Stator Flux linkage DC offset Based Diagnostics of Stator Fault in Permanent Magnet Synchronous Machines

AKANKSHA UPADHYAY
FACULTY OF ENGINEERING | LUND UNIVERSITY

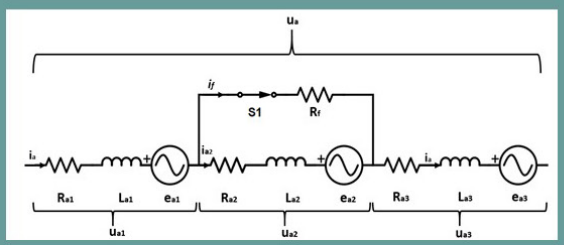

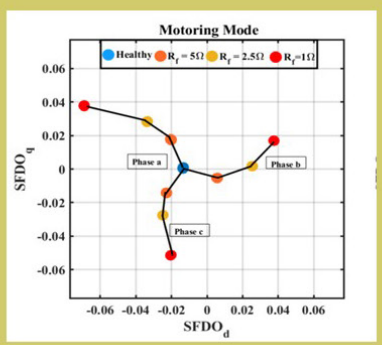

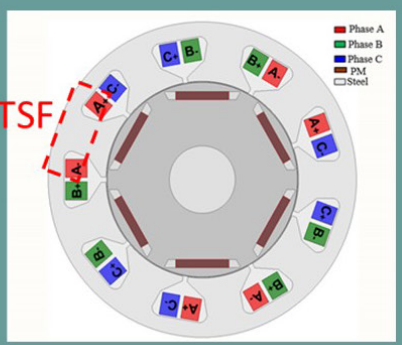

Printed by Media-Tryck, Lund 2024 NORDIC SWAN ECOLABEL 3041 0903

Faculty of Engineering
Division of Industrial Electrical Engineering and Automation
Department of Biomedical Engineering

ISBN 978-91-985110-3-1
CODEN:LUTDEX/(TEIE1098)/1156/2024

Stator Flux Linkage DC Offset Based Diagnostics Of Stator Fault in Permanent Magnet Synchronous Machines

Akanksha Upadhyay

LUND
UNIVERSITY

Thesis for the degree of Licentiate of Engineering
Thesis supervised by :- Prof. Mats Alaküla & Dr. Avo Reinap
Division of Industrial Electrical Engineering and Automation,

2024

Licentiate Thesis Defence

To be presented, with the permission of the Faculty of Industrial Electrical Engineering and Automation of Lund University Sweden, for public criticism at LTH, M building on Thursday, the 14th of November 2024 at 10:00.

Faculty Opponent

Prof. Toomas Vaimann, Tallinn, Estonia
(Research Professor at TalTech – Tallinn University of Technology)

Cover illustration front : Illustrated by Akanksha Upadhyay

The thesis work was financially supported by Swedish Energy agency.

Faculty of Engineering,
Division of Industrial Electrical Engineering and Automation
Department of Biomedical Engineering, Lund University, Sweden

ISBN: 978-91-985110-2-4(pdf)

ISBN: 978-91-985110-3-1 (print)

CODEN:LUTDEX/(TEIE-1098)/1-156/2024

Printed in Sweden by Media-Tryck, Lund University, Lund 2024

"In the end, only three things matter: how much you loved, how gently you lived, and how gracefully you let go of things not meant for you."

By: Gautama Buddha

Acknowledgements

First and foremost, I would like to express my sincere gratitude to my advisor Prof. Mats Alakula who is always ready to help both in research and life. I met him as a researcher from Tokyo who is struggling to keep her family together at one place. He believed in me and brought me here across the seven seas. His supervision, passion, patience, enthusiasm, optimism, (list is long) encourages me to move and cross any obstacles coming through.

Besides, my advisor, I would also like to thank my co-supervisor Avo Reinap, who helped me in an organised way from the very first day and till now. Though, it was difficult for me to understand his vision and wisdom completely but when I tried to imagine and think repeatedly I able to grab. The things that directed me forward are availability, puzzling, help to resolve my unorganised thoughts and doubts. Almost every single comment and suggestions of him, are worth tried during my research. His depth of knowledge in machines helped me learn different perspectives of electromagnetic behaviour of electric machines.

Furthermore, I would like to extend my gratitude to project manager at Volvo namely Zhe Huang and Rasmus Andersson for putting up the roots and significance of research to Swedish Energy Agency and helped me in pursuing my findings came out from the initial literature studies. I am deeply grateful for both of them along with Jonas Ottoson for questioning and bringing out the best out of every DILEMMA meetings.

I am blessed and thankful to be around with my fellow co-workers that have meant a lot to me. Philip Abrahamsson is the one who being there to tell me in and outs of my first teaching at IEA. Fran for doing extensive reading to my first review paper and further always being there to discuss anything that I am going through. You are amazing!

Max and Samuel, thank you for sharing you are knowledge, experience and time with me. Meng and David thanks for being talkative, cheerful and at the same time

meaningful to me. There are so many more colleagues that have given me special fika time. Thanks to Ulf, Olof, Henriette, Ramesh, Gabriel, Sabastian,Per, Leonardo, Alice, Mattias, Hannes, Edwin, Huan Li, Amir and others for facilitating an open discussion on our daily challenges as well as research. Carina, Ulrika, Maira, thank you for all your administrative assistance over the years.

Many thanks to Getachew, Johan and Avo for setting up my first experiment with 1:1 transformer and later during machine test procedures. I wish to acknowledge the help provided by Anton in understanding filters and there appropriate selection during a lab-view setup in laboratory.

Most of all, to the almighty God for giving his endless blessings and strength to make this work possible, to my parents for giving me an inspirational life and taught me to think bigger, family in law for always been supportive , to my loving husband for his unconditional love and faith, my friends in Helsingborg and Stockholm for all their birthday's and holiday's parties and making Sweden a home away from home, and last but not least to my kids for being patient and let her mom to be not just a mom.

Helsingborg, 19 December 2023

Akanksha Upadhyay

Abstract

Condition monitoring and fault diagnosis are imperative for maintaining the safe, reliable, and long-term performance of the traction machine used in electric vehicle. The occurrence of inter-turn faults in stator insulations which can lead to short circuit fault, can significantly degrade the performance and reliability of these machines. Early detection of fault conditions is important to minimize the damage and therefore reduce the downtime of the traction machine. The main focus of this thesis is to understand the root cause behind the stator insulation degradation which leads to inter turn fault and develop a method for the early detection of inter turn faults in the traction machine, particularly permanent magnet synchronous motors (PMSM).

To accomplish this objective, this thesis initially conducted a literature review to uncover the roots of the insulation failure and to identify the existing onboard condition monitoring (OCM) techniques. According to the literature, majority of the condition monitoring techniques are based on current and temperature. However, the permanent magnet synchronous machine (PMSM) of a vehicle drive system is driven under vector control including a current loop, so its not possible to monitor a inter turn fault (ITF) via fundamental frequency currents, and their sequence components. On the other hand, there is a possibility to see a change in characteristic of a PMSM through the stator voltages and the integrals of these, the Stator Flux Linkage (SFL). Therefore, this thesis proposes a relatively simple technique based on stator flux vector component analysis for detecting stator inter turn fault in a PMSM. The proposed diagnostic methodology is able to indicate and allocate the ITF to a specific phase windings.

The proposed diagnostic model is simulated by a complete drive system model and experimentally tested to study PMSM fault behavior under different operating conditions. The validity of the proposed approach is verified by means of both simulation model and experimental results. Experimental results have also demonstrated that the proposed method can identify and locate inter-turn faults even when the stator windings are connected in a delta pattern.

In conclusion, this research presents a new method for inter-turn fault detection of

permanent magnet synchronous motors using stator flux linkage DC offset without having any additional hardware onboard.

Keywords: EV, stator insulation system, PMSM, electric drive, condition monitoring, ITF, SFDO, diagnostics, sensor-less, stator flux linkgaes , traction machine, automotive.

Nomenclatures

Acronyms

Acronyms	What It Stand For	Page Number
EV	Electric Vehicle	1
ESS	Energy Storage System	1
DC	Direct Current	2
VSI	Voltage Source Inverter	2
FD	Fault Diagnosis	2
CM	Condition Monitoring	2
PMSMs	Permanent Magnet Synchronous Machines	2
SoH	State of Health	2
PE	Power Electronic	3
EMI	Electromagnetic Interference	3
AC	Alternating Current	3
ITF	Inter Turn Fault	4
TTFs	Turn to Turn Failures	4
ITSC	Inter Turn Short Circuit	4
TEAM	Thermal, Electrical, Ambient and Mechanical	5
FEM	Finite Element Method	9
VPI	Vacuum Pressure Impregnation	10
PD	Partial Discharge	10
PEEK	Poly Ether Ether Ketone	10
P-core	Pot Core	11
2D	Two Dimensional	11
3D	Three Dimensional	11
IGBTs	Insulated Gate Bipolar Transistors	14
MOSFETs-SiC	Metal-Oxide-Semiconductor Field-Effect Transistor Silicon Carbide	14
LCR	Inductance (L), Capacitance (C), and Resistance (R)	15
RL	Resistance (R)-Inductance (L)	15
RC	Resistance (R)-Capacitance (C)	15
HF	High Frequency	16

Continued on the next page

Continuation from the previous page

Acronyms	What It Stand For	Page Number
IM	Induction Machines	19
OCM	Onboard Condition Monitoring	19
HiPot	High Potential Test	20
PDIV	Partial Discharge Inception Voltage	22
MCM	Machine Characterization Methods	23
DTM	Dynamic Testing Methods	23
SSM	Stand Still Methods	24
PT100	Platinum 100	15
RTD	Resistance Temperature Detectors	24
BEMF	Back EMF	24
ESA	Electromagnetic Signature Analysis	25
MCSA	Motor Current Signature Analysis	25
FFT	Fast Fourier Transform	25
ANN	Artificial Neural Network	26
STFT	Short Time Fourier Transform	26
WT	Wavelet Transform	26
WVD	WignerVille Distribution	26
DWT	Discrete Wavelet Transform	26
PSA	Power Signature Analysis	26
FI	Fault Identification	28
FS	Fault Severity	28
SL	Sensor-Less	28
PI	Performance Indices	28
SFL	Stator Flux Linkage	32
FOC	Field Oriented Control	39
ASRF	Anti-Synchronous Reference Frame	40
SFDO	Stator Flux Linkage DC Offset	41
LPF	Low Pass Filter	49
CW	Concentrated Windings	56
ODE	Ordinary Differential Equations	61
TRF	Torque Ripple Factor	65
AE	Analytical Equation	66
PI	Proportional Integral	69
FW	Field Weakening	72
SM-PD	Simulink-Position Dependent	78
SM-CP	Simulink-Constant Parameters	78
HPF	High Pass Filter	114
SRF	Synchronous Reference Frame	120
C-RIO	Compact Re-configurable IO	128
NI	National Instrument	128
LV	LabView	128
PC	Personal Computer	128
CSV	Comma-Separated Value	129
VI	Virtual Interface	143

End of the table

Latin Symbols

Symbol	Unit	Definition	Page Number
E_m	kV/mm	Dielectric strength	12
k	W/mK	Thermal conductivity	12
c_p	J/kgK	Specific heat capacity	12
E	kV/mm	Electric field intensity	14
d	m	Distance	14
V	V	Voltage	14
Z	Ω	Impedance	16
ϕ	deg	Phase	16
f	Hz	Frequency	16
R_s	Ω	Stator resistance	40
d-q	-	Rotating Reference frame	40
u_a, u_b, u_c	V	Instantaneous value of three phase voltage	42
$\hat{u_a}$, $\hat{u_b}$, $\hat{u_c}$	V	Peak value of three phase voltage	42
$u_j(t)$	V	Three phase voltage	42
R_j	Ω	Three phase resistance	42
$i_j(t)$	A	Three phase current	42
x_a, x_b and x_c	-	Space vector formulation for three phase	44
$\overrightarrow{x}$	-	Space vector	44
t	s	Time	45
$SFDO_d$,$SFDO_q$	Wb	Stator flux linkage DC offset in ASRF	50
L_{ab}, L_{ac}, L_{bc}	H	Mutual-inductances between phase a to b, a to c and b to c	54
L_{aa}, L_{bb}, L_{cc}	H	Self-inductances of phase a,b and c	54
i_a ,i_b,i_c	A	Three phase current	55
e_a ,e_b,e_c	V	Three phase induced volatge	55
R_a,R_b,R_c	Ω	Phase resistance across phase a,b and c	55
M	H	Mutual-inductances	55
L	H	Self-inductances	55
P	W	Mechanical power	56
T_e	Nm	Electromagnetic torque	56
R_{a2}	Ω	Faulted coil resistance	57
R_{a1}	Ω	Healthy coil resistance	57
L_{a2}	H	Faulted coil inductance	57
e_{a2}	V	Induced voltage across faulted coil	57
N_2	-	Number of short circuited turns	57
N_a	-	Total number of turns in the faulted phase	57
N_s	-	Total number of turns in the phase	57
L_{a1}	H	Self inductances of the healthy part of the phase a	57
L_{a2}	H	Self inductances of the faulted part of the phase a	57
M_{a1a2}	H	Mutual inductances between coil a1 to coil a2	57
M_{a2a3}	H	Mutual inductances between coil a2 to coil a3	57
M_{a2b}	H	Mutual inductances between coil a2 to phase b	57
M_{a2c}	H	Mutual inductances between coil a2 to phase c	57

Continued on the next page

Continuation from the previous page

Symbol	Unit	Definition	Page Number
i_f	A	Fault current	61
i_{a2}	A	Current in coil a2	61
e_f	V	Induced volatge across the faulted coil	61
B_m	Nm/rpm	Viscous friction factor	62
T_L	Nm	Load torque	62
J	kg.m2	Moment of inertia	62
L_d ,L_q	H	Inductances at d and q axes	70
i_d ,i_q	A	Current at d and q axes	70
u_d ,u_q	V	Inverter voltage at d and q axes	70
U_{dc}	V	DC link voltage	70
T_s	s	Sampling time	70
L_{dc}	H	Average self inductance of the stator winding	90
L_{ac}	H	Varying self inductance of the stator winding	90
L_s	H	Stator inductance matrix	100
f_c	Hz	Cut-off frequency	116

End of the table

Greek Symbols

Symbol	Unit	Definition	Page Number
ρ	kg/m3	Mass density,	12
σ	S/m	Electric conductivity	12
ϵ	-	Dielectric constant	12
$tan\delta$	-	Dissipation factor	12
$\alpha\beta$	-	Stationary reference frame	40
τ	-	Time constant	40
θ_r	deg	Angle between stationary reference frame and rotatory reference frame	40
$\overrightarrow{u_s}^{\alpha\beta}$	V	Inverter voltage vector	41
$\overrightarrow{i_s}^{\alpha\beta}$	A	Terminal current vector in stationary reference frame vector	41
$\overrightarrow{\psi_s}^{\alpha\beta}$	Wb	Stator flux linkages vector	41
ω	rad/s	Supply voltage frequency	42
γ	deg	Phase shift = $\frac{2\pi}{3}$	42
ψ_j	Wb	Stator flux linkage of three phase	12
ψ_a, ψ_b, ψ_c	Wb	Instantaneous SFL in phase a,b and c	42
$\hat{\psi_a}$, $\hat{\psi_b}$, $\hat{\psi_c}$	Wb	Peak value of SFL in phase a,b and c	42
δ_a, δ_b, δ_c	deg	Phase difference due to applied load in each phase	42
ψ_α,ψ_β	Wb	Stator flux linkages in stationary reference frame	43
δ_a, δ_b, δ_c	deg	Phase difference due to applied load in each phase	42
ψ_d,ψ_q	Wb	Stator flux linkages in synchronous reference frame	43

Continued on the next page

Continuation from the previous page

Symbol	Unit	Definition	Page Number
ψ_{d-},ψ_{q-}	Wb	Stator flux linkages in anti synchronous reference frame	43
$\overrightarrow{\psi_s}^{d-q-}$	Wb	Stator flux linkages vector in anti synchronous reference frame	43
$\overrightarrow{\psi_s}$	deg	Stator flux linkages vector	45
ψ_{pm}	Wb	SFL in phases *(a, b and c)* from the permanent magnets of the rotor	54
ω_e	rad/s	Time derivative of the electrical position of the rotor	55
μ	-	Fault fraction	57
Ψ_m	Wb	SFL from permanent magnet	61
ω_m	rad/s	Mechanical rotor speed	62
ψ_f	Wb	Flux linkages across the faulty coil	45
$\phi_{j,n}$	Wb	The phase shift of nth harmonic in phase a,b and c	66
Ψ_{aa}	Wb	The total flux linkage to *phase a*,	89
Ψ_{ab}	Wb	The flux from *phase a*, linking the coils of *phase b*	89
Ψ_s	Wb	Stator flux linkage	100
$\Psi_{\alpha\beta}$	Wb	Stator flux linkage in stationary reference frame	100
u_α, u_β	V	Inverter voltage in stationary reference frame	114
i_α,i_β	A	Machine terminal current in stationary reference frame	114
ω_c	rad/s	Filter cut off angular frequency	114
ω_s	rad/s	Stator electrical angular frequency	114

End of the table

Contents

Acknowledgements I

Abstract III

Nomenclatures V

1 Introduction 1
- 1.1 Background . . . 1
- 1.2 Problem statement . . . 4
- 1.3 Thesis objectives and outline . . . 4
- 1.4 Scientific contributions . . . 5
- 1.5 Publications . . . 6

References . . . 7

2 Stator insulation system and test specimen for studying TEAM stresses 9
- 2.1 Stator insulation systems . . . 9
  - 2.1.1 Type I and Type II insulating systems . . . 10
- 2.2 Test specimen . . . 11
  - 2.2.1 Geometry and material selection . . . 12
  - 2.2.2 Simulation results and TEAM stresses . . . 13
- 2.3 Summary . . . 17
- 2.4 Learning outcomes . . . 17

References . . . 18

3 Condition monitoring techniques of ITF -A review 19
- 3.1 Background . . . 19
- 3.2 The condition monitoring technique . . . 20
- 3.3 Onboard condition monitoring techniques and its classification . . . 20
- 3.4 OCM techniques under self analysis mode . . . 21
  - 3.4.1 Partial discharge monitoring . . . 22
  - 3.4.2 HF impedance/inter-turn capacitance monitoring . . . 22
  - 3.4.3 Machine characterization methods . . . 23
- 3.5 OCM techniques under traction Mode . . . 24
  - 3.5.1 Temperature monitoring . . . 24

3.5.2 Vibration monitoring . . . 25
3.5.3 Electromagnetic signature analysis . . . 25
3.5.4 Motor current signature analysis . . . 26
3.5.5 Power signature analysis . . . 27
3.5.6 Monitoring of sequence components . . . 27
3.5.7 Quality assessment and proposal of new diagnostic method 29
3.6 Futuristic trends in monitoring . . . 31
3.7 Summary . . . 32
3.8 Learning outcomes . . . 32
References . . . 33

4 The proposed diagnostic technique 39
4.1 Vector control of PMSM . . . 39
4.2 Proposed diagnostic technique . . . 40
4.3 Mathematical Intrpretations . . . 42
4.3.1 Case study . . . 48
4.4 Vector control with proposed diagnostic scheme . . . 50
4.5 Summary . . . 51
4.6 Learning outcomes . . . 51
References . . . 52

5 Inter turn fault analysis using analytical model 53
5.1 Analytical model of PMSM-without ITF . . . 53
5.2 Analytical model of PMSM with ITF . . . 56
5.2.1 Voltage equation of faulted PMSM . . . 58
5.2.2 Specifications of the test machines used for modeling . . . 61
5.3 Simulation results . . . 62
5.4 Model initialisation . . . 65
5.5 Simulink model with current controller- without ITF . . . 69
5.5.1 Simulink model . . . 69
5.5.2 Simulation setup and results . . . 71
5.6 Simulation results with current controller - with ITF . . . 73
5.6.1 Simulink model with position dependent (SM-PD) values from FEM . . . 78
5.7 Summary . . . 81
5.8 Learning outcomes . . . 81
References . . . 82

6 Parameter identification using FEM model 83
6.1 Introduction . . . 83
6.2 FEM model of healthy PMSM . . . 84
6.2.1 RMxprt . . . 85

6.2.2 Stator design details . . . 85
6.2.3 Rotor design details . . . 86
6.2.4 Machine Specification . . . 87
6.2.5 No load study . . . 88
6.2.6 Inductance of a healthy machine . . . 89
6.2.7 Back emf of healthy machine . . . 91
6.3 FEM model of unhealthy machine . . . 92
6.3.1 Fault creation using Co-Simulation(Maxwell/Twin Builder) . . . 93
6.3.2 Model setup . . . 93
6.3.3 Simulation approach and operating modes . . . 94
6.4 Parameters Identification . . . 95
6.5 Summary . . . 110
6.6 Learning outcomes . . . 110
References . . . 111

7 Inter turn fault diagnostics using SFDO 113
7.1 ITF diagnostics- using simulink model . . . 113
7.1.1 The SFDO observer . . . 113
7.2 Simulation setup and results . . . 117
7.2.1 Operating modes . . . 118
7.2.2 Idling Mode . . . 118
7.2.3 Motoring Mode . . . 121
7.2.4 Field weakening Mode . . . 122
7.3 Summary . . . 124
7.4 Learning outcomes . . . 124
References . . . 124

8 Experimental verification 127
8.1 Experimental setup . . . 127
8.1.1 Rotor angle offset calibration . . . 130
8.2 Experimental results . . . 131
8.2.1 Model Validation . . . 137
8.3 Summary . . . 142
8.4 Learning outcomes . . . 143
References . . . 144

9 Conclusions 145
9.1 Conclusion . . . 145
9.2 Future Work . . . 147

A Appendix A - RMxprt Model Data 149
A.1 Phase measurement obtained from the FEM results . . . 154
A.2 Steps of coupling Maxwell to Twin Builder . . . 155

Chapter 1

Introduction

1.1 Background

Over the past several years the number of EVs has shown a strong increase rate. With a goal of achieving zero carbon emissions by 2045[1, 1], this rate of increase is not expected to slow down. It is no longer just carbon emissions that are driving the EVs (EV's) popularity but also high starting torque, improved efficiency, better acceleration, less noise, and low maintenance requirements. With the transportation electrification industrial revolution worldwide in general and in Sweden, a lot of academic and industrial research and development efforts have been directed towards enhancing the design, control, and reliability of the EV powertrains[2, 1].

The EV powertrain is made out of energy storage system (ESS) and electric drive unit as shown below:

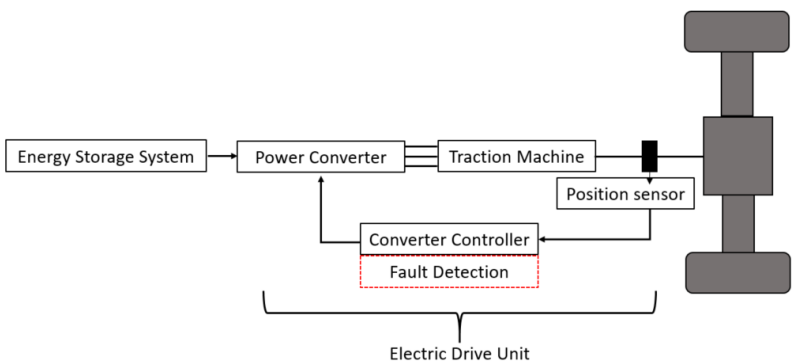

Figure 1.1: Schematic diagram of EV powertrain with diagnostic option.

ESS responsible to supply the demand power to the EV propulsion system together with DC-DC bidirectional converter to regulate the DC (Direct Current)voltage to the DC link input to the power converter. Electric Drive unit consists of power converter and Voltage source inverter (VSI) ; a digital controller with a real-time vector control implementation and Traction machine[2, 1]. The traction machine is the only moving electrical apparatus in a typical electric drive system. The ESS, DC-DC converter, DC link, and VSI are static by nature. It is therefore not surprising that it develops internal faults more often than any other component in the EV drive system. Thereby, reliable, fast, accurate, and online fault diagnosis (FD) and condition monitoring (CM) techniques are required to enhance the EV's propulsion system's reliability.

When studying the EV drive system of the powertrain, the system's practicality should be considered. For example, Tesla uses induction motors in their earlier EV models[3, 1]but now from model 3 switching to interior permanent magnet motor[4, 1], whereas Volkswagen[5, 1], Volvo [6, 1], and Nissan [7, 1] also uses interior permanent magnet motors. Moreover, the EV produced by Land Rover use switched reluctance motor (SRM) [8, 1]. For more than a decades and still now, permanent magnet synchronous motors (PMSMs) have been the workhorse of the EV industry. Due to its mature technology, high power density, high efficiency, and ease of control of external mechanical torque [9, 1]. In light of this, this work considered PMSMs as a traction machine in EVs drive systems.

Fault diagnosis and condition monitoring studies in traction machines are as old as the motors' studies [2, 1]. Nevertheless, when FD and CM problems are addressed in the EV powertrain, the drive system's nature should be taken into account. For instance, in EV drive systems, the PMSMs are vector controlled [2, 1]. Therefore, the controller reaction to the fault should be deeply considered. Furthermore, monitoring the condition of the drive system does not only mean detecting faults. It also includes evaluating the status of the system.

Condition monitoring (CM) and detecting faults (FD) are the first steps toward enhancing its reliability [10, 1]. A condition monitoring system (CM) monitors a physical system so that the changes in its characteristics may be used to schedule maintenance before the system suffers severe deterioration or breakdown [10, 1]. In order to estimate a system's health condition, CM utilizes knowledge of the failure mechanisms of physical parts.

Commonly used terms like prognosis and diagnosis together with condition monitoring are defined here as:

1) **Fault Diagnosis (FD)**: is to find out the root cause behind the fault [10, 1].

2) **Prognosis**: assesses the current state of health (SoH) level of a component and predicts the component's health at some point in the near future [10, 1].

3) **Condition Monitoring**: is to measure the real time condition of a component, in case, if it drifts away from the healthy condition, appropriate action can be taken [10, 1].

Condition monitoring and fault diagnostics are the terms used and elaborated more in chapter 2 and 3 .

Types of fault in PMSM drive systems - In the PMSM drive system, three significant categories of faults could happen to the system while it is in service and provided through a figure below. PMSM faults are classified by the location as stator and rotor faults.

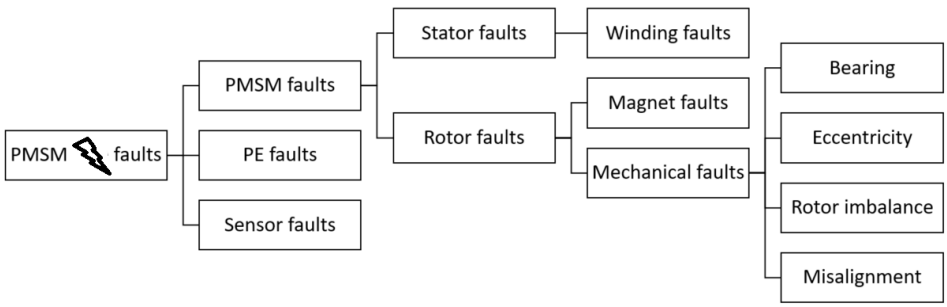

Figure 1.2: Types of faults in PMSMs drive unit

Power electronic (PE) faults are caused due to control circuit failure, auxiliary components failure (sensors), converter circuit failure and that could be divided further to: Capacitor failure (DC-link);power transistor failure; diode failure and inductors and EMI (Electromagnetic Interference) filter failures. These are omitted from the figure because there occurrence is very less around 9% [11, 1].

Based on a literature survey[2, 1], stator winding failures are one of the most common reasons for AC motor failures and represent between 36% and 66% of all failures, while bearing faults represent between 13% and 41%, respectively, depending on the type and size of the machine, as shown in Figure 1.3.

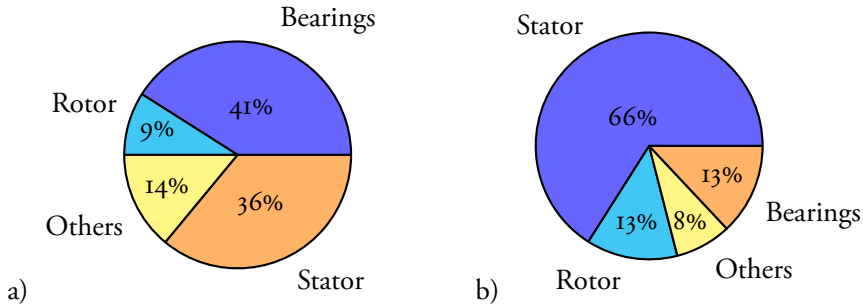

Figure 1.3: Faults percentages by various components in a) low voltage and b) high voltage machines[2, 1]

The most common electrical faults of PMSMs are stator winding faults. Approximately, 21% [11, 1] of all the faults in PMSM accounts for the inter-turn fault (ITF). Basically, stator-related faults start with the turn-to-turn faults in one of the stator's coils. It is noteworthy to mention that throughout the dissertation chapters, the inter-turn failures (ITFs) are the same as inter turn short circuit (ITSC) and turn to turn failures (TTFs).

1.2 Problem statement

Condition monitoring and fault diagnostics of stator faults of traction machine -

The influence of ITF on the PMSM is generally small at the embryonic stage, but it causes a circulating current in the shorted turns. Unlike rotor's electrical or mechanical faults, the ITF once remains undetected then it propagates to the other turns and eventually leads to phase faults, phase to phase faults and phase-to-ground faults. The ITF will also induce extra flux at the fault location, and the extra flux may lead to an irreversible demagnetisation fault [10, 1].Thus, protection by fault detection against this situation is essential to be investigated.

1.3 Thesis objectives and outline

This licentiate dissertation's main objectives is to develop and implement non-invasive, online, precise, and non-destructive fault diagnosis and condition monitoring routines to detect the ITFs in vector controlled driven traction machines of EV drivetrain. Furthermore, the developed technique should be able to allocate the faulty phase and fault severity. To achieve the first objective of FD and CM routines development, the following procedures were done in the following nine chapters:

- A physics based simulation of pot core transformer is made to understand the root causes behind the insulation failure under thermal, electrical, ambient and mechanical stresses (TEAM) in chapter 2. In addition, an overview of stator insulation systems along with the available standards for EV traction machines is presented.
- A detailed investigation of the available CM techniques for EV traction machine is presented together with the existing challenges of existing monitoring method, as well as futuristic trends and proposed methods for identifying ITFs is presented in chapter 3 .
- Based on the investigation in the previous step, detection of ITF using the stator flux linkage vector component analysis based FD techniques are introduced and explained in chapter 4.
- Analytical modeling and analyzing the effect of the ITF with and without the vector controller action combined with the power electronics inverter switching. An analysis of the behavior of the stator magnetic flux, the change in inductance, the fault current, and electromagnetic torque under varying fault severity is presented in chapter 5.
- Physics based modelling using FEM and simulation of traction machine to assess the fault parameters and flux distribution around the faulted turns/coils is analysed and provided in detail in chapter 6.
- Dynamic model development using the fault parameters obtained from the FEM model, for ITF diagnostics using stator flux linkage vector component under different operating conditions is discussed in chapter 7.
- Experimental investigation and implementation of the proposed FD scheme in the real electric drive system is provided in chapter 8.
- The main conclusions and how to take this research ahead is provided in chapter 9.

1.4 Scientific contributions

In the field of fault diagnosis and condition monitoring of the ITFs in traction machine's drive system designed for the EV powertrain, the following contributions were achieved and published:

- A comprehensive in-depth review of online and offline condition monitoring of stator inter-turn fault. Based on a literature review, a new classification of onboard condition monitoring techniques is proposed, which includes self-analysis and traction modes.
- Proposal of novel real time stator flux linkage based diagnosis technique on a controller that utilises power converter input voltages and signal processing to see the stator flux intrusively.
- System level analysis of analytical fault model of PMSM together with stator flux DC observer in simulink simulation software.
- Development of a FEM-based model to analyze flux line distribution under fault conditions and its effect on mutual coupling and induced voltage.
- Experimental implementation and verification of the proposed diagnostic technique under different fault severity, fault location and operating modes.

1.5 Publications

1. A. Reinap and A. Upadhyay, "Specification of a Specimen for Accelerated Thermal Aging Tests," 2019 IEEE 12th International Symposium on Diagnostics for Electrical Machines, Power Electronics and Drives (SDEMPED), 2019, pp. 49 55,doi:10.1109/DEMPED.2019.8864856.
2. A. Upadhyay, M. Alaküla and F. J. Márquez Fernández, "Characterization of Onboard Condition Monitoring Techniques for Stator Insulation Systems in EVs A Review," IECON 2019 45th Annual Conference of the IEEE Industrial Electronics Society, 2019, pp. 3179 3186.
3. A. Upadhyay, and M. Alaküla , "A Theoretical Study Of Stator Flux Linkage DC Offset Based Stator Fault Detection For PMSM Drive Systems," IEEE Vehicle Power and Propulsion Conference (VPPC) 2022.
4. A. Upadhyay, and M. Alaküla , " Stator Flux Linkage DC Offset Based Stator Fault Detection For PMSM Drive Systems,"IECON 2022 48th Annual Conference of the IEEE Industrial Electronics Society, 2022.
5. A. Upadhyay, A. Reinap and M. Alaküla "Parameter Identification For inter turn fault Detection In Permanent Magnet Synchronous Motors Using Stator Flux Linkage DC Offset Monitoring," 2023 IEEE 15th International Symposium on Diagnostics for Electrical Machines, Power Electronics and Drives (SDEMPED), 2023.

References

[1] https://www.government.se/contentassets/e731726022cd4e0b8ffa0f8229893115/swedens-draft-integrated-national-energy-and-climate-plan/.

[2] T. Orlowska-Kowalska, M. Wolkiewicz, P. Pietrzak, M. Skowron, P. Ewert, G. Tarchala, M. Krzysztofiak, and C. T. Kowalski, "Fault diagnosis and fault-tolerant control of pmsm drives–state of the art and future challenges," *IEEE Access*, vol. 10, pp. 59 979–60 024, 2022.

[3] [Online]. Available: https://www.tesla.com/en_eu/blog

[4] [Online]. Available: https://www.tesla.com/en_eu/model3

[5] [Online]. Available: https://www.volkswagen.se/sv/modeller/tiguan

[6] https://www.volvocars.com/se/support/car/xc60.

[7] https://www.nissanusa.com/electriccars/leaf/versions-specs/.

[8] I. Boldea, L. N. Tutelea, L. Parsa, and D. Dorrell, "Automotive electric propulsion systems with reduced or no permanent magnets: An overview," *IEEE Transactions on Industrial Electronics*, vol. 61, no. 10, pp. 5696–5711, 2014.

[9] Z. Zhu and C. Chan, "traction machine topologies and technologies for electric, hybrid, and fuel cell vehicles," *IEEE Vehicle Power and Propulsion Conference*, 2008.

[10] G. C. S. E. A. B. I. Culbert and H. Dhirani, "Electrical insulation for rotating machines-design, evaluation, aging, testing, and repair," *the Institute of Electrical and Electronics Engineer Inc.*, 2004.

[11] T. C. A. Gandhi and L. Parsa, "Recent advances in modeling and online detection of stator interturn faults in electrical motors," *IEEE Transactions on Industrial Electronics*, vol. 58, no. 5, p. 1564–1575, 2011.

Chapter 2

Stator insulation system and test specimen for studying TEAM stresses

This chapter briefly describe the stator insulation system and explores various reasons derived from literature to determine the root cause behind the stator insulation failure. To gain a deeper understanding of fault initiation, a solenoid-based sample test specimen has been analyzed using finite element method (FEM) to see the effect of stresses like thermal, mechanical and electrical.

2.1 Stator insulation systems

The stator of a traction machine consists of three basic components: the stator core, the electric conductors (usually copper), and the insulation. A low reluctance path for the magnetic field is provided by the core. It is usually made up from thin sheets of electric steel. The electric conductors carry the currents supplied to the machine and should be dimensioned to withstand operation without overheating. Three-phase traction machines typically have multiple parallel strands wound on the core of each phase coil in order to reduce AC losses. The stator insulation plays a passive role, which means it does not contribute to the creation of magnetic fields nor to their guidance, but it is necessary to keep the conductors intact, electrically separate from each other and isolated from the chassis, the machine's casing, and improve slot fill [1, 2].

The stator insulation system is divided into primary and secondary insulation [2, 2]. The stator primary insulation is divided into three main categories: the strand insulation for each conductor (implemented by using insulated magnet wire), the coil separator in case of multi-layer windings and the slot insulation or slot liner [3, 2].

A secondary insulation is used to enhance the electrical insulating strength of the winding, protecting from environmental conditions like dirt and moisture, and providing additional mechanical strength. A common way of implementing the secondary insulation is by impregnating the stator with epoxy, silicone or urethane polymers. Impregnation helps in removing trapped air between the winding conductors and in between the winding and the core, which degrades heat dissipation. Impregnation techniques for the stator winding vary with the application needs. It can be provided by dipping, trickling and vacuum pressure impregnation (VPI) [4, 2].VPI is considered to be complex and time consuming as compared to other impregnation techniques.

2.1.1 Type I and Type II insulating systems

The safety and reliability of motor performance is guaranteed by the proper design and use of suitable materials. Selection of insulating materials depends on the voltage rating, thermal rating, mechanical strength required by the traction machines. Traction machines are supplied by inverter drives, therefore the insulating material for traction machines are often subjected to over-voltages having high frequency content. Under such conditions, degradation due to erosion or partial discharge (PD) activity takes place which leads to the breakdown of insulation[5, 2]. In order to prevent such PD activity, solution adopted for insulating system are mainly depend on their rated voltage. When the required voltage rating of traction machines are lower than 1000 V, Type I insulation systems are used. In Type I insulation system, the primary insulation are organic material and impregnations are used in secondary insulation.

Type II insulations systems are used in traction machines of voltage rating above 1000 V. In this case rectangular wires are used. Strand, turn and groundwall insulations are employed in an orderly manner. Furthermore, mica based tapes are used to provide corona resistance during PD activity. In order to tackle the problems of PD activity, new insulation materials called PD resistant materials or PD free materials are introduced. Considering a insulation point of view, a PD free concept can be realized by uniform or homogeneous coating of primary insulation with certain thickness. At this moment, poly ether ether ketone (PEEK) is gaining popularity in materials of choice for attaining PD resistance[6, 2].

Stator faults

Stator insulation failure leads to stator faults. Usually it begins with inter-turn faults and subsequently develops further into more severe phase-to-phase and phase-to-ground faults [7, 2]. The other fault modes are coil to coil and phase to phase short-circuits as provided in [8, 2].

The stator of the traction machine is exposed to somewhat different stress conditions as compared to an electrical machine used in more stationary industry applications [9, 2]. During operation inside an EV the stator is subjected to stresses of diverse nature, usually referred to as TEAM stresses - thermal, electrical, ambient and mechanical - which have an impact on the stator insulation condition [10, 2], [1, 2]. Below is a brief description of these stresses and their root causes.

The proposed specimen for thermal accelerated aging test in our lab[11, 2] sheds light on these stresses.

2.2 Test specimen

Analyzing and visualizing the stresses in traction machines is simplified if a reduced but equivalent test object can be proposed. A pot core (P-core) has been proposed as test specimen due to its simplicity and availability. P-cores have many advantages, including high quality factor and temperature stability. Their self-shielding geometry isolates the winding from external magnetic fields as well as forcing the direction of the generated magnetic field. Equivalent in terms of materials and preferably winding parameters.

The test specimen[11, 2], is a parallel wired solenoid that is evaluated by using an axi-symmetric 2D (two Dimensional) finite element (FE) model in Comsol multi-physics. The aim of the design model is visualizing an interior stress distribution of an idealized coil. In Figure 2.1, an axis-symmetric 3D (three Dimensional) model of a multi-turn coil is presented. Parallel wired solenoids are depicted as having 56 turns with number of turns going in and out on two-dimensional representations[11, 2] .

Through the test specimen, we intend to investigate internal stress distributions, physical processes that may cause insulation failures, and fault development.

To understand electrical, thermal or thermal-mechanical stress distributions, Comsol multi-physics performs finite element simulations.

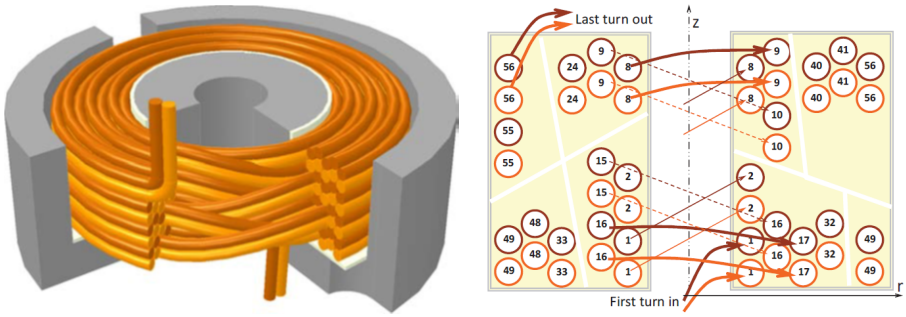

Figure 2.1: Double stranded coil layout and wire transition between turns and layers. 28 turn parallel wire coil shown in 3D and 56 turn parallel wire coil shown in 2D schematics[11, 2]

2.2.1 Geometry and material selection

Two P-core transformer are of interest one is small (Ø30H10) having diameter of 30mm and height of 10mm while another one is large P-core having diameter of 50mm and height of 40mm (Ø50H40). Smaller P-core are only used in FEM based analysis, while big P-core are intended for visualising high frequency impedances.

Table 2.1 shows a complete list of materials and their properties used in building the model in Comsol.

Table 2.1: MATERIAL SPECIFICATIONS AND PROPERTIES [12, 2]

	copper conductor	PEI/PAI enamelling	Impregnation Epoxy	Nomex 418 ground wall	Air void and ambient	Ferrite P-core
Mass density, ρ [kg/me3]	8700	1500	1500	1120	1.23	4700
Electric conductivity, σ [S/m]	$57e6$	5e-20	1e-11	5e-18	5e-15	1e-5
Dielectric strength, E_m [kV/mm]	1	4	3.6	2.5	1	1
Dielectric constant, ϵ [-]		23	20	38	3.3	
Dissipation factor, tanδ [-]		1e-3		6e-3		
Thermal conductivity,k [W/mK]	400	0.26	0.5	0.1	0.026	
Specific heat capacity,c_p [J/kgK]	385	1000	1500		1.0	
Thermal expansion,α [1/K]	17e-6	16e-6	1e-4		3.4e-3	
Elasticity, E [Pa]	$110e9$	$7.4e9$	$3.5e9$		1.4	
Poisson's ratio,v []	0.35	0.42	0.44			
Compressive strength, [Pa]		$2.8e8$				
Tensile strength, [Pa]		$1.5e8$				

2.2.2 Simulation results and TEAM stresses

TEAM stresses are evaluated and described in the following subsection under different stress cases following the setup of the model. There is no abbreviation order since mechanical and thermal stresses are combined together during simulation.

Thermal stress- Insulation design of stator depends largely on the thermal requirement of the machine operation. If the machine operates above the designed threshold temperature the insulation is considered to be in thermal stress. This temperature results from copper, eddy current and stray losses in the conductors. Core loss and windage losses further elevates the winding temperature. The high temperature causes a chemical reaction leading to degradation of organic material coated on conductors. Consequently, brittleness and delamination [1, 2] of ground-wall insulation appear. The chemical oxidation process is given by Arrhenious rate law proposed by Dakin [1, 2].The equation approximates the life of insulation with respect to temperature. Its well known considered as rule of thumb that every 10°C rise in temperature above the threshold temperature leads to decrease in a insulation life by 50%.

Mechanical stress-Thermal stress in the winding initiates relative motion between the molecules of organic materials used as insulation materials, causing insulation layers to expand and contract in limited space, deteriorating their strength and causing them to breakdown. To show the deterioration caused by thermal stress a simulation is made on the test specimen shown in Figure 2.2.

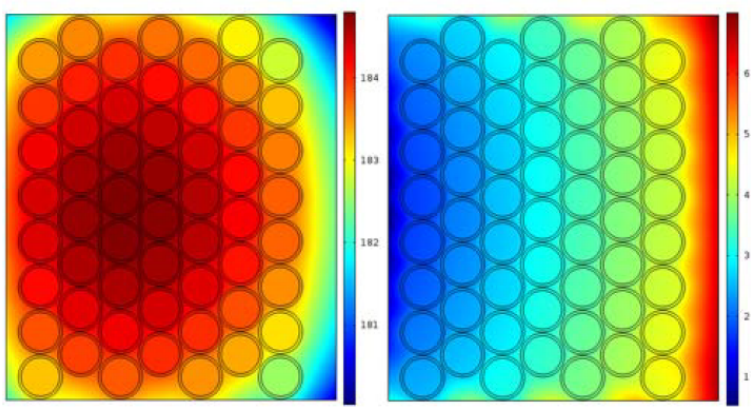

Figure 2.2: Temperature [°C] and displacement 10μm.[11, 2]

The thermal load in the model is defined as following: the specific heat losses in conductors are 1 W/cm^3, which corresponds to current density of 5.88A/mm^2 (2.96A for Ø0.8mm wire) and resistivity of 28.8nΩm at 182°C. All external surfaces are

defined to have natural cooling conditions of 5W/m^{2}K at 20°C.

Figure 2.2, shows the resulting temperature distribution and thermo-mechanical displacement. The leftmost figure shows the maximum temperature at the center, causing strains and displacements in the rightmost figure equal to 10μm. In case of displacement, the unit scale is in multiples of 10μm.

This analysis will yield information on the relationship between tensile and compressive strains on strand and turn insulation, which can result in mechanical wear, fracture, and failure.

Electrical stress- The stator insulation considered to be in electrical stress if the applied voltage is more than the breakdown voltage. Transient voltages are generated by switching IGBTs and MOSFETs-SiC in inverter-fed drives, or by mismatches in the impedance of the inverter, cable, and traction machine. Transient voltage caused by fast switching devices in modern drives could stress electric vehicle insulation systems. Normally, insulation systems are designed to resist transient surges. Faster transients, on the other hand, can cause failures due to non-uniform voltage distributions. Through parasitic capacitances across inter turn capacitances, inter strand capacitances, and inter phase capacitances, steep fronted voltages cause transient leakage currents.

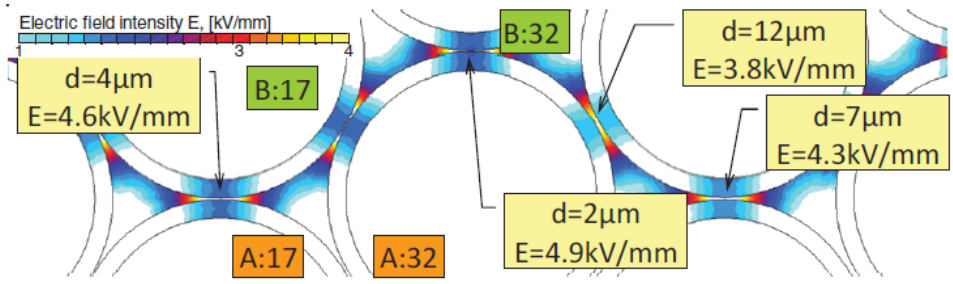

Figure 2.3: Electric field intensity distribution at 200 V with variable air-space between wires[11, 2]

By using electrostatics simulations in comsol, the inception field distribution between parallel strands A and B is visualized when 200 V is applied across them. There are 2-12μm of air space between each strand as shown in Figure 2.3, and the coating thickness is 50μm. The voltage applied across the parallel strands is 200V. Voltage difference can be small but E field can be large as (E=V/d). It can cause conditions for dielectric breakdown since air has a dielectric strength of 3 kV/mm and is part of the winding assembly[1, 2]. The result of the electrical breakdown is an electric discharge and material erosion that wears down the main insulation, enamel coating, etc.

Parameters change under high frequency- Using a large coil, a measurement is made

to examine the parametric change under high frequency.

Impedance characteristics The test specimen is formed with a 0.6 mm parallel wired 200 turn coil in an 8 x 23.8 mm window. Lab setup together with a circuit schematic is shown in Figure 2.4. An Hioki IM3533 − 01 LCR meter is used to measure impedance between 20Hz and 200kHz.

The test specimen's circuit schematic is shown in Figure 2.4. The RL-links represents the parallel wires in the circuit and RC-links is defined as the parasitic between them.

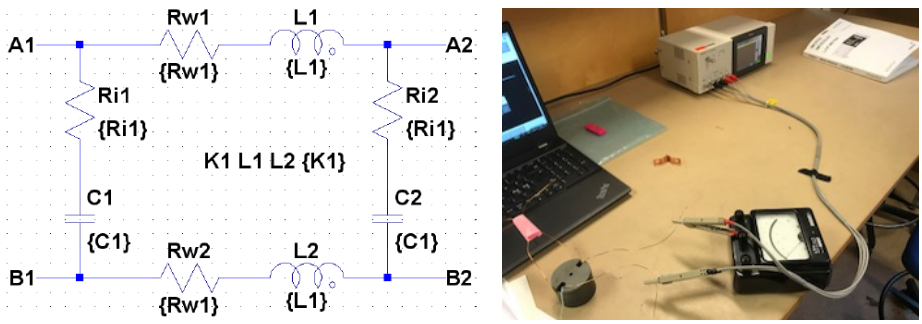

Figure 2.4: Circuit presentation of a test coil and lab setup for measuring coil impedance[11, 2]

A parallel wire test coil is apparently a transformer, where the test voltage can be applied across the inductance (A1A2, B1B2) or turn-to-turn insulation (A1B1). The magnetic fields can be added or subtracted and amplified by using a magnetic core. As a result of introducing the core and main insulation, a new coil-to-core capacitance is added. The selected measurements including the magnetic core are shown in Figure 2.5.

The first figure in left (A1B1) belongs to capacitance between the coils that decrease from 5.98 nF to 5.80 nF over the frequency range. The corresponding series resistance reduces from 5.27 kΩ to 3 Ω. The second figure in right (A1A2+BOC) reveals inductance 18.2 mH, resonance at 142 kHz and series resistance 1.33 Ω.

If the previous measurement had coil B in open circuit then in the next experiment coil B is shorted. The third figure (A1A2+BSC) reveals inductance 14 µH, series resistance 2.66Ω, and at 140 kHz the phase angle is close to 0.

The fourth connection (A2B1) can be defined as differential mode excitation, which reveals series resonance at 15.3 kHz followed by parallel resonance at 142 kHz attached to previously known parameters Ls and Cs.

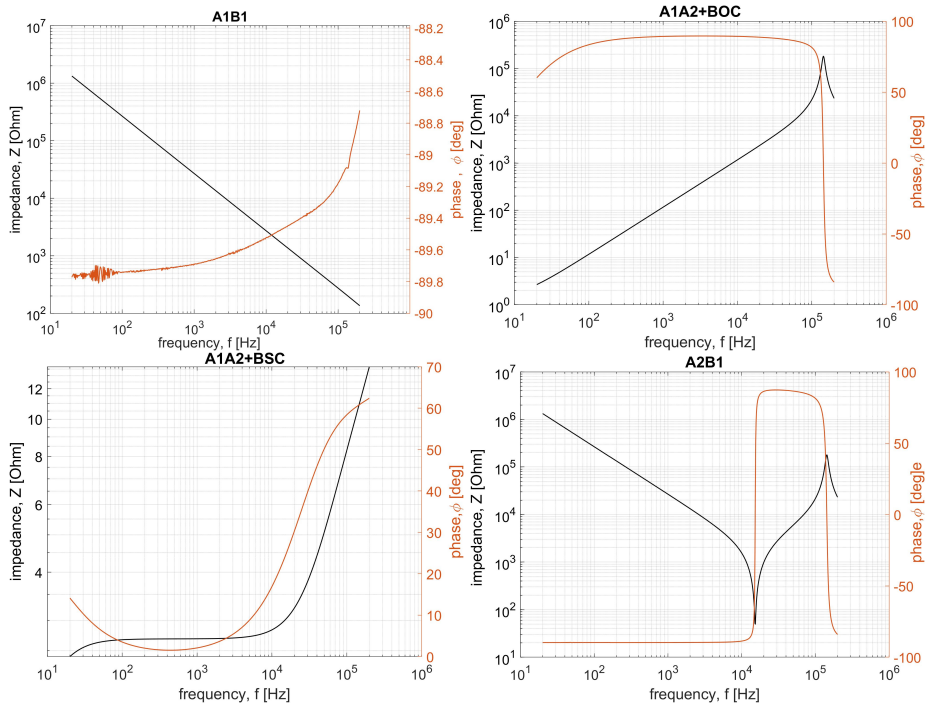

Figure 2.5: Impedance characteristics for four selected circuital connections

HF characteristics of the specimen indicate a decrease in parasitic capacitance between coil turns, an increase in leakage inductance, and a decrease in magnetizing inductance as frequency increases. This short lab exercise helped to understand the measurements to evaluate the parameters for the specimen and to determine how and what parameters change with high frequency.

This measurement was initially intended to make a large number of tests for accelerated ageing studies, but due to other priorities in the project and time constraints, this work has been suspended.

Ambient stress- Insulation system exposed to dust, gases, water, humidity, oils and chemicals which can increase insulation deterioration in traction machine. Thermal, mechanical and electrical ageing will proceed at a faster rate due to moisture absorption or because of surrounding air. Typically, the operating environment of most traction machines results in two or more of these ageing mechanisms being present. Interactions between the stresses may be complex and result in unexpected consequences.

2.3 Summary

Stator insulation system and its deterioration under dynamic TEAM stresses have been the subject of this chapter. A description of the proposed test specimen geometry and material selection is provided. An investigation of TEAM stress analysis was carried out using FEM with the proposed specimen. The results of simulations conducted to understand how insulation material changes under electrical, thermal, and mechanical stresses. Table 2.2 summarises the nature of stresses and root causes behind them. Individually or synergistically, these stresses can cause decomposition and result in failure, fatigue, or reduced insulation life.

Table 2.2: Nature of stresses and Root Causes

Stresses	Root Causes
Thermal	Overload .
Electrical	Switched voltage supply with high voltage and voltage derivatives.
Ambient	Humidity, dirt, exposure to chemicals.
Mechanical	Thermal,Vibrations.

2.4 Learning outcomes

- The understanding of stator insulation system in traction machines is made by following the standards and selecting the specimen's geometry. The insulation material should take into consideration the traction machine's operating frequency, temperature, and mechanical strength in order to ensure it has a long working life and a compact size.
- Measurement of impedance for 1:1 transformer using LCR meter under different combinations.

References

[1] G. C. S. E. A. B. I. Culbert and H. Dhirani, "Electrical insulation for rotating machines-design, evaluation, aging, testing, and repair," *the Institute of Electrical and Electronics Engineer Inc.*, 2004.

[2] D. L. A. B. S. Nategh, D. Barber and O. Aglen., "Review and trends in traction machine design: Primary and secondary insulation systems," *2018 XIII International Conference on traction machine s (ICEM), Alexandroupoli*, pp. pp. 2607–2612, 2018.

[3] Z. Huang, "Modeling and testing of insulation degradation due to dynamic thermal loading of electrical machines," *Doctoral Thesis*, pp. 20–21, 2017.

[4] `https://www.elantas.com/products-service/secondary-insulation.html`.

[5] F. S.-L. B. Jürgen H and J. Fleischer., *Handbook of Coil Winding*, vol. 1. 2018.

[6] `https://www.zeusinc.com/wp-content/uploads/2014/03/RESINATE_No3-PEEKInsWire_Zeus.pdf`.

[7] J. Mayer and D. Gerling, "Simulation of arbitrary fault-conditions in pm-machines by generalized unsymmetrical modeling," *2012 XXth International Conference on Electrical Machines*, 2012.

[8] M. Malekpour, B. Phung, and E. Ambikairajah, "Online technique for insulation assessment of induction motor stator windings under different load conditions," *IEEE Transactions on Dielectrics and Electrical Insulation*, vol. 24, no. 1, pp. 349–358, 2017.

[9] A. B. Peter Juris and B. Ponick, "A coupled thermalelectromagnetic energy consumption calculation for an electric vehicle with wheel hub drive considering different driving cycles," *IEEE Vehicle Power and Propulsion Conference*, 2012.

[10] P. J. Tanver and J. Penman, "Condition monitoring of traction machines," *U.K.: Research Studies Press*, 1987.

[11] A. Reinap and A. Upadhyay, "Specification of a specimen for accelerated thermal aging tests," in *2019 IEEE 12th International Symposium on Diagnostics for Electrical Machines, Power Electronics and Drives (SDEMPED)*, pp. 49–55, 2019.

[12] "Iec 60085 standard electrical insulation. thermal evaluation and designation," 2007.

Chapter 3

Condition monitoring techniques of ITF -A review

This chapter provides the current state of onboard condition monitoring techniques. Based on the nature and applicability, these techniques are classified into two categories namely, self analysis mode and traction mode. The purpose of this characterization is to provide automotive engineers a comprehensive overview of stator fault monitoring techniques and the know how of where, how and when can they be applied. Towards the end, futuristic trends of these monitoring techniques are discussed and based on existing research gap a new stator fault diagnostics method is proposed.

3.1 Background

The detection of the location and the assessment of the severity of inter-turn faults at an early stage is challenging. Several efforts are reported in the literature for the detection of stator faults. A review of both online and offline methods available for inter-turn fault detection in low-voltage induction machines (IM) is presented by Grubic [1, 3]. Various exhaustive surveys of online condition monitoring of stator faults for IM are presented in [2, 3]-[3, 3]. There are very few case studies available in the literature on reliability assessment of traction machines used in EV. Moreover, Gandhi [4, 3] and Arumugam [5, 3] present comprehensive studies for stator based faults, taking both the PMSM and IM into account.

Based on existing literature, this chapter aims to provide the automotive industry with a comprehensive survey of available onboard condition monitoring (OCM) tech-

niques for the stator insulation system, assessing their applicability to EV traction machines. Furthermore, a classification of the OCM techniques reviewed is proposed, according to whether they can be used while the machine is engaged for driving the vehicle or not. The proposed characterization structure, is divided in traction and stand still mode. The monitoring techniques can able to monitor faults under development (e.g. gradually changing insulation capacitance that can be detected by e.g.high frequency (HF) analysis) and developed faults (e.g. inter-turn faults that can be detected by e.g signature, sequence analysis or dynamic testing).

3.2 The condition monitoring technique

The determination of the State of Health (SOH) of the stator insulation system during the serviceable life of a traction machine helps ensuring a safe vehicle operation. Some of the condition monitoring techniques in the literature require that the machine is removed from the vehicle drive system and mounted on a dedicated test bench. For this reason, these techniques are dominated offboard condition monitoring techniques in this work. The most common offboard monitoring techniques to assess the stator turn-to-turn insulation are the surge test and the offboard partial discharge (PD) test [6, 3]. To test the phase-to-ground insulation, mostly the insulation resistance (IR) test, the polarization index test, the DC and AC high potential (HiPot) test [7, 3]-[8, 3] and the dissipation factor test are performed. The surge test and the AC and DC HiPot test are destructive in nature. The main drawback of offboard condition monitoring techniques is that they require the machine to be disassembled from the vehicle drivetrain, which generally is both time consuming and expensive. Additionally, they are not suitable for determining the running reliability of the traction machine, since they do not monitor the machine during operation. Nevertheless, since there are no significant differences in offboard condition monitoring techniques applied to EV traction machines compared to any other type of machine, the main focus of this chapter is on onboard condition monitoring techniques.

3.3 Onboard condition monitoring techniques and its classification

Onboard condition monitoring (OCM) techniques comprise those methods that can be applied after the traction machine is installed in the vehicle, using the existing equipment and sensors on-board. Depending on whether they are applicable or not while the traction machine is engaged in driving the vehicle, they can be classified into two different modes.

- **Self-analysis mode** - Self analysis mode can be activated at any time when the machine is not engaged for driving the vehicle. Functional and condition monitoring tests can be performed then. The main advantage of testing under self analysis mode is that the drivetrain does not need to comply with the driver's demands, and therefore pre-defined sequences of test currents and voltages could be supplied to the motor if needed. Some of these tests may require the machine to rotate, and in that case, it should be possible to mechanically disconnect the machine from the wheels.

  The state of health of a stator winding is not expected to deteriorate very fast, but at a rate that is expected to trend over days, weeks , months or even years. Thus, even though some of the proposed measurements can only be performed in self-analysis mode, they can be expected to run frequently enough to detect potential changes in the state of health of the insulation, depending on how often the vehicle is used.

- **Traction mode** - In traction mode, the drivetrain is in a state to be used for moving the vehicle, thus the machine can run at any relevant speed and torque level with respect to a drive cycle as required by the driver. However, there may still be room for running some additional condition monitoring tests while the machine is in operation. It is important to consider that in traction mode, the traction machine is subjected to all the normal external stresses which could interfere with the measurement processes performed by the condition monitoring methods.

Thus many measurements that only can be done in "self analysis mode" can be made daily since the vehicle is expected to be started at least once every day. In order to avoid complexity in the data logging and further processing its important to decide when or during what period its important to evaluate the healthiness of the stator insulation. Time duration for the test can vary like once in a week, once in a day or before every start of the vehicle called ignition. The monitoring technique which can be employed before the ignition of the vehicle are bundled under the category called self analysis mode. Therefore, testing and diagnostics under these two modes open up further research questions for future implementation.

3.4 OCM techniques under self analysis mode

Onboard SoH estimation of the insulation system is usually based on terminal parameters of the traction machine, for example the measurement of voltages, currents, the rotor angle and/or the derivatives of it and possibly vibration. Some tests like

the partial discharge (PD) test, the high frequency (HF) impedance analysis and the dynamic test can be performed in self analysis mode.

3.4.1 Partial discharge monitoring

Partial discharge is the localized dielectric breakdown of the voids present in the insulation system under high voltage stress. The root cause behind the voltage stress is the voltage derivative created by the high frequency switching converter. This stress is not uniformly distributed along the winding and it affects more the very first turns of the phase coil, significantly impacting its insulation system [9, 3].

Onboard monitoring of PD activity is done by tracking the partial discharge inception voltage (PDIV). PDIV is the voltage level at which PD starts. If the voltage surge is above the PDIV it will lead to PD appearance, which could in turn lead to insulation failure [9, 3]. According to [9, 3], a decrease in PDIV indicates an aged insulation. PDIV decreases also with a rise in temperature. For instance, if the temperature increases from 25^oC to 155^oC typically the PDIV decreases by 30%.

To measure PDIV, filters of increased steepness are recommended by IEC 61934 [10, 3]. There are few studies available in the literature concerning onboard PD monitoring for traction machines. Hammarström [11, 3] introduces a test setup designed to measure PDIV with different rise times of the applied voltage. In this setup, a smooth filter is employed to reduce the adverse effect of fast steep voltage fronts on motor insulation deterioration. However, to do onboard monitoring of PDIV additional equipment is needed [11, 3].

For these reasons, the implementation of an onboard PD monitoring system in EV is cumbersome and the availability of new advanced PD resistant insulation materials such as nanofilled enamels and impregnation resins [12, 3]-[13, 3] makes this method less attractive for onboard use.

3.4.2 HF impedance/inter-turn capacitance monitoring

To observe the aging process of the stator insulation system HF impedance monitoring is introduced in [14, 3]-[15, 3]. The deterioration of the inter-turn insulation can be detected by a change in the inter-turn capacitance. Usually the insulation resistance, dissipation factor and capacitance are used as indicators of the ageing process of the stator insulation [14, 3]. According to [14, 3], fault indicators can be obtained by measuring the differential leakage current at each phase of the stator. An aging related change in inter-turn capacitance of the stator insulation is reported by [16, 3]. Even a

small change in the impedance of the insulation system gives an indication of a stator fault under development.

In [16, 3], the high frequency leakage current is measured with a high frequency current sensor, having a bandwidth in the range of at least 7MHz. This frequency is a lot higher than what standard current sensors used in traction machines today can measure and thus implementing this method onboard requires additional HF currents sensors and the corresponding sampling capacity.

As it is not possible to use a HF impedance analyzer onboard, another way to monitor HF impedance is by injecting a small HF signal into the stator winding [15, 3]. The injected frequency must be close to the resonant frequency of the system. A magnetic probe, like a sense winding, kept in the vicinity of the winding can be used to measure the flux generated by the high frequency signal. The phase deviation between the injected signal and the measured flux gives an indication of the resonant frequency and hence the change in inter-turn capacitance can be calculated.

3.4.3 Machine characterization methods

Machine characterization methods (MCM) aim to identify the electromagnetic model of the traction machine by subjecting the machine to an intentional sequence of currents and speeds and measuring the response. There are mainly two types of machine characterization methods: dynamic testing methods (DTM) and standstill methods (SSM).

Dynamic testing

DTM can identify the magnetic model from the measurements when the machine accelerates or brakes. Through DTM, the electromagnetic parameters of the traction machine (inductance, permanent magnet flux linkage, and thus torque and flux linkage maps) can be obtained as a function of the stator current, usually expressed in the rotor reference frame. These methods consist on accelerating and decelerating the machine with a known current set-point and logging the evolution of the voltages, rotor position and speed with very high time resolution. From these logged signals, the machine properties are calculated in post-processing, and the whole test procedure can be conducted in just a few minutes[17, 3].

Standstill testing

SSM can be performed with or without rotor locking. In order to obtain the magnetic model, the machine excited with a hysteresis current controller which applies a square voltage wave to the machine. The flux can be calculated by integrating the volt-

age minus the voltage drop due to the stator resistance [18, 3]-[19, 3]. These methods generally perform well supposing that the square voltage wave alternates from positive to negative values with a high frequency. Nevertheless, when estimating fluxes, integration might cause drifting that must be considered.

3.5 OCM techniques under traction Mode

Monitoring under traction mode is advantageous as it provides constant monitoring during a traction cycle. This provides input to predictive maintenance, in detection of an incipient fault and in scheduling actions to avoid more severe process downtime. To detect the SoH of the stator insulation system while the vehicle is in operation several monitoring methods are developed [6, 3], [20, 3]-[21, 3] and described following.

3.5.1 Temperature monitoring

Constant monitoring of the temperature and its trending over time can be implemented both with and without dedicated sensors. Nowadays, most traction machines are embedded with temperature sensors at least in the windings and end-windings and possibly in the stator core. Sensors like PT100 (PT-platinum) resistance temperature detectors (RTD), optical fibre and theromcouples (J and K Type) are reported in [22, 3]-[23, 3].

Substantial work has been done also in estimating the temperature without using temperature sensors. This can be done by injecting HF voltages or currents [24, 3]-[25, 3], by analyzing the back EMF harmonics (BEMF) [26, 3], or with the help of a thermal model [27, 3]-[28, 3]. In the first two cases, the rate of change of the temperature is estimated by the change in stator winding resistance.

The HF injection test, estimates the temperature by injecting a carrier signal into the traction machine winding. The injected signal frequency is much higher than the fundamental frequency. Using the HF signal response, the winding temperature can be estimated from the HF resistance using a linear thermal model [24, 3]. In general, the carrier signal can either be a HF voltage or a HF current signal [25, 3].

BEMF based methods compute temperature using the temperature dependence of the permanent magnet flux linkage. Flux linkages can be estimated by measuring the machine terminal voltages and currents. In [26, 3], this technique is used to measure the mean temperature variation of the PM magnets.

Temperature estimation using available thermal models[27, 3]-[28, 3] is useful but

it requires precise knowledge of the machine geometry, materials, and the cooling system of the machine onboard [27, 3].

3.5.2 Vibration monitoring

Vibration monitoring methods are primarily used to detect mechanical and bearing related faults [29, 3]. However, some studies report the detection of inter-turn faults in the stator as well [30, 3], [31, 3]. This monitoring technique requires additional sensors (e.g. accelerometers) to detect vibration due to a shorted or inter-turn fault in the stator [30, 3]. As an example, the use of a vibration sensor with high sensitivity and sampling frequency of 25kHz is reported in [30, 3].

A shorted coil in the stator winding provides a lower resistance path to the current as compared to a healthy winding. Therefore, in a current controlled machine, the ohmic losses in the slots become lower and hence the temperature will be lower too. This lower temperature in the shorted slot combined with the higher temperatures in the healthy slots can lead to a thermal bend, which in turn leads to vibrations in the bearings as the machine rotates. The higher the difference in temperature, the higher the vibration level [31, 3].

Vibration signal monitoring yields good results in fault diagnosis, nevertheless the removal of background noise originated e.g. by the vehicle driving over uneven surfaces, is often considered a complex process.

3.5.3 Electromagnetic signature analysis

Electromagnetic signature analysis (ESA) is performed by monitoring the flux linkage in the machine winding. A healthy traction machine has a symmetrical flux distribution. However, stator and rotor faults create distortion in the flux distribution. To identify the unsymmetrical distribution of the flux in the airgap a search coil may be placed across each stator tooth [32, 3]-[33, 3]. The induced emf in the search coil is then integrated to obtain the flux linkage and its distribution. Alternatively, high resolution measurement or estimation of the terminal voltages and phase currents can be used to estimate the stator flux linkage, although not with as high spatial resolution as measurement coils on each tooth.

3.5.4 Motor current signature analysis

Motor current signature analysis (MCSA) is based on the analysis of the harmonic spectrum of the motor current, obtained by the fast Fourier transform (FFT) algorithm. The current harmonic spectrum changes after the development of a stator fault. Faults like stator winding short-circuits and eccentricities appear at specific frequencies in the current harmonic spectrum [34, 3].

A stator inter-turn fault can appear as a second harmonic in the stator current vector in a synchronously rotating reference frame [35, 3] or as a third harmonic in the phase current [36, 3], [37, 3] if the machine is supplied by a symmetric sinusoidal voltage system. With a high performing current control, the corresponding harmonics will instead appear in the machine terminal voltage. Automatic recognition of the inter-turn fault using pattern recognition based on artificial neural network (ANN) is also reported in [38, 3].

EV drive systems usually equipped with at least two current sensors on the stator winding phase. Therefore, MCSA has proven to be an efficient monitoring technique for stator insulation fault detection.

One of the main limitations of MCSA comes from the fact that FFT is only applicable to stationary signals, since it requires averaging the signal in time and then performing analysis in the frequency domain. However, due to the variable speed, it is not always possible to obtain stationary signals while the vehicle is in operation. When such non stationary signals are present, FFT is not a reliable technique for short-circuit fault detection[35, 3]-[37, 3].

To overcome this, short time Fourier transform (STFT), Wavelet transform (WT) or Wigner-Ville distribution (WVD) may be applied for spectrum estimation of non-stationary signals because of their ability to determine the occurrence time of each frequency component [39, 3]. The STFT provides the spectrum at a discrete time instant by using a fixed window function, at the cost of reduced signal resolution. To avoid signal resolution problems, wavelet was developed which has an adjustable window that automatically adjusts to give the most appropriate resolution[40, 3]-[41, 3].

Various papers have reported OCM of inter-turn or stator faults using discrete Wavelet transform (DWT) [42, 3]-[43, 3]. An effort to evaluate single inter-turn fault development and its severity by extracting the energy obtained from a external magnetic field using multidimensional DWT is reported in [44, 3] while the same problem is tackled by analyzing both FFT and DWT in [45, 3]. To consider speed variation for inter-turn fault development a separate study measuring and analyzing the torque

producing (quadrature) current using DWT is reported in [46, 3].

The main advantage of using WT is performing time frequency analysis and extracting the time at which the signature starts changing [47, 3]-[48, 3]. Another tracking algorithm, namely VoldKalman filtering order, is introduced and applied to track the harmonics of PMSM drives under non-stationary conditions in [43, 3]. However, the analysis of non stationary signals provides complex time-frequency characteristics during the transient state. Additionally, the performance limitations imposed by the sensors already existing in the vehicle drive and the need to know the base analytical frequencies or the base spectrum related to faults make these methods quite cumbersome in PMSM machines.

3.5.5 Power signature analysis

Power Signature analysis (PSA) is based on the spectral analysis of the instantaneous power [49, 3]. Unbalanced power at the output terminals of the traction machine gives an indication of unbalance in the supply voltage or current. A change in resistance due to contact surface damage, corrosion, excessive overheating or winding inter-turn short faults creates asymmetry in the phase current as presented by J.Yun [50, 3]. This resulting asymmetry in the phase current causes circulation of negative sequence current components, therefore reducing the motor power performance [51, 3]. PSA is considered to be less complex than MCSA and flux monitoring. However, the use of PSA for the determination of the insulation system's SoH or the diagnosis of faults is not widely accepted, and further development of this technique is needed in order to prove its reliability.

3.5.6 Monitoring of sequence components

Sequential component analysis is the classical way of converting unbalanced systems into three sets of symmetrical balanced systems known as positive, negative and zero sequence components (I1, I2, I0). To detect inter-turn faults and stator insulation health several methods using sequence component analysis are reported [52, 3]-[53, 3].

A stator insulation fault creates an asymmetry in the stator impedance that appears as an asymmetry in the phase current when supplied by a symmetric voltage, and an asymmetry in the phase voltage if the current is controlled instead, which is the case for EV traction machine drives. A way to detect these asymmetries is by using artificial neural networks (ANN) to analyze the voltages and currents as reported in [54, 3],[2, 3]. The asymmetries can be detected by signature analysis as discussed above, but also with sequence analysis. An asymmetric voltage contains negative sequence compo-

nents. In [55, 3], both positive and negative sequence components of the current and voltage are used to figure out the fault severity, location and fault type under vector control. Detection of inter-turn fault and its location is carried also by zero sequence component of voltage and current in [55, 3]. The zero sequence voltage component based diagnostics is appealing since it is independent of the unbalanced supply from the drive [56, 3]. However, this method needs access to the neutral point of the stator winding.

In conclusion,the perks and shortcomings of each and every monitoring technique under proposed self and traction mode is tabulated below.

Table 3.1: Classification Of OCM techniques under self analysis and Traction mode

OCM Techniques Under Self Analysis Mode			
References	Methods	Monitoring Parameter	Characteristics
[9, 3],[11, 3]	PD Test	PDIV- the voltage at which PD starts	(+) detects insulation failure,(-) Need filters on board
[14, 3]- [16, 3]	HF Impedance	IR, DF, leakage current and capacitance	(+) detection of inter-turn degradation,(-) requirement of HF current sensors having BW of at least 7MHz
[17, 3]- [19, 3]	Standstill and Dynamic testing	Inductance, torque, PM flux linkage, flux linkage maps	(+) quick calculation of machine properties using logged signals,(-) difficulty in measurement at high current when rotor unlocked
OCM Techniques Under Traction Mode			
[22, 3]- [28, 3]	Temperature	Temperature, HF voltage or current, Back EMF	(+) easy to perform due to inbuilt sensors, (-) sensor less measurement requires precise knowledge of the machine geometry and cooling system onboard
[29, 3]-[31, 3]	Vibration	Vibration	(-) requirement of sensors,(-) difficulty in removal of background noise
[32, 3]- [51, 3]	Signature Analysis	Flux linkage, current, and instantaneous power	(+) availability of current sensors on EV board makes it efficient,(-) interpretation of result become difficult due to current control
[52, 3]-[53, 3]	Sequence Component Analysis	Positive, negative and zero sequence of Voltage and current	(+) detects turn-turn fault at steady state, (+) no sensors required (-) neutral of the machine has to be accessible

3.5.7 Quality assessment and proposal of new diagnostic method

There are six different diagnostics techniques under traction mode. The main aim of this section is to assess the monitoring technique in terms of fault identification (FI), fault severity (FS) and sensor-less (SL) operation. When comparing different monitoring techniques the most significant characteristics are assigned as performance indicators. In order to make the decision the diagnostic methods are assessed by these performance indices (PIs). To understand each performance indicators like FI, FS and SL a short descriptions is provided below-

- **Fault identification (FI)** : Whether the OCM technique could able to locate and determine the fault or not. Such as single phase fault, coil fault, phase to phase fault or open circuit fault.
- **Fault severity (FS)** : Whether the machine performance compromised by the fault or not.
- **Sensor-less (SL)** : Whether the traction machine need extra sensors on board or not for extracting fault signals.

Temperature monitoring - To identify stator fault and its severity, temperature monitoring would need precise thermal sensors allocation across the winding. The rise in temperature across winding are due to number of factors like change in ac resistance of the winding at high frequency , change in supply , load conditions etc. this could affect the sensitivity of stator fault identification.

Vibration monitoring - Identification of stator fault via vibration could be possible by employing extra sensors on board. The test need to be conducted in controlled environment since the noise from the outside environment could interfere with fault detection and this considered as a major shortcoming of this method.

Signature analysis - Signature analysis can be done by electromagnetic signature analysis (ESA), motor current signature analysis(MCSA) and power signature analysis (PSA).

- **Flux signals (ESA)**: This method is promising in terms of FI, FS but so far in literature there is need to place search coil across the winding which will further adds to cost of implementation.
- **Current signals (MCSA)**: MCSA is considered to be suitable diagnostic method since the current signals will be provided by sensors on board and there will be no need for additional sensors. However, in EV drive system machine runs

under current control loop which makes the current harmonics to appear in terminal voltage.

- **Power signals (PSA)**: Fault diagnostics through power signals are not widely accepted due to its complexity.

Sequence component analysis - Asymmetrical three phase system give rise to three sequence component namely zero, positive and negative sequence components. Fault detection through zero sequence component of voltage in star connected winding is appealing since it is independent of unbalance in supply voltage but need the access to neutral point connection[56, 3]. Positive and negative sequence component of voltage could able to provide FI, FS and sensorless detection but at the cost of computational complexity.

Following is a list of the literature-based performance indicators for each monitoring technique:

Table 3.2: Quality Assessment Of OCM techniques in Traction mode under FOC control

Performance Indicators			
Monitoring Technique	FI	FS	SL
Temperature	×	×	✓
Vibration	✓	×	✓
Sequence component analysis			
Terminal voltage and Flux	✓	✓	×
Current	×	×	✓
Signature component analysis			
Terminal voltage and Flux	✓	✓	✓
Current	×	×	✓
Power	×	×	✓

As a result of the above assessment, in this thesis, the stator flux linkage is identified as the main diagnostic parameter and a detection methodology based on the vector decomposition of stator flux linkage is proposed.

Regarding stator flux diagnostics, both sensors and sensor-less monitoring of ITF have been done in literature. Sensors like hall effect and search coils [32, 3],[33, 3],[57, 3] are most commonly used for ITF diagnosis besides its extra size, complex installation, and additional cost, etc. On the other hand, sensor less diagnostics of ITF via SFL are about finding fault signatures in the frequency domain [42, 3],[58, 3] which includes more complicated decision making algorithms (such as machine learning models or artificial neural network (ANN) based model) to identify and classify the extracted fault signatures.

To address the limitations of current research, a simple method of detecting stator ITF is proposed using SFL vector component analysis without the need for additional sensors or without using any complicated ANNs or FFTs. This proposed diagnostic methodology is detailed in chapter 4 .

3.6 Futuristic trends in monitoring

Commercial electric drivetrains are developed to a high state of functionality. Torque and power density, efficiency, torque quality and controllability fulfill very high requirements. Prediction of lifetime on the design table under expected operating conditions and, once in operation, estimation of the remaining lifetime, also called condition monitoring, under actual operating conditions leave room for further development.

The starting point is lifetime prediction based on the sensors normally available for traction drive control, with their limitations in number and performance like bandwidth or resolution. Still there are several different types of condition monitoring techniques that can be applied to a drive system in a vehicle, like sequence analysis to detect winding insulation failures or dynamic testing to determine torque- and flux maps that can be used for both controller tuning and health evaluation. These kinds of functionality can be expected to be a part of EV drivetrains in a near future, since no additional hardware or no higher sensor specifications is required.

To take condition monitoring to a higher level, tests like HF impedance analysis of PD analysis must be adopted. Such testing methods require improved sensors, like current sensors with higher bandwidth and maybe higher resolution, switches that can reconfigure the stator winding for PD analysis, vibration sensors etc. All these changes increase the cost of the drive train and the value of the deepened insight in the SoH of a traction machine drive must be balanced against the increased cost. Nevertheless, it can be expected that the condition monitoring capabilities of future traction machine drives will improve as the components cost fall. The voltage level used in EV drive trains is increasing towards, and maybe beyond, 1kV implying that isolation material issues can be expected to increase and then also the motivation to monitor the condition more closely.

3.7 Summary

A comprehensive review of onboard condition monitoring methods is presented. Special focus is laid on methods that can be applied to traction machines whilst still assembled in their intended application, here referred to as onboard condition monitoring (OCM) methods. A classification is proposed distinguishing between self analysis mode and traction mode. An overview of the proposed diagnostic method is provided, as well as a comparison with those currently in use. A quality assessment is conducted based on performance indicators. The terminal voltage or SFL considered as a promising monitoring parameter for ITF detection. Futuristic trends describe the extent and capacity of OCM in commercially available vehicles in the near future.

3.8 Learning outcomes

This characterization helps build understanding for monitoring the stator insulation system while the vehicle is moving and not moving. An obvious challenge is data logging in standstill monitoring, such as how often (daily, weekly, monthly or annually) you want to see the SoH of the stator insulation system tested.

References

[1] B. L. S. Grubic, J. Aller and T. Habetler, "A survey on testing and monitoring methods for stator insulation systems of low-voltage induction machines focusing on turn insulation problems," *IEEE Transactions on Industrial Electronics*, vol. 55, no. 12, p. 4127–4136, 2008.

[2] G. S. G. K. J. Y. T. H. R. Tallam, S. B. Lee and R. Harley, "A survey of methods for detection of stator-related faults in induction machines," *IEEE Trans. Ind. Appl.,*, vol. 43, no. 4, p. 920–933, 2007.

[3] F. F. T. C. C. G. Bellini, A., "Advances in diagnostic techniques for induction machines," *IEEE Transactions on Industrial Electronics*, vol. 55, no. 12, pp. 4109–4126, 2008.

[4] T. C. A. Gandhi and L. Parsa, "Recent advances in modeling and online detection of stator interturn faults in electrical motors," *IEEE Transactions on Industrial Electronics*, vol. 58, no. 5, p. 1564–1575, 2011.

[5] P. A. T. Hamiti and C. Gerada, "Turn–turn short circuit fault management in permanent magnet machines," *IET Electronics Power Applications*, vol. 9, no. 9, p. 634–641, 2015.

[6] G. C. S. E. A. B. I. Culbert and H. Dhirani, "Electrical insulation for rotating machines-design, evaluation, aging, testing, and repair," *the Institute of Electrical and Electronics Engineer Inc.*, 2004.

[7] J. Geiman, "Dc step-voltage and surge testing of motors," *Maint. Technology*, vol. 3, no. 9, pp. 32–39, 2007.

[8] `https://www.atecorp.com/atecorp/media/pdfs/data-sheets/baker-st112a_manual.pdf`.

[9] IEC60085, "Standard electrical insulation. thermal evaluation and designation," 2007.

[10] IEC61934, "Electrical insulating materials and systems – electrical measurement of partial discharges (pd) under short rise time and repetitive voltage impulses," 2006.

[11] T. HammarstrÖm, "Partial discharges at fast rising voltages," *Doctoral Thesis Chalmers University Of Technology*, pp. 101–103, 2014.

[12] A. D. F. Guastavino, E. Torello and A. Ratto, "Life tests on twisted pair specimens insulated by nanofilled enamel," *Annual Report Conference on Electrical insulation and Dielectric Phenomena, Quebec, QC*, pp. 678–681, 2008.

[13] S. S. F. Guastavino, A. Ratto and E. Torello, "Electrothermal aging tests on different kinds of enamelled wires," *10th IEEE International Conference on Solid Dielectrics, Potsdam*, pp. 1–4, 2010.

[14] K. Y. S.-B. Lee, J. Yang and R. M. Bharadwaj, "An online groundwall and phase-to-phase insulation quality assessment technique for ac-machine stator windings," *IEEE Trans. Industrial Applications*, vol. 42, no. 4, p. 946–957, 2006.

[15] R. C. P. Werynski, D. Roger and J. F. Brudny, "Proposition of a new method for in-service monitoring of the aging of stator winding insulation in ac motors," *IEEE Transactions Energy Conversions*, vol. 21, no. 3, p. 673–681, 2006.

[16] J. Björngreen, "Pmsm diagnostics and prognostics," *Master's thesis, Lund University*, 2016.

[17] R. M. K. S. Wiedemann, S. Hall and M. Alaküla, "Dynamic testing characterization of a synchronous reluctance machine," *IEEE Transactions on Industry Applications*, vol. 54, no. 2, pp. 1370–1378, March-April 2018.

[18] S. C. N. Bedetti and R. Petrella, "Stand-still self-identification of flux characteristics for synchronous reluctance machines using novel saturation approximating function and multiple linear regression," *IEEE Transactions on Industry Applications*, vol. 52, no. 4, pp. 3083–3092, July 2016.

[19] S. Wiedemann and R. M. Kennel, "Encoderless self-commissioning and identification of synchronous reluctance machines at standstill," *IEEE 26th International Symposium on Industrial Electronics (ISIE),*, pp. 296–302, june 2017.

[20] M. A. A. Flach, F. Draeger and L. Brabetz, "A new approach to diagnostics for permanent-magnet motors in automotive power train systems," *8th IEEE Symposium on Diagnostics for Electrical Machines, Power Electronics and Drives*, pp. 234–239, 2011.

[21] S. B. O. B. Akin and H. A. Toliyat, "On-board fault diagnosis of hev induction motor drive at start-up and during idle mode," *2007 IEEE Vehicle Power and Propulsion Conference, Arlington, TX,*, pp. 140–147, 2007.

[22] R. Rothe and K. Hameyer, "Life expectancy calculation for electric vehicle traction machine s regarding dynamic temperature and driving cycles," *2011 IEEE International Electric Machines and Drives Conference (IEMDC), Niagara Falls*, pp. 1306–1309, 2011.

[23] J. L. X. Ding and C. Mi, "Online temperature estimation of ipmsm permanent magnets in hybrid electric vehicles," *6th IEEE Conference on Industrial Electronics and Applications, Beijing*, pp. 179–183, 2011.

[24] Y. Wu and H. Gao, "Induction-motor stator and rotor winding temperature estimation using signal injection method," *IEEE Transactions on Industry Applications*, vol. 42, no. 4, pp. 1038–1044, July-Aug. 2006.

[25] K. L. V. I. G. Feng, C. Lai and N. C. Kar, "Improved high-frequency voltage injection based permanent magnet temperature estimation for pmsm condition monitoring for ev applications," *IEEE Transactions on Vehicular Technology*, vol. 67, no. 1, pp. 216–225, Jan. 2018.

[26] T. T. T. K. D. D. Reigosa, D. Fernandez and F. Briz, "Permanent-magnet temperature distribution estimation in permanent-magnet synchronous machines using back electromotive force harmonics," *IEEE Transactions on Industry Applications*, vol. 52, no. 4, pp. 3093–3103.

[27] W. P. T. Huber and J. Böcker, "Monitoring critical temperatures in permanent magnet synchronous motors using low-order thermal models," *International Power Electronics Conference (IPEC-Hiroshima 2014 - ECCE ASIA), Hiroshima*, pp. 1508–1515, 2014.

[28] O. Wallscheid and J. Böcker, "Global identification of a low-order lumped-parameter thermal network for permanent magnet synchronous motors," *IEEE Transactions on Energy Conversion*, vol. 31, no. 1, pp. 354–365, 2016.

[29] R. Randall, "Developments in digital analysis techniques for diagnostics of bearings and gears," *Fifth International Congress on Sound and Vibration, Adelaide, South Australia*, 1997.

[30] X. S. Z. Yang and M. Krishnamurthy, "Vibration monitoring of pm synchronous machine with partial demagnetization and inter-turn short circuit faults," 2014 ieee transportation electrification conference and expo (itec), dearborn," *Fifth International Congress on Sound and Vibration, Adelaide, South Australia*, pp. 1–6, 2014.

[31] J. F. M. Ebrahimi, "Vibration monitoring of pm synchronous machine with partial demagnetization and inter-turn short circuit faults," *IET Electrical Power Application*, vol. 6, no. 1, pp. 35–45, 2012.

[32] X. S. Y. Da and M. Krishnamurthy, "A new approach to fault diagnostics for permanent magnet synchronous machines using electromagnetic signature analysis," *IEEE Transactions on Power Electronics*, vol. 28, no. 8, pp. 4104–4112, 2013.

[33] P. Neti and S. Nandi, "Stator inter-turn fault detection of synchronous machines using field current and rotor search-coil voltage signature analysis," *IEEE Transactions on Industry Applications*, vol. 45, no. 3, p. 911–920, May/Jun. 2009.

[34] A. V. J. S. Praneeth and S. S. Williamson, "Algorithm for prediction and control of induction motor stator interturn faults in electric vehicles," *IEEE Transportation Electrification Conference and Expo (ITEC), Chicago*, pp. 130–134, 2017.

[35] M. A. S. Nejad and M. Taghipour, "Inter-turn stator winding fault diagnosis and determination of fault percent in pmsm," *IEEE Applied Power Electronics Colloquium (IAPEC)*, pp. 128–131, 2011.

[36] J. R. R. L. R. H. Saavedra, J. C. Urresty, "Detection of interturn faults in pmsms with different winding configurations," *Energy Conversion and Management*, pp. 534–542, 2014.

[37] S. N. Q. Wu, "Fast single-turn sensitive stator winding inter-turn fault detection of induction machines based on positive- and negative-sequence third harmonic components of line currents," *IEEE Transactions on Industry Applications*, vol. 46, no. 3, 2010.

[38] M. A. F. Çira and B. Gümüş, "A new approach to detect stator fault in permanent magnet synchronous motors," *IEEE 10th International Symposium on Diagnostics for traction machine s, Power Electronics and Drives (SDEMPED)*, pp. 316–321, 2015.

[39] H. H. S. H. Kia and G. Capolino, "Digital signal processing for induction machines diagnosis - a review," *IECON 2007 - ccrd Annual Conference of the IEEE Industrial Electronics Society, Taipei*, pp. 1155–1162, 2007.

[40] P. P. H. Douglas and A. K.Ziarani, "A new algorithm for transient mcsa using wavelets," *IEEE Transactions on Industry Applications*, vol. 40, no. 5, 2004.

[41] `http://users.rowan.edu/~polikar/WTpart1.html`.

[42] R. R. H. Cherif, A. Menacer and R. Pusca, "Dispersion field analysis using discrete wavelet transform for inter-turn stator fault detection in induction motors," *IEEE 11th International Symposium on Diagnostics for traction machines, Power Electronics and Drives (SDEMPED)*, pp. 104–109, 2017.

[43] J. R. J. Urresty and L. Romeral, "Diagnosis of interturn faults in pmsms operating under nonstationary conditions by applying order tracking filtering," *IEEE Transactions on Power Electronics*, vol. 28, no. 1, pp. 507–515, 2013.

[44] A. D. S. S. Moosavi, Q. Esmaili and Y. A. Amirat, "Inter-turn fault detection in stator winding of pmsm using wavelet transform," *2017 IEEE Vehicle Power and Propulsion Conference (VPPC), Belfort*, pp. 1–5, 2017.

[45] B. A. M. Heydarzadeh, M. Zafarani and M. Nourani, "A wavelet-based fault diagnosis approach for permanent magnet synchronous motors," *IEEE Transactions on Energy Conversion*.

[46] J. C. A. G. J. A. Rosero, L. Romeral and J. A. Ortega, "On the short-circuiting fault detection in a pmsm by means of stator current transformations," *IEEE Power Electronics Specialists Conference, Orlando, FL, 2007*, pp. 1936–1941, 2007.

[47] B. T. P. M. Malekpour and E. Ambikairajah, "Diagnosis of stator winding insulation failure in induction motors shortly after its occurrence," *International Conference on Condition Monitoring and Diagnosis (CMD)*, pp. 485–488, 2016.

[48] M. R.-G. S. B. L. T. K. J. Pons-Llinares, J. Antonino-Daviu and C. Yang, "Use of discrete and optimized continuous tfd tools for transient-based diagnosis in controversial fault cases," *9th IEEE International Symposium on Diagnostics for Electric Machines, Power Electronics and Drives (SDEMPED), Valencia*, pp. 114–121, 2013.

[49] R. A. K. G. B. Kliman, W. J. Premerlani and D. Hoeweler, "A new approach to on-line turn fault detection in ac motors," *Conf. Rec. c1st IEEE IAS Annu. Meeting*, vol. 1, no. 1, pp. 687–693, 1996.

[50] K. L. S. B. L. J. Yun, K. Lee and J. Yoo, "Detection and classification of stator turn faults and high-resistance electrical connections for induction machines," *IEEE Transactions on Industry Applications*, vol. 45, no. 2, pp. 666–675, March-April 2009.

[51] A. H. M. S. U. S. F. Legowski and A. M. Trzynadlowski, "Instantaneous power as a medium for the signature analysis of induction motors," *IEEE Transactions on Industry Applications*, vol. 32, pp. 904–909, 1996.

[52] M. B. K. Bouzid and G. Champenois, "New expressions of symmetrical components of the induction motor under stator faults," *IEEE Transactions on Industry Applications*, vol. 60, no. 9, pp. 4093–4102, 2013.

[53] B. G. C. N.Leboeuf, T.Boileau and F. Meibody-Tabar, "Real-time detection of interturn faults in pm drives using back-emf estimation and residual analysis," *IEEE Transactions on Industry Applications*, vol. 47, no. 6, pp. 2402–2412, Nov.-Dec. 2011.

[54] T. G. H. R. M. Tallam and R. G. Harley, "Self-commissioning training algorithms for neural networks with applications to electric machine fault diagnostics," *IEEE Trans. Power Electron.*, vol. 17, no. 6, p. 1089–1095, Nov. 2002.

[55] H. L. H. Jeong, S. Moon and S. W. Kim, "Interturn short circuit fault detection of permanent magnet synchronous motors based on positive- and negative-sequence signatures," *IEEE 11th International Symposium on Diagnostics for traction machine s, Power Electronics and Drives (SDEMPED), Tinos*, pp. 167–172, 2017.

[56] M. C. J. Hang, J. Zhang and J. Huang, "Online interturn fault diagnosis of permanent magnet synchronous machine using zero-sequence components," *IEEE Transactions on Power Electronics*, no. 12, pp. 1627–1632, 2015.

[57] Y. Park, "On-line detection and classification of rotor and load defects in pmsms based on hall sensor measurements," *IEEE Energy Conversion Congress and Exposition (ECCE), Portland, OR*, pp. 716–721, 2018.

[58] B. M. Ebrahimi and J. Faiz, "Feature extraction for short-circuit fault detection in permanent-magnet synchronous motors using stator-current monitoring," *IEEE Trans. Power Electron.*, vol. 25, no. 10, p. 2673–2682, Oct. 2010.

Chapter 4

The proposed diagnostic technique

This chapter briefly describe the vector control and how it is used in combination with PMSM machines to control the speed and torque. Since the proposed diagnostic would be part of it later on its important to lay out the details beforehand. Following that, the proposed diagnostic techniques are described in detail, along with their block diagram representations. The proposed diagnostic scheme is described using stator flux vector diagram and mathematically using the symmetric three phase supply and asymmetric three phase supply, and later the concept is evaluated using simulink.

4.1 Vector control of PMSM

Vector control, also known as field-oriented control (FOC), is a method used in the control of AC motors, particularly induction motors and permanent magnet synchronous motors (PMSMs). The goal of vector control is to manage the motor's torque and magnetic flux independently, similar to the way DC motors are controlled.

From a synchronous coordinate system attached to the rotor position, the rotating current vector is composed of two dc components along the d and the q axis of the rotating frame, which can be controlled independently.i_d current is used to control and adjust the flux in the d axis while i_q is responsible to control the desired torque in motors. In its simplest form, only the q-currents are used for torque control, but in more advanced drives unique combinations of d and q currents are used, particularly for field weakening operation[1, 4].

The basic scheme of PMSM vector control is presented in Figure 4.1.

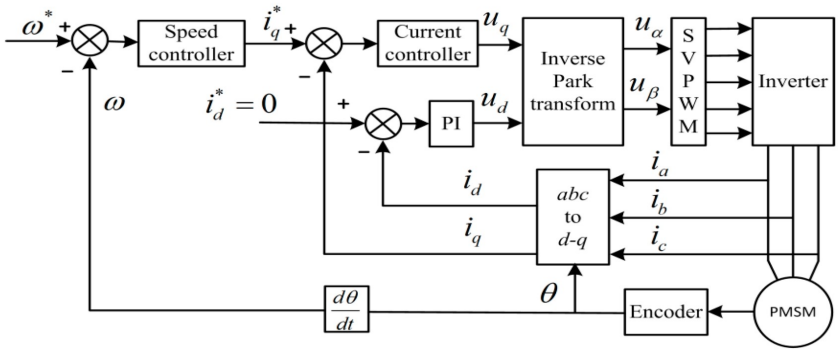

Figure 4.1: The block diagram of vector controlled PMSM [2, 4]

Thus the stator currents cannot be expected to be significantly impacted by isolation faults, as long as the current control system is working as intended, so the fundamental frequency currents and sequence components cannot be used to monitor inter-turn faults. However, it is possible to observe a change in characteristics of a motor by analyzing stator voltages and the integrals of these voltages, the Stator Flux Linkage (SFL). Based on this fundamental a new diagnostic scheme is proposed to detect incipient ITF faults. The following section discusses in detail the vector control strategy that is the foundation of the proposed fault detection scheme.

4.2 Proposed diagnostic technique

The proposed method is based on detection of the dc offset of the SFL vector in the antisynchronous reference frame (ASRF). The DC offset of the SFL is calculated by estimating the SFL in the stator reference frame, transforming it to an ASRF, and low-pass filtering it.

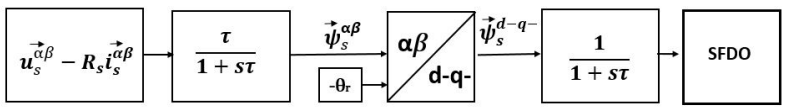

Figure 4.2: The complete block diagram of the proposed method

It is possible to simplify the proposed method by looking at each step separately. There are three steps involved in obtaining the diagnostic parameter "SFDO". Following is a breakdown of the steps:

Step 1-

The stator flux linkages can be calculated by the integral of the voltage drop in stationary reference frame as:

$$\overrightarrow{\psi_s}^{\alpha\beta} = \int (\overrightarrow{u_s}^{\alpha\beta} - R_s \overrightarrow{i_s}^{\alpha\beta}) dt \tag{4.1}$$

Therein $\overrightarrow{u_s}^{\alpha\beta}$ denotes the inverter voltage vector as $\overrightarrow{u_s}^{\alpha\beta} = u_\alpha + j u_\beta$, R_s is the stator resistance, $\overrightarrow{i_s}^{\alpha\beta}$ is the machine terminal current vector in stationary reference frame as $\overrightarrow{i_s}^{\alpha\beta} = i_\alpha + j i_\beta$ and $\overrightarrow{\psi_s}^{\alpha\beta}$ is the stator flux linkages vector as $\overrightarrow{\psi_s}^{\alpha\beta} = \psi_\alpha + j\psi_\beta$.

This integral is difficult to perform in a real drive since both voltage and current values are subject to estimation/measurement error and the stator resistance varies with both frequency and temperature. Acknowledging that small errors will lead to a drift in the integral, the integral should be high-pass filtered (HPF).High pass filtering of an integral equals low pass filtering of the integrand. Thus, a SFL estimate in stationary reference frame is estimated by low pass filtering the integrand multiplied with a gain as a time constant as shown in Figure 4.3 where τ is the time constant.

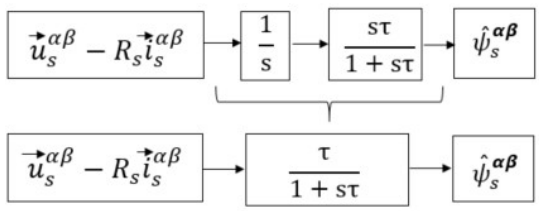

Figure 4.3: Block diagram used to obtain the SFL in stationary reference frame

Low pass filtering can be made with a physical LPF which is fed with the real output voltage of a converter and the measured phase currents [3, 4], or in software only using an estimate of the stator voltage including compensation for dead times, rise and fall times and semiconductor voltage drops.

Step 2-

In the next step, transforming the stationary vectors into synchronous and anti-synchronous reference frames using Park vector transformation [4, 4], and pass these estimates to a low pass filter to obtain the diagnostic variable "Stator flux linkages dc offset" as SFDO.

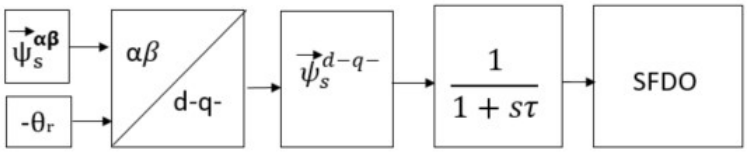

Figure 4.4: The block diagram for obtaining SFDO

In order to have an understanding of different reference frame an attempt is made by stator flux linkages vector analysis in the following subsection using the case study.

4.3 Mathematical Intrpretations

Three phase symmetric voltage supply - Under symmetric voltage supply to any three phase system or machine a three phase sinusoidal voltage source such that the voltage vector is taken to rotate at constant angular velocity ω.

$$\begin{cases} u_a = \hat{u_a} sin(\omega t) \\ u_b = \hat{u_b} sin(\omega t - \gamma) \\ u_c = \hat{u_c} sin(\omega t - 2\gamma) \end{cases} \tag{4.2}$$

Here, u_a, u_b, u_c, $\hat{u_a}$, $\hat{u_b}$, $\hat{u_c}$ denotes the instantaneous and peak value of the applied voltage in each phase *a, b, and c* respectively , ω represent the supply voltage frequency and the phase shift of the phase is represented by γ=$\frac{2\pi}{3}$.

The three phase symmetric stator flux linkages obtained from a three phase symmetric sinusoidal voltage supply applied to PMSM are given below and can be found using

$$u_j(t) = R_j i_j(t) + \frac{\mathrm{d}\psi_j(t)}{\mathrm{d}t} \tag{4.3}$$

Therein $u_j(t)$ denotes the three phase voltage , R_j is the stator winding resistance across each phase , i_j is the three phase current and ψ_j is the stator flux linkage of three phase $j\epsilon$ *a,b,c.* The time is denoted by t. The stator flux linkages to each phase is given below:

$$\begin{cases} \psi_a = \hat{\psi}_a cos(\omega t + \delta_a) \\ \psi_b = \hat{\psi}_b cos(\omega t + \delta_b - \gamma) \\ \psi_c = \hat{\psi}_c cos(\omega t + \delta_c - 2\gamma) \end{cases} \tag{4.4}$$

Here, ψ_a, ψ_b, ψ_c, $\hat{\psi}_a$, $\hat{\psi}_b$, $\hat{\psi}_c$ denotes the instantaneous and peak value of SFL in each phase *a, b, and c* respectively. δ_a, δ_b, δ_c represents the phase difference due to applied load in each phase *a, b, and c* respectively.

The space vector diagram- of stator flux linkages in stationary, synchronous (*dq*) and anti synchronous (*d-q-*) reference frame is illustrated in the Figure 4.5.

The figure composed of three complex planes. First stator based complex plane also known as stationary frame of reference with axis of α and β. The SFL vector linked with the stationary frame of reference can be expressed in terms of there components (shown in Figure 4.5 with indigo lines) seen by each winding namely -

$$\overrightarrow{\psi_s}^{\alpha\beta} = \psi_\alpha + j\psi_\beta \tag{4.5}$$

A second complex plane with axis *d and q* which is like an axis tied to the rotor [5, 4].The SFL vector linked with the rotor frame of reference can be expressed in terms of there components (shown in Figure 4.5 with sky blue lines) seen by each winding namely :

$$\overrightarrow{\psi_s}^{dq} = \psi_d + j\psi_q \tag{4.6}$$

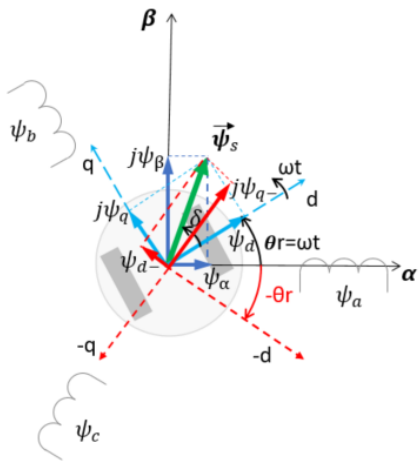

Figure 4.5: An overview of a SFL vector components

A third complex plane with axes *d-* and *q-* rotating in the opposite(reverse) direction to the rotor. The SFL vector linked with the anti rotor frame of rotation can be expressed in terms of there components (shown in Figure 4.5 with red lines) seen by each winding namely :

$$\overrightarrow{\psi_s}^{d-q-} = \psi_{d-} + j\psi_{q-} \tag{4.7}$$

In Figure 4.5, the superscript from the SFL vector is omitted to simplify the graphical representation.

The relationship between the stator and rotor oriented linkage space vectors as ;

$$\overrightarrow{\psi_s}^{dq} = \overrightarrow{\psi_s} e^{-j(\theta_r)} \tag{4.8}$$

where, θ_r is the angle between the stationary and rotating complex plane. In case when the complex plane is rotating in the reverse rotor direction then the rotor linked spaced vector as ;

$$\overrightarrow{\psi_s}^{d-q-} = \overrightarrow{\psi_s} e^{-j(-\theta_r)} = \overrightarrow{\psi_s} e^{j(\theta_r)} \tag{4.9}$$

The symmetric SFL in stationary reference frame($\alpha\beta$) -

The space vector formulation in its general form is given by equation:

$$\overrightarrow{x} = \sqrt{\frac{2}{3}}[x_a + x_b e^{j\gamma} + x_c e^{j2\gamma}] \tag{4.10}$$

The variables x_a, x_b and x_c represent three phase instantaneous time dependant supply variables. Substituting these instantaneous values into the expression of general space vectors while considering the assumption of symmetry as written in equation 4.11 is result into equation 4.12

$$\hat{\psi} = \hat{\psi_a} = \hat{\psi_b} = \hat{\psi_c}; \delta = \delta_a = \delta_b = \delta_c; \tag{4.11}$$

$$\overrightarrow{\psi_s}^{\alpha\beta} = \sqrt{\frac{2}{3}}\hat{\psi}[cos(\omega t + \delta) + cos(\omega t + \delta - \gamma)e^{j\gamma} + cos(\omega t + \delta - 2\gamma)e^{j2\gamma}] \tag{4.12}$$

according to Euler's law cosx can be replaced by $cos(x) = \frac{e^{jx}+e^{-jx}}{2}$;

can be substituted and the space vector equation become as-

$$\begin{aligned}\overrightarrow{\psi_s}^{\alpha\beta} =& \sqrt{\frac{2}{3}}\hat{\psi}[\frac{e^{j(\omega t+\delta)} + e^{-j(\omega t+\delta)}}{2} + \frac{e^{j(\omega t+\delta-\gamma)} + e^{-j(\omega t+\delta-\gamma)}}{2}e^{j\gamma} \\ &+ \frac{e^{j(\omega t+\delta-2\gamma)} + e^{-j(\omega t+\delta-2\gamma)}}{2}e^{j2\gamma}]\end{aligned}$$

By solving the above equation the vector equation becomes;

$$\overrightarrow{\psi}_s^{\alpha\beta} = \sqrt{\frac{2}{3}}.\frac{3}{2}\hat{\psi}e^{j(\omega t+\delta)} + \sqrt{\frac{2}{3}}.\frac{3}{2}\hat{\psi}\underbrace{(e^{-j(\omega t+\delta)} + e^{-j(\omega t+\delta-2\gamma)} + e^{-j(\omega t+\delta-4\gamma)})}_{\text{vector sum is zero}} \tag{4.13}$$

The second term in the right hand side of equation 4.13 is zero, given that this term is formed by three vectors of the same amplitude which are phase shifted with respect to each other by γ.

Therefore the SFL vector under symmetric supply is expressed as a vector with constant amplitude and frequency, and rotates with an angular speed ω as seen from the stationary $(\alpha\beta)$ reference frame when driven by a sinusoidal a symmetrical three-phase system.

$$\overrightarrow{\psi}_s^{\alpha\beta} = \sqrt{\frac{3}{2}}\hat{\psi}e^{j(\omega t+\delta)} \tag{4.14}$$

An asymmetric SFL in stationary reference frame$(\alpha\beta)$ -

In the case of asymmetry, if one of the phase flux linkages is different in amplitude or phase from the other phases in the provided case is the amplitude and the phase of phase *c* as shown in equation 4.15. Particularly with inter-turn faults, the flux linkage to the faulted phase decreases to align the thought later with reality. The decrease in flux linkages appears to indicate the change in phase *c* flux linkage.

$$\hat{\psi_x} = \hat{\psi}, \hat{\psi_c} \neq \hat{\psi}, \hat{\psi_c} = \hat{\psi} - \Delta\hat{\psi}, \delta_x = \delta, \delta_c \neq \delta, \delta_c = \delta + \Delta\delta \tag{4.15}$$

Substituting above:

$$\begin{aligned}\overrightarrow{\psi_s}^{\alpha\beta} =& \sqrt{\frac{2}{3}}\hat{\psi}\left(\frac{e^{j(\omega t+\delta)} + e^{-j(\omega t+\delta)}}{2} + \frac{e^{j(\omega t+\delta-\gamma)} + e^{-j(\omega t+\delta-\gamma)}}{2}e^{j\gamma}\right) \\ &+ \sqrt{\frac{2}{3}}(\hat{\psi} - \Delta\hat{\psi})\left(\frac{e^{j(\omega t+\delta+\Delta\delta-2\gamma)} + e^{-j(\omega t+\delta+\Delta\delta-2\gamma)}}{2}e^{j2\gamma}\right)\end{aligned} \tag{4.16}$$

Simplifying using $e^{j4\gamma} = e^{j\gamma}$:

$$\begin{aligned}\overrightarrow{\psi_s}^{\alpha\beta} =& \sqrt{\frac{2}{3}}\frac{\hat{\psi}}{2}\Bigg(2e^{j(\omega t+\delta)} + e^{-j(\omega t+\delta)} + e^{-j(\omega t+\delta-2\gamma)}) \\ &+ (1 - \frac{\Delta\hat{\psi}}{\hat{\psi}})(e^{j(\omega t+\delta+\Delta\delta)} + e^{-j(\omega t+\delta+\Delta\delta-\gamma)}\Bigg)\end{aligned} \tag{4.17}$$

Next step is to simplify it further by adding and subtracting $e^{j(\omega t+\delta)}$ and $e^{-j(\omega t+\delta-\gamma)}$

$$\begin{aligned}\overrightarrow{\psi}_s^{\alpha\beta} =&\sqrt{\frac{2}{3}}\frac{\hat{\psi}}{2}\Bigg(2e^{j(\omega t+\delta)}+e^{-j(\omega t+\delta)}+e^{-j(\omega t+\delta-2\gamma)}+e^{j(\omega t+\delta)}.e^{j(\Delta\delta)}\\&+\underbrace{(e^{j(\omega t+\delta)}-e^{j(\omega t+\delta)})}+e^{j(\omega t+\delta-\gamma)}.e^{-j(\Delta\delta)}+\underbrace{(e^{-j(\omega t+\delta-\gamma)}-e^{-j(\omega t+\delta-\gamma)})}\\&-\frac{\Delta\hat{\psi}}{\hat{\psi}}(e^{j(\omega t+\delta)}.e^{j(\Delta\delta)}+e^{-j(\omega t+\delta-\gamma)}.e^{-j(\Delta\delta)})\Bigg)\end{aligned} \tag{4.18}$$

$$\begin{aligned}\overrightarrow{\psi}_s^{\alpha\beta} =&\sqrt{\frac{2}{3}}.\frac{3}{2}\hat{\psi}e^{j(\omega t+\delta)}+\sqrt{\frac{2}{3}}\frac{\hat{\psi}}{2}\underbrace{(e^{-j(\omega t+\delta)}+e^{-j(\omega t+\delta-2\gamma)}+e^{-j(\omega t+\delta-\gamma)})}_{\text{vector sum is zero}}+\\&\sqrt{\frac{2}{3}}\frac{\hat{\psi}}{2}\Bigg(e^{-j(\omega t+\delta-\gamma)}.(e^{-j(\Delta\delta)}-1)+e^{j(\omega t+\delta)}.(e^{j(\Delta\delta)}-1)-\frac{\Delta\hat{\psi}}{\hat{\psi}}(e^{j(\omega t+\delta)}.e^{j(\Delta\delta)}\\&+e^{-j(\omega t+\delta-\gamma)}.e^{-j(\Delta\delta)})\Bigg)\end{aligned} \tag{4.19}$$

$$\begin{aligned}\overrightarrow{\psi}_s^{\alpha\beta} =&\sqrt{\frac{3}{2}}\hat{\psi}e^{j(\omega t+\delta)}+\sqrt{\frac{2}{3}}\frac{\hat{\psi}}{2}(e^{j(\omega t+\delta)}(e^{j(\Delta\delta)}-1)+e^{-j(\omega t+\delta-\gamma)}(e^{-j(\Delta\delta)}-1))\\&-\sqrt{\frac{2}{3}}\frac{\Delta\hat{\psi}}{2}(e^{j(\omega t+\delta)}.e^{j(\Delta\delta)}+e^{-j(\omega t+\delta-\gamma)}.e^{-j(\Delta\delta)})\end{aligned} \tag{4.20}$$

$$\overrightarrow{\psi}_s^{\alpha\beta} =\begin{cases}\Delta\hat{\psi}=\Delta\delta=0\rightarrow\sqrt{\frac{3}{2}}\hat{\psi}e^{j(\omega t+\delta)}\\\Delta\hat{\psi}\neq 0;\Delta\delta=0\rightarrow\sqrt{\frac{3}{2}}\hat{\psi}e^{j(\omega t+\delta)}-\sqrt{\frac{2}{3}}\Delta\hat{\psi}\frac{(e^{j(\omega t+\delta)}+e^{-j(\omega t+\delta-\gamma)})}{2}\\\Delta\hat{\psi}\neq 0;\Delta\delta\neq 0\rightarrow\sqrt{\frac{3}{2}}\hat{\psi}e^{j(\omega t+\delta)}+\\\sqrt{\frac{2}{3}}(\hat{\psi}-\Delta\hat{\psi})\frac{(e^{j(\omega t+\delta+\Delta\delta)}+e^{-j(\omega t+\delta+\Delta\delta-\gamma)})}{2}-\sqrt{\frac{2}{3}}\hat{\psi}\frac{(e^{j(\omega t+\delta)}+e^{-j(\omega t+\delta-\gamma)})}{2}\end{cases} \tag{4.21}$$

From the obtained resultant SFL vector in the stationary reference frame consists of one vector rotating forward at synchronous speed as in the symmetric case, and a rotating vector on top of that, consisting of one part rotating synchronously forward and one backward.

The loci and radii pattern for above three case are shown in Figure 4.6. For each of the phases, the SFL magnitude is proportional to the respective locus' radius (*a,b,c*), and its inclination is proportional to the respective phase angle (*a,b,c*). As the three-phase are identical under symmetric conditions, the real and imaginary components for a given load are same and expressed as a circle in a complex plane. With the asymmetry on *phase c* due to change in the magnitude and the phase, the shape, size, and orientation of the loci points change vary from the signature loci; hence, Equation 4.21 is satisfied.

Next step is to transform the rotating vector into *dq* and anti *dq* reference frame.

An asymmetric SFL in rotor reference frame(dq) -

Using equation 4.22 as given below:

$$\overrightarrow{\psi_s}^{dq} = \overrightarrow{\psi_s} e^{-j(\theta_r)} \tag{4.22}$$

where θ_r,

$$\theta_r = \omega t; \tag{4.23}$$

Substituting above in equation 4.22 together with the obtained resulting vector in stationary reference frame the obtained rotating vector in *dq* is :

$$\overrightarrow{\psi_s}^{dq} = \begin{cases} \Delta\hat{\psi} = \Delta\delta = 0 \rightarrow \sqrt{\frac{3}{2}}\hat{\psi}e^{j(\delta)} \\ \Delta\hat{\psi} \neq 0; \Delta\delta = 0 \rightarrow \sqrt{\frac{3}{2}}\hat{\psi}e^{j(\delta)} + \sqrt{\frac{2}{3}}\Delta\hat{\psi}\frac{(e^{j(\delta)} + e^{-j(2\omega t+\delta-\gamma)})}{2} \\ \Delta\hat{\psi} \neq 0; \Delta\delta \neq 0 \rightarrow \sqrt{\frac{3}{2}}\hat{\psi}e^{j(\delta)} + \\ \sqrt{\frac{2}{3}}(\hat{\psi} - \Delta\hat{\psi})\frac{(e^{j(\delta+\Delta\delta)} + e^{-j(2\omega t+\delta+\Delta\delta-\gamma)})}{2} - \sqrt{\frac{2}{3}}\hat{\psi}\frac{e^{j(\delta)} + e^{-j(2\omega t+\delta-\gamma)}}{2} \end{cases} \tag{4.24}$$

From the obtained resultant SFL vector in the *dq* or rotor reference frame consists of constant point (shown in the middle Figure 4.6) in the symmetric case, and a backward rotating vector rotating at twice the speed of the symmetric vector under stationary reference frame in the asymmetric case shown in the middle Figure 4.6 with red and blue dot.(when the magnitude and phase of one of the phase different than the other phase).

An asymmetric SFL in anti synchronous reference frame(d-q-) -

The SFL in the ASRF can be expressed by a coordinate transformation according to equation 4.25. In this equation, θ_r is the same as given in equation 4.23, but rotating in the opposite direction.

Substituting same as above the resulting rotating vector in *d-q-* is :

$$\overrightarrow{\psi}_{d-q-} = \overrightarrow{\psi}_{\alpha\beta}.e^{j(\omega t)} \tag{4.25}$$

$$\overrightarrow{\psi}_s^{d-q-} = \begin{cases} \Delta\hat{\psi} = \Delta\delta = 0 \rightarrow \sqrt{\frac{3}{2}}\hat{\psi}e^{j(2\omega t+\delta)} \\ \Delta\hat{\psi} \neq 0; \Delta\delta = 0 \rightarrow \sqrt{\frac{3}{2}}\hat{\psi}e^{j(2\omega t+\delta)} - \sqrt{\frac{2}{3}}\Delta\hat{\psi}\frac{(e^{j(2\omega t+\delta)}+e^{-j(\delta-\gamma)}}{2} \\ \Delta\hat{\psi} \neq 0; \Delta\delta \neq 0 \rightarrow \sqrt{\frac{3}{2}}\hat{\psi}e^{j(2\omega t+\delta)} - \sqrt{\frac{2}{3}}\hat{\psi}\frac{(e^{j(2\omega t+\delta)}+e^{-j(\delta-\gamma)}}{2} + \\ \sqrt{\frac{2}{3}}(\hat{\psi}-\Delta\hat{\psi})\frac{(e^{j(2\omega t+\delta+\Delta\delta)}+e^{-j(\delta+\Delta\delta-\gamma)})}{2} \end{cases} \tag{4.26}$$

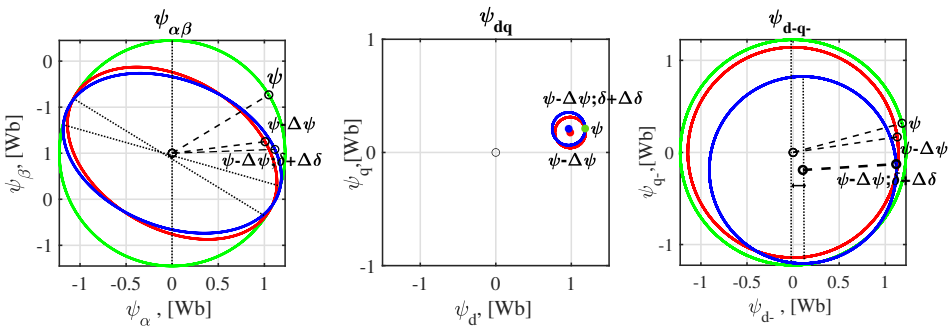

Figure 4.6: Change in the loci pattern at symmetric and asymmetrical conditions under $\alpha\beta$, *dq* and *d-q-*

During asymmetry, the obtained resultant vector in *d-q-* frame have both stationary (DC) and rotating components (AC). This is due to fact that the difference in phase voltages is a single phase component which on its own cannot be expressed as a rotating vector. Nevertheless, the phase quantities are transformed and their fundamentals will appear as a dc quantity in *d-q-* frame shown with double arrow black line in the rightmost Figure 4.6.

4.3.1 Case study

In the simulink, the steps for SFDO based diagnostics are initially simply implemented to get an understanding of symmetrical and asymmetrical three phase supply.

The model comprising of all the above mentioned steps (Figure 4.2- Figure 4.4) and fed by a three-phase sine wave voltage supply.

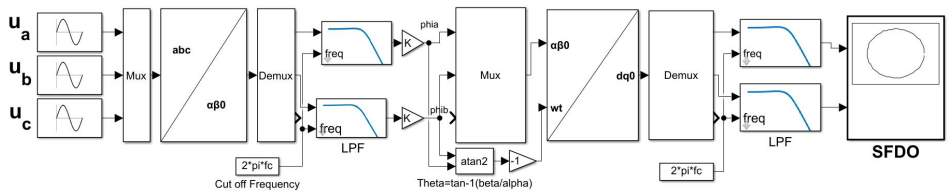

Figure 4.7: Evaluation of the proposed concept by using assymetric three phase supply in simulink

A script is used to run the model while varying the voltage supply across phases *a, b, and c.* A simulation with three levels of voltage deviation is made using the above model. Normal voltage is the peak voltage of 100 V, half normal voltage is the peak voltage of 50 V, and zero voltage is the extreme for checking the offset in extreme cases such as short circuit. This is applied in either phase of the three phases *(a, b, c)*. In an ideal case of sinusoidal balanced SFL, the space phasor model in the complex plane is in the form of a circle centered around the origin. To obtain the stator flux linkages under the stationary reference frame, the voltages are converted from three phase to two phase and low pass filtered with a gain equal to time constant.

Under perfectly symmetrical case, the SFL in α-β frame of reference is in the form of a circle centered around the origin. In the next step, the SFL is transformed from α-β to ASRF. Based on the Figure 4.8 (middle column), the flux lines appear to be twice as large as when compared to α-β frame of reference (following equation 4.26). As a result of the asymmetrical supply, the origin is shifted and isn't centered around origin.

DC offset (SFDO) obtained after passing ASRF signal to LPF is shown in the right column of Figure 4.8. It shows an unbalanced scenario in the form of a larger offset. The SFDO increases with an increase in supply voltage unbalance. For instance, the SFDO is maximum when one of the phase voltage is nil and zero when the applied phase voltages are equal or balanced.

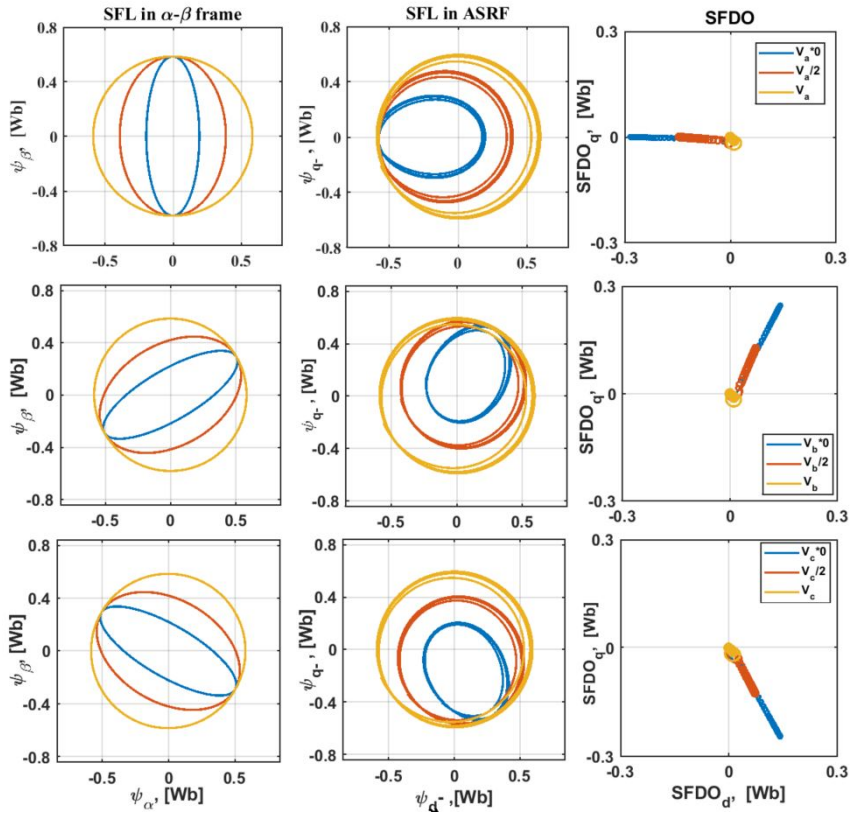

Figure 4.8: Simulation results of assymetrical voltages across x) phase *a* y) phase *b* z) phase *c*

Accordingly, this simple case study illustrates the effectiveness of the proposed method by depicting the SFDO value's magnitude and direction and their corresponding fault location based on unbalance or asymmetry.

4.4 Vector control with proposed diagnostic scheme

Implementation of the proposed model is made in a existing vector control system with a name of the SFDO observer.

The proposed SFDO observer is added to the inner loop of the FOC. A complete diagnostic model scheme is shown in Figure 4.9.

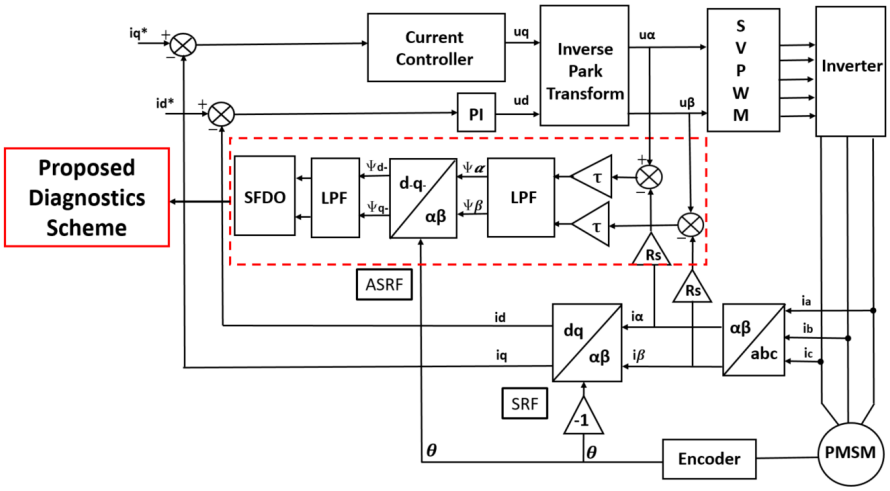

Figure 4.9: The block diagram of proposed scheme under FOC

4.5 Summary

This chapter presented the principal and methodology of the proposed stator flux linkage DC offset observer. Additionally, the synchronous and antisynchronous reference frames are illustrated and mathematically derived under symmetry and asymmetric cases. Using the proposed methodology, a simple case study of changing the supply voltage is presented to show its effectiveness. An improved FOC model is created with an inner loop of the proposed diagnostics.

4.6 Learning outcomes

This chapter leads the author to learn about anti synchronous reference frame. SFDO based diagnostic with unbalance voltage helped to understand the principle and the know how of its implementation and its applicability to ITF detection.

References

[1] [Online]. Available: https://www.iea.lth.se/kel/2020

[2] B. Zhang, Y. Pi, and Y. Luo, "Fractional order sliding-mode control based on parameters auto-tuning for velocity control of permanent magnet synchronous motor," *ISA Transactions*, vol. 51, no. 5, pp. 649–656, 2012. [Online]. Available: https://www.sciencedirect.com/science/article/pii/S0019057812000547

[3] B. Peterson, "Induction machine speed estimation - observations on observers," *TEIE-1009*, 1996. [Online]. Available: https://portal.research.lu.se/en/publications/induction-machine-speed-estimation-observations-on-observers

[4] C. J. e. a. O'Rourke, "A geometric interpretation of reference frames and transformations: dq0, clarke, and park," *IEEE Transactions on Energy Conversion 34, 4*, pp. 2070 – 2083, December 2019.

[5] S.M.A.cruz, "Stator winding fault diagnosis in three-phase synchronous and asynchronous motors, by the extended park's vector approach," *IEEE Transactions on Industry Applications*, Sept.-Oct. 2001.

Chapter 5

Inter turn fault analysis using analytical model

This chapter presents an analytical model of a permanent magnet synchronous machine with a stator ITF. The model of the healthy PMSM is initially described in order to set the basis of the model and define the symbols used. Later, PMSM faulted equations is described with the same nomenclature. A study of ITF's effect on back emf, inductance, resistances, stator flux linkages, current and torque is conducted to make the equations more intuitive. Additionally, a description of how these parameters vary under current control with and without ITF is provided with a simulink based model. The following steps discuss the detailed effect of ITF on fault current and electromagnetic torque under various fault scenarios. Afterwards, a model has been improvised with position dependent inductance values and induced voltages are exported from the FEM study and the results are further analyzed and discussed.

5.1 Analytical model of PMSM-without ITF

This section presents an analytical three-phase model of the PMSM similar to the models described in[1, 5]and [2, 5]. The modelling is preferably conducted in three phase to understand how the ITF affects the flux, inductance, voltage and current across the phases. For the clarity of the text, in this thesis a "linear machine" refers to a machine where the properties of materials are assumed to be linear.

Stator flux linkages and voltage equations -

Permanent magnet synchronous machines consist of a stator with a three phase winding, and a rotor with permanent magnets. The terminals of the stator can be connected to a three phase voltage source supply or through a three phase voltage source inverter (VSI). A magnetic field is created in the air gap of the machine both by the stator current and the permanent magnets. Therefore the flux linkage is a sum of the flux linkages from the stator phase current and from the permanent magnets[3, 5].

$$\psi_j(t) = L_{ij}(t).i_j(t) + \psi_{pm}(t) \tag{5.1}$$

Therein, the matrix $L_{ij}(t)$ (3x3) is referred to as self and mutual inductance and ψ_{pm} (1 x 3) denotes flux linkage in phases *(a, b and c)* from the permanent magnets of the rotor and it serves as a constant.

The phase flux linkages can be written as :

$$\psi_a = L_{aa}i_a + L_{ab}i_b + L_{ac}i_c + \psi_{pm}sin(\theta_r) \tag{5.2}$$

$$\psi_b = L_{bb}i_b + L_{ba}i_b + L_{bc}i_c + \psi_{pm}sin(\theta_r - \frac{2\pi}{3}) \tag{5.3}$$

$$\psi_c = L_{cc}i_c + L_{cb}i_b + L_{ca}i_c + \psi_{pm}sin(\theta_r + \frac{2\pi}{3}) \tag{5.4}$$

where:

- ψ_a, ψ_b, ψ_c represents the total fluxes linking each stator winding.
- L_{aa}, L_{bb}, L_{cc} represents the self-inductances of the stator windings.
- L_{ab}, L_{ac}, L_{bc} represents the mutual-inductances of the stator windings.
- ψ_{pm} represents the permanent magnet flux linkage.
- θ_r represents the rotor electrical angles.

According to Faraday's law, a voltage is induced across phases based on the rate of change of magnetic flux linkage. The phase voltage of a wye-connected electrical machine can electrically be modeled as[3, 5]:

$$u_j(t) = R_j i_j(t) + \frac{\mathrm{d}\psi_j(t)}{\mathrm{d}t} \tag{5.5}$$

Therein $u_j(t)$ denotes the three phase voltage, R_j is the stator winding resistance across each phase, i_j is the three phase current and ψ_j is the flux linkage of three phase $j\epsilon$ *a,b,c.* The time is denoted by t.

Substituting values obtained from flux linkages(eq.5.2 - eq.5.4) to eq.5.5 will provide the stator terminal voltages across each phases -

$$u_a = R_a i_a + L_{aa}\frac{\mathrm{d}i_a}{\mathrm{d}t} + L_{ab}\frac{\mathrm{d}i_b}{\mathrm{d}t} + L_{ac}\frac{\mathrm{d}i_c}{\mathrm{d}t} + \psi_{pm}\omega_e cos(\theta_r) \tag{5.6}$$

$$u_b = R_b i_b + L_{ba}\frac{\mathrm{d}i_a}{\mathrm{d}t} + L_{bb}\frac{\mathrm{d}i_a}{\mathrm{d}t} + L_{bc}\frac{\mathrm{d}i_c}{\mathrm{d}t} + \psi_{pm}\omega_e cos(\theta_r - \frac{2\pi}{3}) \tag{5.7}$$

$$u_c = R_c i_c + L_{ac}\frac{\mathrm{d}i_a}{\mathrm{d}t} + L_{cb}\frac{\mathrm{d}i_b}{\mathrm{d}t} + L_{cc}\frac{\mathrm{d}i_c}{\mathrm{d}t} + \psi_{pm}\omega_e cos(\theta_r + \frac{2\pi}{3}) \tag{5.8}$$

where ω_e is the time derivative of the electrical position of the rotor. Rotating magnetic flux linkages from magnets are represented by back emf $e_j(t)$ with phase *b* and phase *c* will be $\frac{2\pi}{3}$, and $\frac{-2\pi}{3}$, electrical radians shifted with respected to phase a, respectively. Matrix representation of $e_j(t)$ is provided in eq.5.13.

Matrix based equations of a PMSM

Assume that stator phases are identically constructed (except being phase shifted) the phases have identical phase resistances, self inductance's, and inductive couplings:

$$R_a = R_b = R_c = R_s, L_{ab} = L_{ac} = L_{bc} = M, L_{aa} = L_{bb} = L_{cc} = L \tag{5.9}$$

The sum of the three-phase currents for a star-connected balanced machine equals to zero.

$$i_a + i_b + i_c = 0 \tag{5.10}$$

Combining equations from equation 5.6-5.8, the voltage equation and the stator flux linkage equations of balanced three-phase machine can be represented in matrix form as and given by equation 5.11 and 5.12 respectively.

$$\begin{bmatrix} u_a \\ u_b \\ u_c \end{bmatrix} = \begin{bmatrix} R_s & 0 & 0 \\ 0 & R_s & 0 \\ 0 & 0 & R_s \end{bmatrix} \begin{bmatrix} i_a \\ i_b \\ i_c \end{bmatrix} + \begin{bmatrix} L & M & M \\ M & L & M \\ M & M & L \end{bmatrix} \frac{d}{dt} \begin{bmatrix} i_a \\ i_b \\ i_c \end{bmatrix} + \begin{bmatrix} e_a \\ e_b \\ e_c \end{bmatrix} \tag{5.11}$$

$$\begin{bmatrix} \psi_a \\ \psi_b \\ \psi_c \end{bmatrix} = \begin{bmatrix} L & M & M \\ M & L & M \\ M & M & L \end{bmatrix} \begin{bmatrix} i_a \\ i_b \\ i_c \end{bmatrix} + \psi_{pm} \begin{bmatrix} sin(\theta_r) \\ sin(\theta_r - \frac{2\pi}{3}) \\ sin(\theta_r + \frac{2\pi}{3}) \end{bmatrix} \tag{5.12}$$

where,

$$\begin{bmatrix} e_a \\ e_b \\ e_c \end{bmatrix} = \omega_e \psi_{pm} \begin{bmatrix} cos(\theta_r) \\ cos(\theta_r - \frac{2\pi}{3}) \\ cos(\theta_r + \frac{2\pi}{3}) \end{bmatrix} \tag{5.13}$$

Torque equations

Electromagnetic torque equation can be obtained from the analytical model and its electrical representation of the machine's mechanical power, which can be obtained by the product of the currents and the back-emf [4, 5].

$$P = e_a i_a + e_b i_b + e_c i_c \tag{5.14}$$

Using eq.5.14 and the machine's mechanical speed, instantaneous machine torque can be determined, whose accuracy is largely determined by the accuracy of the back-emf representation.

$$T_m \omega_m = e_a i_a + e_b i_b + e_c i_c \tag{5.15}$$

5.2 Analytical model of PMSM with ITF

Three phase circuit of PMSM with ITF

The circuit model of PMSM with stator ITF is shown in Figure 5.1. The modelled machine [4, 5] is a three phases, three pole pairs, interior permanent magnet machine with concentrated windings (CW) and nine teeth. Each tooth has a single coil

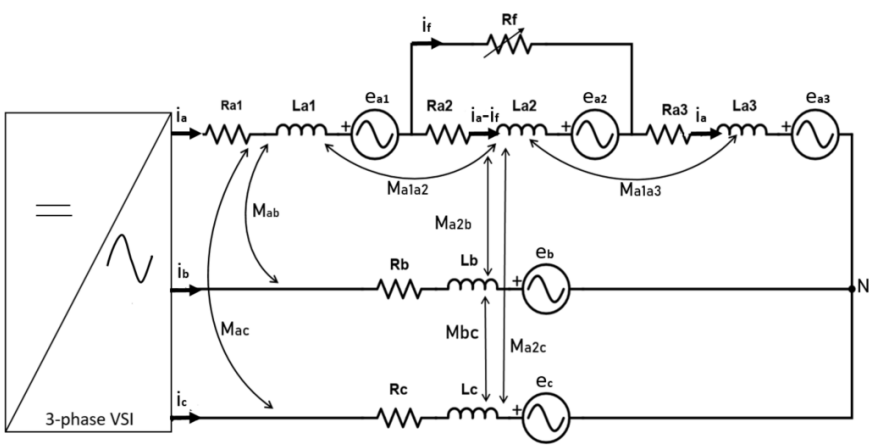

Figure 5.1: PMSM with stator turn-turn fault

wounded around it, which consists of 48 turns. One phase consists of three series connected coils, leading to a total of 144 turns per phase. The faulty phase in Figure 5.1 is phase *a* but it could be possible to move it to other phases as well. All

phases have identical coupling between two phases and have equal self-inductance due to symmetry denoted by L and M. By connecting a resistor across any coil/phase, a faulty operation due to inter-turn fault is created for analysis. The middle winding is considered here for short circuit creation and is represented by a winding with resistance R_{a2}, inductance L_{a2} and back emf e_{a2}. The variable resistor R_f represents the inter-turn fault resistance, which is very high during normal operation of PMSM and converge to zero when a single winding short fault occurs, thus producing a high current flow.

As a measure of the percentage of faulted turns in the winding, μ is used to characterize the stator inter-turn fault. It is defined as the ratio between the number of short-circuited turns(N_2) and the total number of turns(N_a) in the faulted phase.

$$\mu = \frac{N_2}{N_a}; \tag{5.16}$$

The resistance increases directly with the number of turns when the conductor length increases, assuming that the conductor section and resistivity are constant. Thus, the phase's resistance R_s can be divided into R_{a1} and R_{a2}. The partial resistances are given as

$$R_{a1} = (1-\mu)R_s; R_{a2} = (\mu)R_s \tag{5.17}$$

where R_{a1} is the resistance of healthy part, and R_{a2} is the resistance of the faulty part.

Inductance values of faulted PMSM

The most widely used method for calculating self and mutual inductances under fault is proportional to the square of the number of turns, as documented in literature [5]. With N_s number of turns in a phase, the healthy and faulty coils have (1–μ)N_s and μN_s number of turns respectively. So, the self and mutual inductances of healthy and faulty coils are given as

$$L_{a1} = (\mu)^2 L, L_{a2} = (1-\mu)^2 L, M_{a2a1} = \mu(1-\mu)L, M_{a2b} = (1-\mu)M \tag{5.18}$$

The terms L_{a1} and L_{a2} represent the self-inductances of the healthy and faulty sub-coils, respectively. The terms M_{a1a2} and M_{a2a3} represent the mutual inductances between the healthy and the faulty parts of the coils. While M_{a2b} and M_{a2c} represent the mutual inductances between the faulty coil and the healthy phase b and c respectively.

To determine inductance under fault conditions by the equation given above, a fault fraction is required, and in this case, the fault resistance is varied, not the related number of turns. The inductance of the faulty coil are directly linked to the ratio between the number of shorted turns and the number of total turns of one phase [5,

5] also known as fault fraction. Considering that one coil has an R_f load, the fault fraction in this case is 0.33. By substituting mu, the faulted inductances are obtained using eq. 5.34.

Table 5.1: Faulted inductances obtained from analytical expression [mH]

Fault Condition	L_{a2}	M_f	M_{a2b}	M_{a2c}
μ= 0.33	12.8	6.5	-4.62	-4.62

This assumption is exact in the case of windings with one slot per pole and per phase and supposing one pole pair machines. However, it is not valid in the case of windings with more than one slot per pole and per phase[5, 5]. **Due to winding placement and influence of machine geometry under fault in this work identification of inductance is based on finite element analysis for various fault configurations and is further described in detail in chapter** 6**.**

5.2.1 Voltage equation of faulted PMSM

In the event of an ITF in any phase of a PMSM, the affected phase changes from a healthy state into a faulted state, as indicated in Figure 5.2. The fault creation is made by connecting a fault resistor (R_f) across the coils. The machine used in this case is having three coils per phase. When considering the phase winding, it can be modeled as three series-connected coils, comprising the fault loop and the remaining winding turns. Denoting with u_a the voltage across the non-faulted phase, u_{a1}, u_{a2} and u_{a3} are the resulting induced voltages over the three coils.

Assuming linear properties, the equations describing the faulted machine can be written as follows:

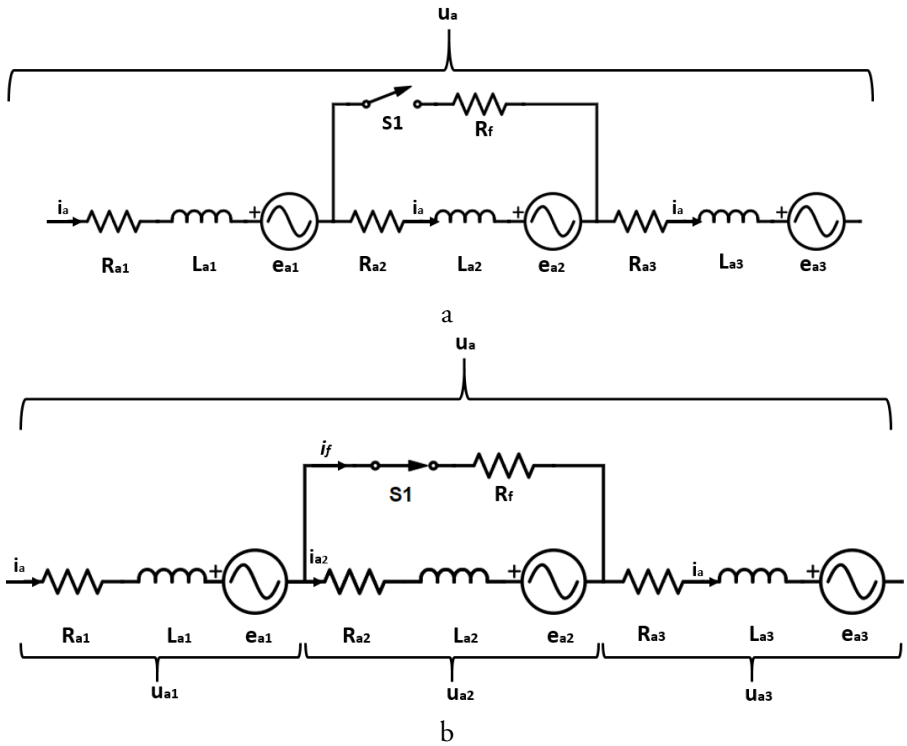

Figure 5.2: The single phase representation of a phase a with switch open is illustrated in figure a, and figure b presents the single phase representation of the phase *a* in the case of a turn-to-turn fault

$$u_{a1} = R_{a1}.i_a + L_{a1}\frac{\mathrm{d}i_a}{\mathrm{d}t} + M_{a2a1}\frac{\mathrm{d}(i_a - i_f)}{\mathrm{d}t} + M_{a3a1}\frac{\mathrm{d}i_a}{\mathrm{d}t} + M_{a1b}\frac{\mathrm{d}i_b}{\mathrm{d}t} + M_{a1c}\frac{\mathrm{d}i_c}{\mathrm{d}t} + e_{a1} \tag{5.19}$$

$$u_{a2} = R_{a2}.(i_a - i_f) + L_{a2}\frac{\mathrm{d}(i_a - i_f)}{\mathrm{d}t} + (M_{a1a2} + M_{a3a2})\frac{\mathrm{d}i_a}{\mathrm{d}t} + M_{a2b}\frac{\mathrm{d}i_b}{\mathrm{d}t} + M_{a2c}\frac{\mathrm{d}i_c}{\mathrm{d}t} + e_{a2} \tag{5.20}$$

$$u_{a3} = R_{a3}.i_a + L_{a3}\frac{\mathrm{d}i_a}{\mathrm{d}t} + M_{a2a3}\frac{\mathrm{d}(i_a - i_f)}{\mathrm{d}t} + M_{a1a3}\frac{\mathrm{d}i_a}{\mathrm{d}t} + M_{a3b}\frac{\mathrm{d}i_b}{\mathrm{d}t} + M_{a3c}\frac{\mathrm{d}i_c}{\mathrm{d}t} + e_{a3} \tag{5.21}$$

where R_{ai} is the resistance (with i = $1, 2, 3$ in reference to Figure 5.2 b), L_{ai} is the self inductance, e_{ai} is the back-emf and M_{aiaj} is the mutual inductance (where i denotes the coil number $1, 2, 3$) and i_{a2} is equal to $i_a - i_f$. The term R_f represents the contact resistance between the short circuited turns.

By adding equation 5.19-5.21, we get the total voltage drop across phase a:

$$u_a = R_a i_a + L_a \frac{\mathrm{d}i_a}{\mathrm{d}t} - (M_{a2a1} + L_{a2} + M_{a2a3}) \frac{\mathrm{d}i_f}{\mathrm{d}t} + M_{ab} \frac{\mathrm{d}i_b}{\mathrm{d}t} + M_{ac} \frac{\mathrm{d}i_c}{\mathrm{d}t} + e_a - R_{a2} i_f \tag{5.22}$$

Where, $u_a = u_{a1} + u_{a2} + u_{a3}$; $R_a = R_{a1} + R_{a2} + R_{a3}$; The self-inductance L_a of three parts and their mutual couplings are:

$$L_a = L_{a1} + L_{a2} + L_{a3} + M_{a1a2} + M_{a2a3} + M_{a3a1} \tag{5.23}$$

Based on linear material for the machine, the mutual couplings are as follows of the phase from faulted phase to the healthy phase is equal to the coupling from the three coils in Figure 5.2 b to the other phases, i.e.

$$M_{ab} = M_{a1b} + M_{a2b} + M_{a3b}; M_{ac} = M_{a1c} + M_{a2c} + M_{a3c} \tag{5.24}$$

Inductance of the faulty coil determined by the sum of its self-inductance's L_{a2} and the mutual couplings from the other healthy coil.

$$M_f = M_{a2a1} + L_{a2} + M_{a2a3}; e_{a2} = e_f \tag{5.25}$$

The voltage across the new short-circuit loop created by the turn-to-turn fault can be described as

$$0 = R_{a2} i_a + M_f \frac{\mathrm{d}i_a}{\mathrm{d}t} - L_{a2} \frac{\mathrm{d}i_f}{\mathrm{d}t} - (R_{a2} + R_f).i_f + e_{a2} + M_{a2b} \frac{\mathrm{d}i_b}{\mathrm{d}t} + M_{a2c} \frac{\mathrm{d}i_c}{\mathrm{d}t} \tag{5.26}$$

The voltage across the phase b and c can be described as

$$u_b = R_b i_b + L_b \frac{\mathrm{d}i_b}{\mathrm{d}t} + M_{ab} \frac{\mathrm{d}i_a}{\mathrm{d}t} - M_{a2b} \frac{\mathrm{d}i_f}{\mathrm{d}t} + e_b \tag{5.27}$$

$$u_c = R_c i_c + L_c \frac{\mathrm{d}i_c}{\mathrm{d}t} + M_{ac} \frac{\mathrm{d}i_a}{\mathrm{d}t} - M_{a2c} \frac{\mathrm{d}i_f}{\mathrm{d}t} + e_c \tag{5.28}$$

By considering machine symmetry, the following assumptions are made to simplify the equation.

$$R_a = R_b = R_c = R_s \tag{5.29}$$

$$L_a = L_b = L_c = L \tag{5.30}$$

$$M_{ab} = M_{ac} = M_{bc} = M \tag{5.31}$$

The generic three phase faulted PMSM can be described in matrix form :

$$\begin{bmatrix} u_a \\ u_b \\ u_c \\ 0 \end{bmatrix} = \begin{bmatrix} R_s & 0 & 0 & -\mu.R_s \\ 0 & R_s & 0 & 0 \\ 0 & 0 & R_s & 0 \\ -\mu.R_s & 0 & 0 & \mu.R_s + R_f \end{bmatrix} \begin{bmatrix} i_a \\ i_b \\ i_c \\ i_f \end{bmatrix} + \begin{bmatrix} L & M & M & -M_f \\ M & L & M & -M_{a2b} \\ M & M & L & -M_{a2c} \\ -M_f & -M_{a2b} & -M_{a2c} & L_{a2} \end{bmatrix} \frac{d}{dt} \begin{bmatrix} i_a \\ i_b \\ i_c \\ i_f \end{bmatrix} + \begin{bmatrix} e_a \\ e_b \\ e_c \\ -e_f \end{bmatrix} \tag{5.32}$$

where, u_a, u_b, and u_c are phase voltages. i_j are three phase current (with *j = a, b, c and* f). The negative sign of e_f is due to the selected direction of the fault current i_f being opposite to i_a.

where,

$$\begin{bmatrix} e_a \\ e_b \\ e_c \\ e_f \end{bmatrix} = \omega_e \Psi_m \begin{bmatrix} cos(\theta_r) \\ cos(\theta_r - \frac{2\pi}{3}) \\ cos(\theta_r + \frac{2\pi}{3}) \\ -(\mu)cos(\theta_r) \end{bmatrix} \tag{5.33}$$

5.2.2 Specifications of the test machines used for modeling

The test machine used for modelling has a continuous power rating of 4 kW designed to be operated with a DC-link voltage of 300 V. It has a base and a top speed of 750 rpm and 3000 rpm, respectively, and a rated and a peak torque of 12.7 Nm and 50.9 Nm, respectively. The parameters of machine used in simulation are shown in Table 5.2.

Table 5.2: PMSM MACHINE PARAMETERS [4, 5]

Rated Power (kW)	4	Ld (mH)	22
Rated Current (A)	15	Lq (mH)	34
Rated Speed (rpm)	750	Rs (Ω)	0.78
ψ_{pm}(Wb)	0.48	number of turns per coil	48
number of phases	3	number of pole pairs	3
number of slots/pole/phase	1	number of parallel paths	1

Parameters settings while solving ordinary differential equations (ODEs):

The machine is freewheeling at synchronous speed (speed and supply electrical frequency are 500 rpm and 25 Hz respectively). The stator resistance and *d-q* axis in-

ductances are provided in Table 5.2.

During the simulation average value of self and mutual inductances are used. The simulation type is continuous, the simulation step time is $1.2e^{-3}s$, and the simulation solver is ode45. The simulation is carried out with DC-link voltage (Udc) equal to the back emf of the machine at 500rpm i.e.70V. So as to run the machine in the idling mode.

The real time rotor position is calculated by the equation below where the load torque is zero and the electromagnetic torque is obtained by the equation 5.34.

$$T_e - T_L = J.\frac{d\omega_m}{dt} + B_m.\omega_m \tag{5.34}$$

where J is the total moment of inertia of the machine including the motor itself and mechanical load. ω_m is the mechanical rotor speed, T_e is the electrical driving torque, T_L is the load torque, B_m is the viscous friction coefficient. For solving ODEs (eq. 5.32), all the mechanical and electrical parameters are tabulated for reference.

Table 5.3: Parameters of inter-turn fault for PMSM

Permanent magnet flux linkage (ψ_{pm})	0.5 Wb
Moment of inertia (J)	0.475 kg.m2
Machine Speed (ω_m)	500 rpm
Viscous friction factor(B_m)	18 Nm/rpm
Phase Inductance (L)	28 mH
Mutual Inductances(M)	-14 mH
Inter-turn short circuit resistance (R_f)	$5, 2.5, 1\ \Omega$
Load torque (T_L)	0 Nm

5.3 Simulation results

Stator flux linkages

The stator flux linkages due to the stator phase currents and from the permanent magnets of faulted PMSM can be derived from equation 5.1 as

$$\begin{aligned}
\psi_a &= Li_a + Mi_b + Mi_c - (M_{a2a1} + L_{a2} + M_{a2a3})i_f + \psi_m sin(\theta_r) \\
\psi_b &= Li_b + Mi_a + Mi_c - (M_{a1b} + M_{a2b} + M_{a3b})i_f + \psi_m sin(\theta_r - \frac{2\pi}{3}) \\
\psi_c &= Li_c + Mi_a + Mi_b - (M_{a1c} + M_{a2c} + M_{a3c})i_f + \psi_m sin(\theta_r + \frac{2\pi}{3})
\end{aligned} \tag{5.35}$$

In the case of a turn-to-turn fault, a short-circuit loop is created, and the SFL across it is as follows:

$$\psi_f = L_{a2} i_f - (M_{a2a1} + L_{a2} + M_{a2a3}) i_a - M_{a2b} i_b - M_{a2c} i_c - \mu \psi_m sin(\theta_r) \quad (5.36)$$

There is a negative sign on the mutual couplings because the selected direction for i_f is opposite to i_a.

The stator flux linkages equation of three phase faulted PMSM can be written in the matrix form as

$$\begin{bmatrix} \psi_a \\ \psi_b \\ \psi_c \\ \psi_f \end{bmatrix} = \begin{bmatrix} L & M & M & -M_f \\ M & L & M & -M_{a2b} \\ M & M & L & -M_{a2c} \\ -M_f & -M_{a2b} & -M_{a2c} & L_{a2} \end{bmatrix} \begin{bmatrix} i_a \\ i_b \\ i_c \\ i_f \end{bmatrix} + \psi_m \begin{bmatrix} sin(\theta_r) \\ sin(\theta_r - \frac{2\pi}{3}) \\ sin(\theta_r + \frac{2\pi}{3}) \\ -(\mu) sin(\theta_r) \end{bmatrix} \quad (5.37)$$

By subsituting the inductances and by using the dynamic fault equation for stator flux linkage provided in equation 5.37, the SFL across each phase can be obtained.

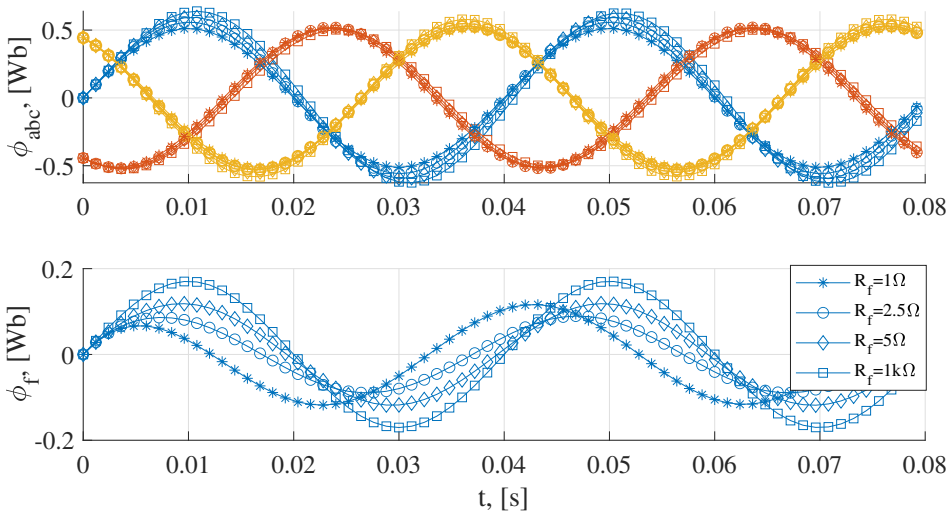

Figure 5.3: SFL per phase and SFL across faulty coil simulated by the equation system with R_f= 1, 2.5 ,5 and 1kΩ

The obtained results from simulations are presented in Figure 5.3. The machine is freewheeling, so there is only SFL due to permanent magnets. Across the faulted phase, the SFL decreases as the main SFL and the SFL generated by the fault current act in opposite directions. Despite this, the magnitude of flux when fault resistance is1 Ω is higher than when fault resistance is 2.5 Ω. This could be due to the increased mutual coupling or it could be due to the increased phase difference compared to healthy SFL.

Fault current

Using matrix eq. 5.32, the fault current (i_f) obtained for different values of the fault resistance: R_f=1, 2.5, 5 and 1kΩ.

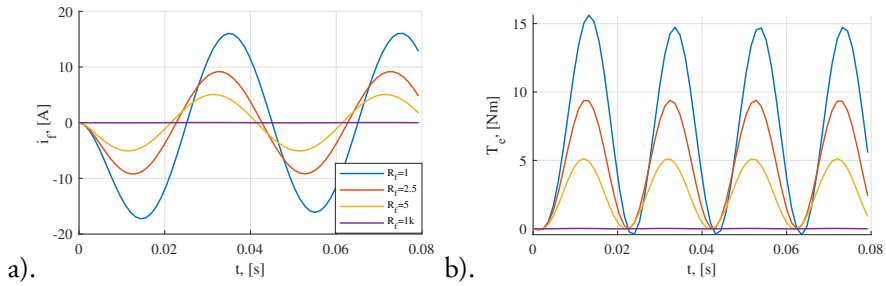

Figure 5.4: Fault current and electromagnetic torque simulated by the equation system with R_f= 1, 2.5,5 and 1kΩ

In Table 5.4, the peak values for i_f under different cases is listed.

Table 5.4: ITF's effect on fault current i_f

Parameter	R_f=1kΩ	R_f=5Ω	R_f=2.5Ω	R_f=1Ω
$i_f[A]$	0.02	4.45	8	14.28
$phase-lag, [deg]$	–	10.8	21.6	43

As can be seen in the above table and from the Figure 5.4, both the magnitude and phase of the fault current increases with decrease in R_f, which results in higher resistive losses, resulting in localized heat. As a result of the extra heat, there may be further winding failures or faults of other types.

Electromagnetic Torque under ITF

The ITF introduces an additional impedance in the affected turn, causing a disturbance in the magnetic field. This disturbance leads to an uneven distribution of magnetic flux and, consequently, a torque ripple. In case of an ITF, the electrical model representation of the machine's mechanical power needs to be updated to include impact of the fault. Here is the updated power equation[4, 5]:

$$P_e = e_a i_a + e_b i_b + e_c i_c - e_f i_f \tag{5.38}$$

$$T_{el}\omega = e_a i_a + e_b i_b + e_c i_c - e_f i_f \tag{5.39}$$

Using eq.5.39, the ITF's impact on torque can be evaluated. As the fault current is the only current flowing in the circuit, the average torque is zero when the R_f is

very high. Figure 5.4, illustrates torque ripple caused by the extra term $e_f i_f$, since both the induced voltage e_f and the fault current i_f have the same frequency; thus, the presence of an ITF causes a torque component to oscillate twice the fundamental frequency.

The ITF's impact on the torque can be evaluated using the torque ripple factor. The torque ripple factor (TRF) is defined as the percentage of the difference between the maximum torque T_{max} and the minimum torque T_{min} compared to the average torque T_{avg}:

$$TRF = \frac{T_{max} - T_{min}}{T_{avg}} * 100 \tag{5.40}$$

The obtained results of TRF from simulations are tabulated below:

Table 5.5: ITF's effect on the torque ripple factor (TRF)

Parameter	R_f=5Ω	R_f=2.5Ω	R_f=1Ω
$T_{max}, [Nm]$	4	7.4	13.14
$T_{min}, [Nm]$	−0.015	−0.016	−0.69
$T_{avg}, [Nm]$	2	3.65	5.94
$TRF(\%)$	200	203	233

The ripple component introduced by the ITF has a larger amplitude compared the components which are also present for the healthy machine. The ripple component introduced by the fault may cause additional stress to the machine as well as the mechanical system to which the machine is connected.

5.4 Model initialisation

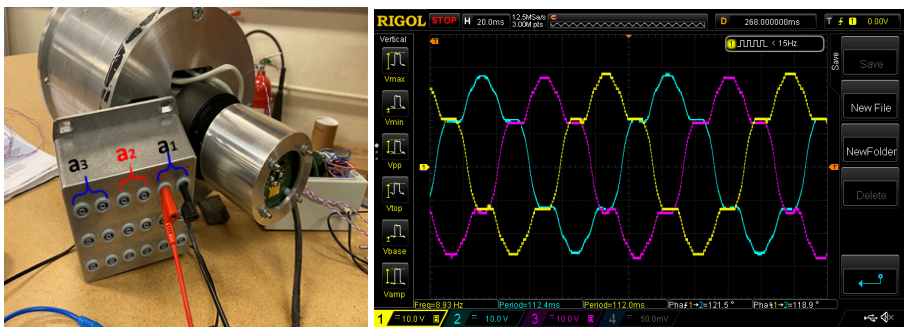

Figure 5.5: Test machine and measured induced voltage under no load condition

Without ITF - For initializing the analytical equation (AE) effectiveness, a lab study has been conducted both under healthy and faulted conditions. An easy setup is used for the test machine. A drilling machine rotates the machine at roughly 107rpm. The induced voltage and fault current was measured with an oscilloscope under healthy and faulted conditions. In Figure 5.5, the test machine and its measurement of induced voltage are shown.

The experimental and analytical results of the induced voltage are compared using AE from equation 5.32. As a result of the obtained comparison, harmonics should be included in the analytical equation based on the experimental results. In order to determine the exact harmonic content of the induced voltage waveform, a Fourier analysis is performed on the measured results. The result of the Fourier analysis is then implemented in the analytical model of the healthy machine. The induced voltage vector of the analytical model, including harmonics, is now calculated as follows:

$$e_{abc} = \omega_e \Psi_m \begin{bmatrix} \sum_{n=1}^{\infty} sin(A_{H,n}\theta_r + \phi_{a,n}) \\ \sum_{n=1}^{\infty} sin(A_{H,n}\theta_r + \phi_{b,n} - n\frac{2\pi}{3}) \\ \sum_{n=1}^{\infty} sin(A_{H,n}\theta_r + \phi_{c,n} + n\frac{2\pi}{3}) \end{bmatrix} \tag{5.41}$$

where, $A_{H,n}$ is the relative amplitude of the nth harmonic and $\phi_{j,n}$ is the phase shift of nth harmonic. Using substitution, the harmonic component of induced voltage from measured results across *phase a* is plotted along with the experimental result in Figure 5.6.

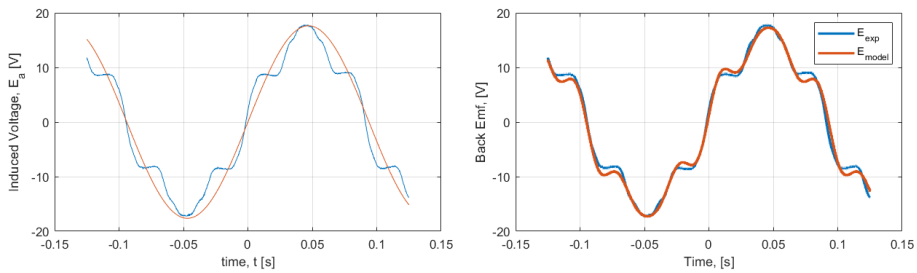

Figure 5.6: Comparison of the induced voltage obtained from the experiment and from the equations(without harmonics) 5.33 and eq(with harmonics). 5.41

With ITF

The current waveform is generated based on the induced voltage waveform described above. Inductance values are constant values derived from a FEM analysis. There is an induced voltage across the phases and the faulty coil has an induced voltage μ times what the actual phase voltage is. The obtained fault current shows a discrepancy in

phase when compared with the actual current. Therefore, an initial test is conducted with measured induced voltage across each coil and it is shown in Figure 5.7. From the result, the induced voltage across the coil decreases with decrease in R_f also a increase in phase difference can be seen with a decrease in R_f.

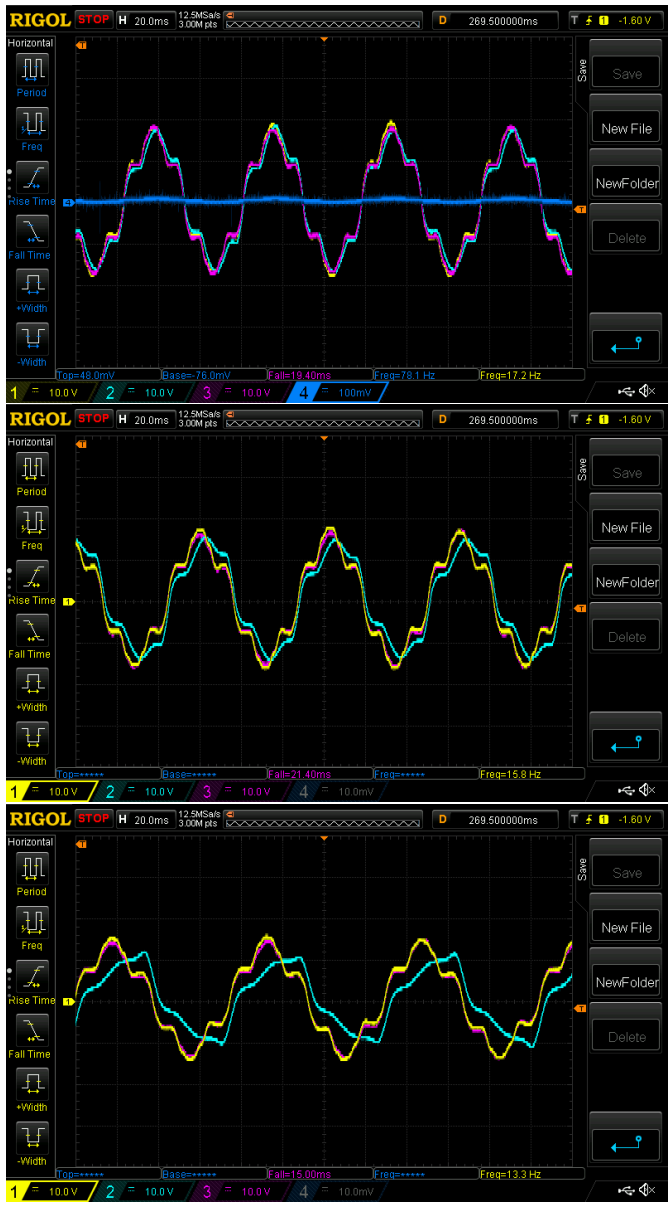

Figure 5.7: Measured induced voltage across one coil of phase a when R_f is 10,5 and 1.2 ohm respectively

To include the phase difference in the induced voltage under faulted conditions can be fitted using the following modified equation with phase difference:

$$e_{abcf} = \omega_e \Psi_m \sum_{n=1}^{\infty} \begin{bmatrix} sin(A_{H,n}\theta_r + \phi_{a,n}) \\ sin(A_{H,n}\theta_r + \phi_{b,n} - n\frac{2\pi}{3}) \\ sin(A_{H,n}\theta_r + \phi_{c,n} + n\frac{2\pi}{3}) \\ -(\mu)sin((A_{H,n}\theta_r + \phi_{a,n}) + \phi_{f,n}) \end{bmatrix} \tag{5.42}$$

where, $A_{H,n}$ is the relative amplitude of the nth harmonic and $\phi_{a,n}$ is the phase shift of nth harmonic and $\phi_{f,n}$ is the phase shift between the induced voltage in the short circuited turn and *phase a*. Taking the harmonic component and substituting it into the induced voltage of equation equation 5.42, the fault current can be obtained.

The measured fault current is compared to the fault current obtained from the analytical model. The fault current from the analytical equation is 6.1 A and measured fault current from test machine is 6.9 A. AE and experimental results appear to be in 13% disagreement in case of fault current.

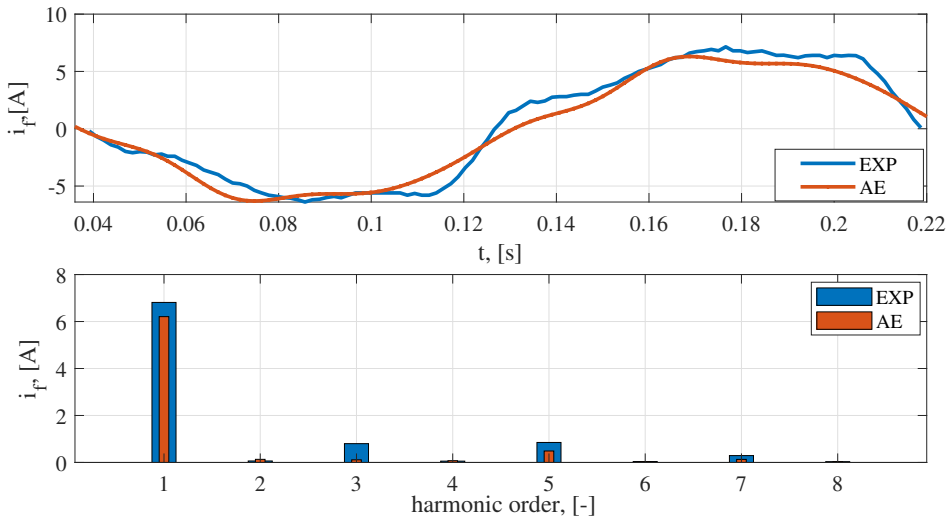

Figure 5.8: Comparison of fault current based on lab measurements and AE

5.5 Simulink model with current controller- without ITF

The fault model described and initialised above is used in conjunction with field-oriented control to observe the machine behaviour with and without ITF. A description of the entire model is provided in this section.

5.5.1 Simulink model

The simulink model used in this thesis for fault modeling and fault detection is provided in Figure 5.9. It have mainly four major components in the model: a current controller, a modulator, a three-phase inverter and the PMSM model (Healthy and Unhealthy). This chapter primarily aims to describe fault modeling by describing and analyzing the above four blocks, while chapter 7 describes the detection system block namely SFDO.

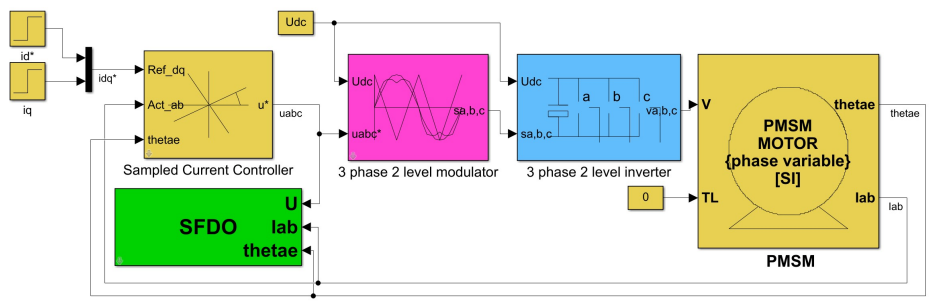

Figure 5.9: A simulink model used for studying the behaviour of PMSM under current control

A brief introduction of the different blocks is provided in order to build an understanding of the complete simulink model.

Sampled current control-

The simulink model uses PI (proportional integral) current controllers for their steady-state accuracy and robustness. The PI controller adjusts the motor current based on the error between the desired current and the measured current. The controller receives the reference current command and compares it with the measured current from

the machine model. Based on this error, the controller generates the appropriate voltage command to the inverter, which then adjusts the motor current accordingly. The controller parameters, such as gains and time constants, need to be carefully tuned to achieve the desired performance.

The current controller is the dead beat controller i.e. the entire current error can be eliminated in one sampling interval. To eliminate the error between the reference and the actual current voltage is provided at *d-q* reference frame as provided in equation below.

$$u_d(k) = \left(\frac{L_d}{T_s} + \frac{R_s}{2}\right)\left((i_d^*(k) - i_d(k)) + \frac{T_s}{(\frac{L_d}{R_s} + \frac{T_s}{2})} \cdot \sum_{n=k-1}^{n=0} (i_d^*(k) - i_d(k))\right) - \omega_e L_q i_q(k)$$

$$u_q(k) = \left(\frac{L_q}{T_s} + \frac{R_s}{2}\right)\left((i_q^*(k) - i_q(k)) + \frac{T_s}{(\frac{L_q}{R_s} + \frac{T_s}{2})} \cdot \sum_{n=k-1}^{n=0} (i_q^*(n) - i_q(n))\right) + \omega_e(\psi_m + L_d i_d(k)$$

where L_d, L_q, i_d and i_q are inductances and current at *d and q* axes and R_s is the stator resistance. T_s is the sampling time, ω_e is the machine electrical speed and k is the sampling instant.

Modulation- The voltage generated from the current controller is fed to the modulator for generating switching sequences for the power inverter. This modulation block employs symmetrized sinusoidal modulation with fixed carrier wave frequency. By subtracting the average of the maximum and minimum values of the reference sinusoidal voltage, symmetrized modulation is performed. A symmetrized sinusoidal signal is used as the modulation signal, while a triangular wave is used as the carrier signal. Using carrier waves to compare three-phase sinusoidal reference voltages, the logical signals S_a, S_b, S_c can be produced. Power transistor switching instants can be defined using the logical signal. Based on the given logical signals, power switches are turned on and off to produce voltage pulses.

Three phase inverter - Three phase inverter with modulation of the phase potential in two levels ($\pm\frac{U_{dc}}{2}$) the switches can be combined in eight patterns. Switching states S_a, S_b, S_c determine the status of switches in each leg. To every combination a set of phase voltages is related.

The PMSM model- The analytical model of PMSM is based on three phases equations. The matrix equations have already been explained in this chapter (equation 5.32). The mechanical system is based on torque equation 5.34, using it mechanical speed and rotation angle can be obtained.

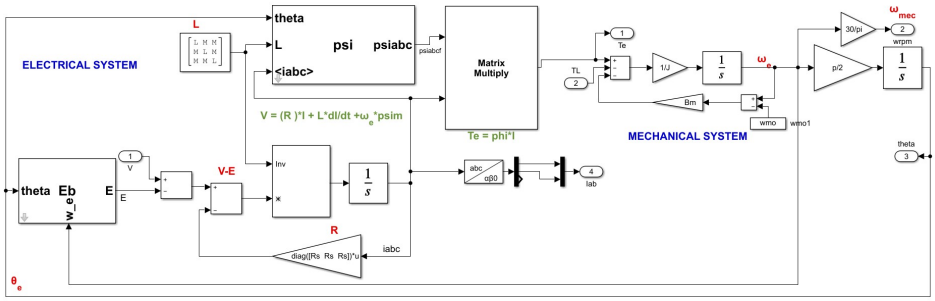

Figure 5.10: PMSM machine block under healthy case

5.5.2 Simulation setup and results

The simulation setting with the reference current applied at the machine is zero at the beginning and i_q = 3A at time instant 0.1 sec and i_d = -5A at time instant 0.3 seconds. The simulation runs for 0.4 seconds.

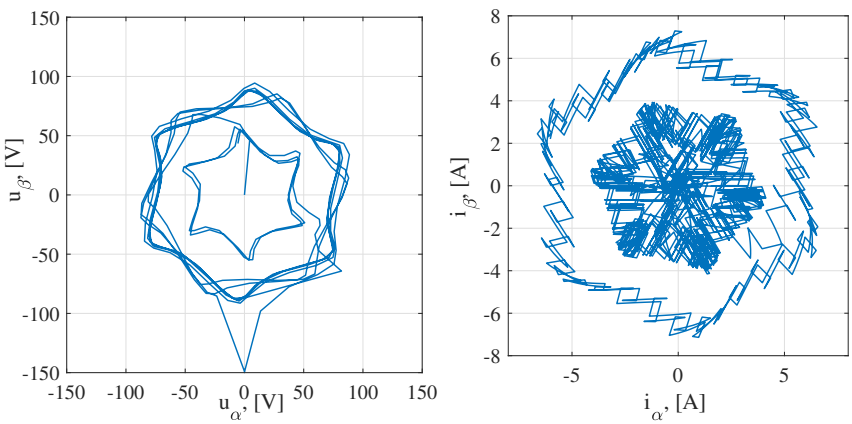

Figure 5.11: The voltage and obtained current from the controller and from the machine

In order to meet the reference current the voltage supplied by the controller in α-β reference frame is provided above with the current obtained in the same reference frame. There are different voltage sets that correspond to different modes. Tuning the gain and integral of the controller is dependent on machine parameters (Table 5.2) and sampling time. For the simulation, sampling frequency is 833Hz.

Figure 5.12 shows simulation results with the change in the demand current in both

d-axis and *q-axis* currents. The topmost figure is showing the increase in the phase voltage needed to achieve the desired current under motoring mode or when the current at *q-axis* is positive and reduction in voltage required when the applied current at d-axis is negative. The following two figures show a comparison of the desired and actual currents for i_d and i_q. It appears that the controller parameters have been tuned effectively to perform the analysis. The magnetic torque is shown in the last part of the graph where the average torque is zero for idling, 3 Nm for motoring, and 4 Nm for FW.

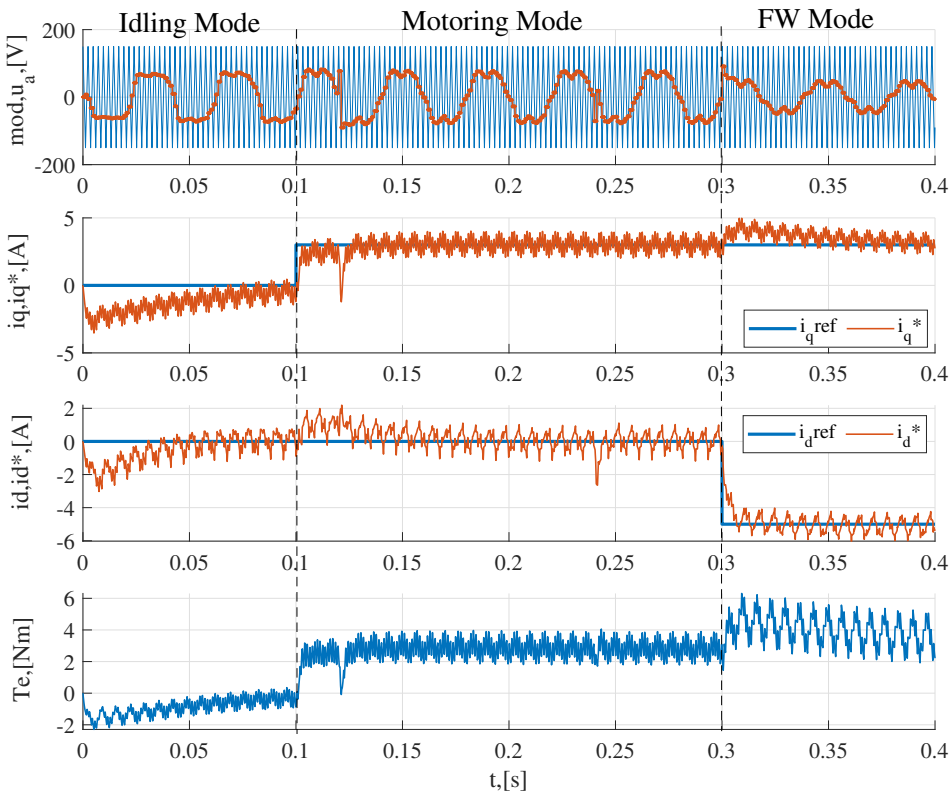

Figure 5.12: Vector control of 3 phase converter under healthy operation of PMSM

The purpose of this study is to better understand how the current controller works under different operating conditions. Taking the learning from the learning on healthy mode and applying it to unhealthy mode will help to better understand how unhealthy mode affects the controller response.

5.6 Simulation results with current controller - with ITF

This simulation is carried out by the same simulink model (Fig.5.11) except the equation system for PMSM is made by using equation 5.31 and the inductance matrix is 4x4 matrix.The resistance and the induced voltage matrix (4x1) are the major changes.

Induced Voltage Matrix -

The induced voltage is fed into the model using curve fitting of the induced voltage obtained from the FEM model illustrated in Figure 5.13, however curve fitting is made by using FFTs of exported induced voltages from FEM and they contain the amplitude of the subharmonics, but they do not take phase into consideration. Therefore, fitting a curve to the induced voltage signal using FFT was numerically equivalent, but apparently not in phase.

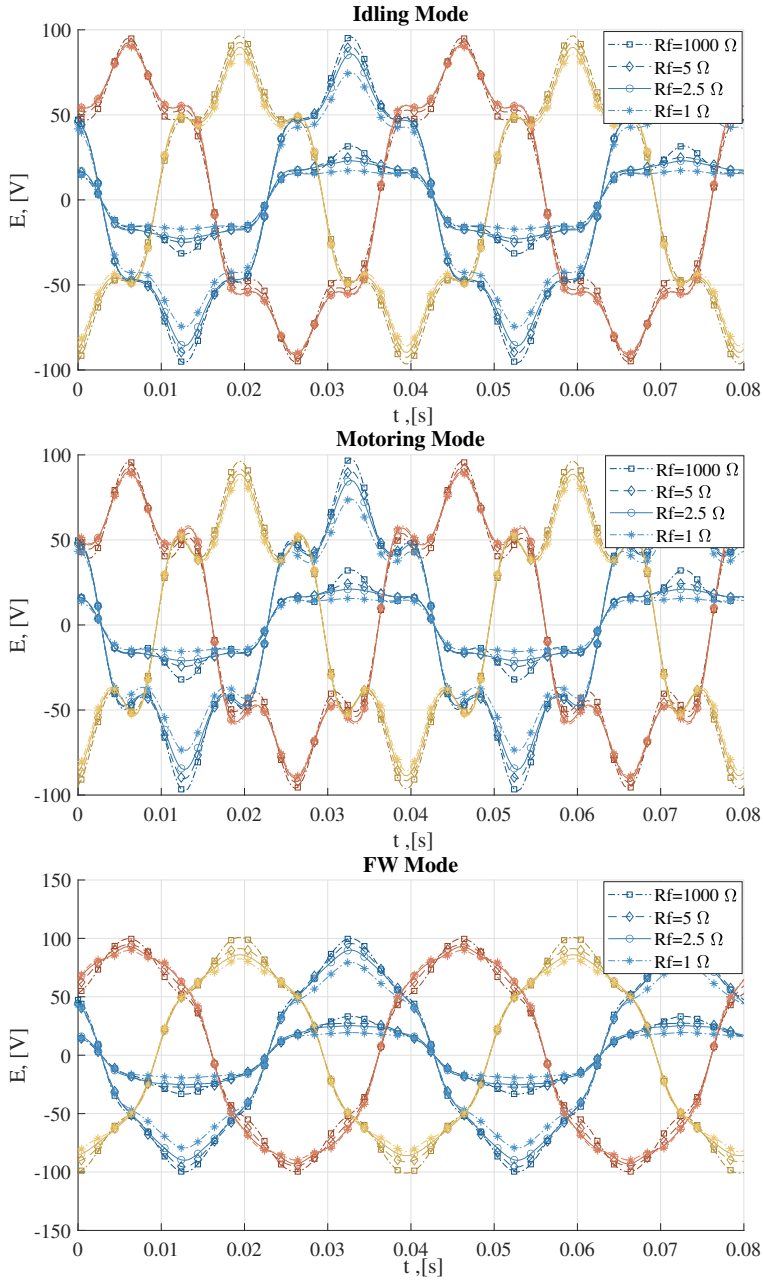

Figure 5.13: Induced voltage obtained from the curve fitting of the FEM exported values in the idling, motoring, and FW modes of phase a,b and c each have a different fault resistance across one coil

Simulation results

The current controller has already been described under healthy conditions, so it is interesting to see how it performs under faulted operation. The simulation settings are same as before. Simulations are conducted three times using a matlab script by changing fault resistance across one coil of *phase a*. In these simulations, the fault resistance varies from 1k to 5, 2.5 and 1 ohm.

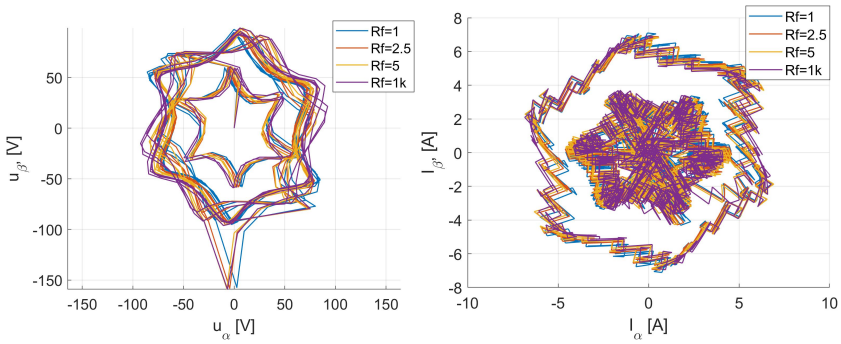

Figure 5.14: The voltage and obtained current from the controller and from the machine under different fault severity as R_f= 1, 2.5,5 and 1kΩ

Figure 5.14, shows the change in voltage requirement under varying fault resistances and current requirements at *d and q axes*. Rightmost figure shows the change in current at the stationary reference frame. Changes in voltage demand may indicate faulty behavior, but it is difficult to see them through the current flow.

Under varying fault resistance and under different operating modes, Figure 5.15 shows the change in current at *d and q-axes*. The machine operates in idling mode when the reference current at *q axes* is zero. During motoring mode, current is required at *q axes* at 3A, and during field weakening (FW), current is required at *d axes* at -5A, and current at *q axes* at 3A.

In comparison with the healthy case, the ripple content of the current increases and the controller requires more voltage to meet the same demand.

When looking at the currents at the *d and q* axes, it is difficult to detect the fault since the controller still works well under ITF.

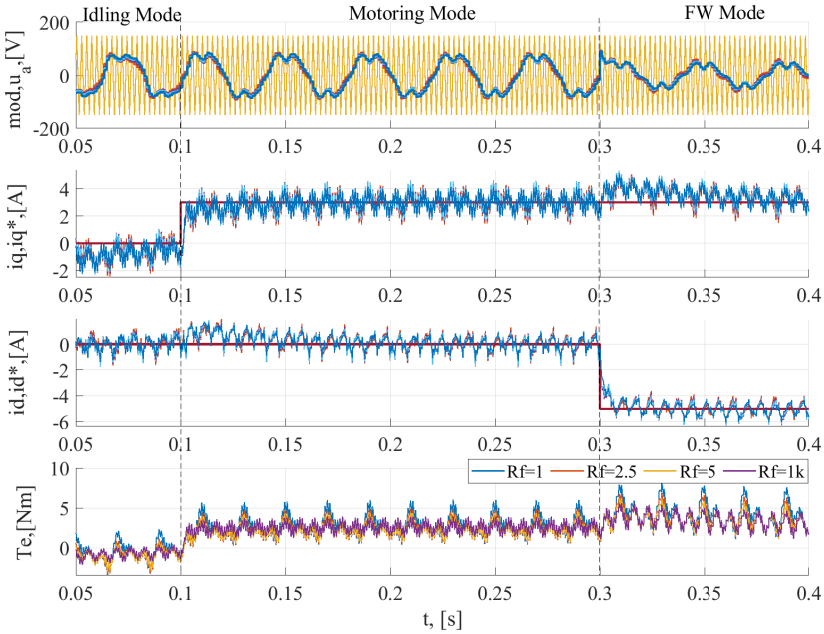

Figure 5.15: Current control of PMSM machine with ITF under different current and fault settings.

Stator flux linkages

When it is difficult to identify the fault signature from the current response, it is better to examine the effect of the stator flux linkage. The SFL response is then plotted under different reference frames here. This result is obtained from the block named SFDO. The block is described in chapter 7 for the sake of separating the modelling and detection part.

It's interesting to see the reduction in the SFL of alpha axis since the faults are created in *phase a* axes. Because of the faulted operation, the flux obtained is in opposition to the main flux, resulting in a reduction in the SFL with a decrease in fault resistance. SFL in the forward rotating reference frame is initially at 0.5 Wb in the d axis, but it changed based on the operating condition, and it further changed with the faulted resistance below the healthy operating values. The ASRF's SFL is also shrinking both in *d and q axes* with decrease in fault resistance.

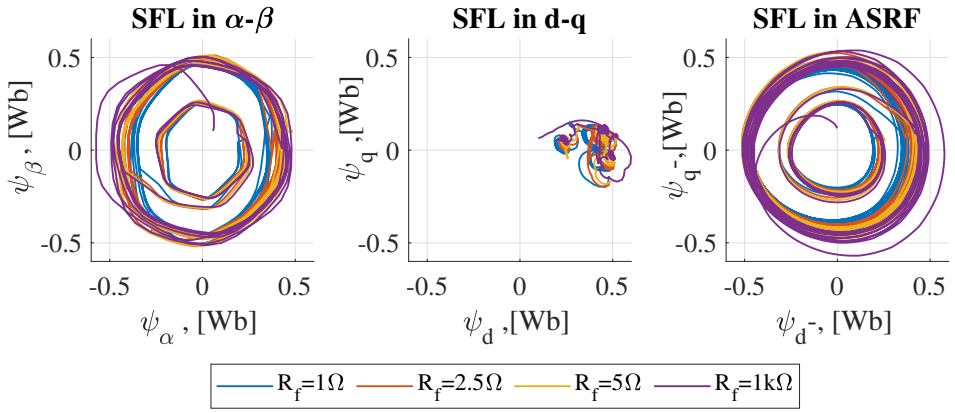

Figure 5.16: The SFL in stationary reference frame, ASRF and the SFDO

Fault current- In idling mode, the magnitude of the fault current is similar to that obtained without the controller. It is expected that the shape of the fault current curve will change due to the inclusion of induced voltage harmonics and the modulation of VSI. The fault current varies both with the various fault resistances and operating conditions. Maximum fault current flows under FW mode and it is 19.6A. In FW mode, fault current increases since the induced voltage across the faulty loop is higher due to adding up the field weakening effect of the negative *d axes* current. The peak value of i_f in motoring mode is 15A and steady state is 14.5A in steady state. There is a comparison between fault current obtained from FEM and this in Table 5.6.

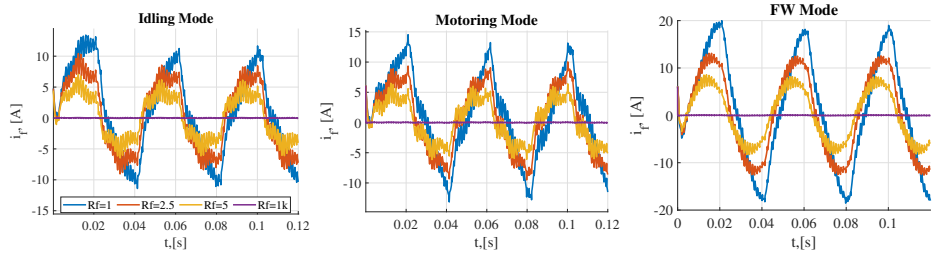

Figure 5.17: Fault current under different operating modes and fault resistances

Torque - The mechanical torque generated under different operating condition are provided in Figure.5.18. During idling, motoring and FW, the average mechanical torque (T_m) under healthy condition is 0Nm, 3Nm and 2.5Nm, respectively. Under different operating modes, torque ripples behaved differently. Under no load conditions, it is null since fault current is the only current flowing through the circuit. The torque ripple here depends on the fault current and the induced voltage across the loop. Torque ripple is suppressed due to suppression in fault current (when looking

in the figure from blue to purple). When the fault resistance decreases the torque ripple difference becomes apparent particularly at 1 Ω.

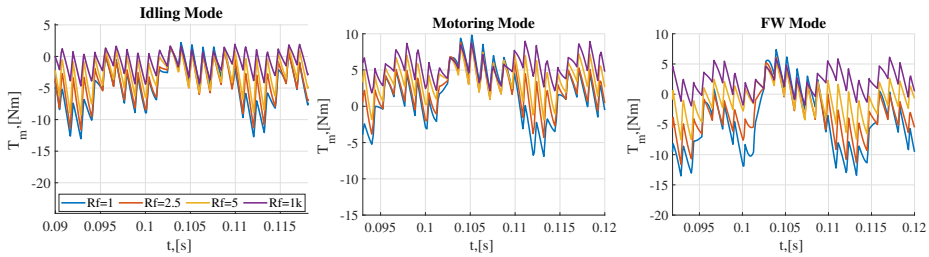

Figure 5.18: Mechanical torque under under different operating modes and fault resistances

5.6.1 Simulink model with position dependent (SM-PD) values from FEM

Comparatively to FEM results (chapter 6), the magnitude of fault current changes significantly when fault resistance becomes 1Ω. To resolve these differences, we attempt to make the model (SM-PD) closer to the FEM model by using position dependent values of inductances and induced voltages.

Induced voltages and inductances are exported from the FEM model to the simulink model using 1-D look up table. As the exported values are relative to position, only 101 data points are required. A position step of 3.6 degrees will be taken in this case until 360 degrees are reached. Time steps can also be used to do this, but more data points need to be used, and they need to be replaced with different speeds as well. The induced voltages and inductance values vary with operating modes. These can be seen in figures of chapter 6 from Figure 6.12 to Figure 6.24.

Using FEM-based position-dependent exported values for induced voltages and inductances in simulation, the magnitude of fault current at fault resistance 1Ω is still not comparable to the magnitude of fault current obtained by FEM to know the exact root cause a analysis is made in the following paragraph.

Simulation results-

This section shows only the fault current and torque since the operating conditions and simulation settings remain unchanged from earlier. The obtained SFDO's and SFLs can be seen in chapter 8.

Fault current - The fault current is obtained as before with similar fault resistances under different operating modes. In idling and motoring modes, the fault current corresponds well with 5 and 2.5 Ω resistances. However, when load resistance becomes equal to 1 Ω, the fault current does not match the results of FEM. Under

different operating modes, position-dependent values improved the phase difference and shape of the fault current.

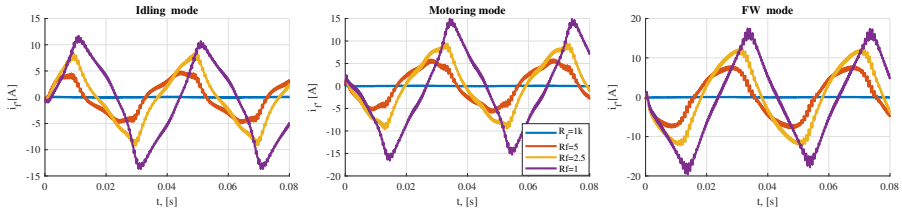

Figure 5.19: Fault current under different operating modes and fault resistances are in ohms

A comparison of peak value of the fault current from SM-PD , FEM and the results obtained from the constant parameters (SM-CP)is tabulated in Table 5.6. Here, the peak value of fault current is taken from Figure 5.17, 5.19 and 6.25.

Table 5.6: Comparison of fault current [A] derived from different models under different operating modes

Idling Mode			
Fault resistance,[Ω]	FEM model	SM-CP	SM-PDP
1	27	12.6	14
2.5	11.2	10	10
5	5.4	5.4	5.3
Motoring Mode			
1	25.81	14.5	15
2.5	10.4	9.3	10
5	4.4	5.4	5
FW Mode			
1	36.3	19.6	20
2.5	21.5	12.4	12.6
5	12	8.3	8.3

Under different operation modes, the model works reasonably well when the fault severity is low or the fault resistance is high. However, when there is a low fault resistance, the model is not able to detect the severity of the fault. So, what could be the reason behind that? The analytical expression of fault current can be determined by using the last column of the analytical equation given in equation 5.32.

$$-e_f = L_{a2}\frac{di_f}{dt} + (\mu R_s + R_f)i_f - M_f\frac{di_a}{dt} - M_{a2b}\frac{di_b}{dt} - M_{a2c}\frac{di_c}{dt} \tag{5.43}$$

To simplify, let's start with an idling mode with zero phase currents, resulting in the equation below-

$$-e_f = L_{a2}\frac{di_f}{dt} + (\mu R_s + R_f)i_f \tag{5.44}$$

$$i_f = -\frac{e_f + L_{a2}\frac{di_f}{dt}}{(\mu R_s + R_f)} \tag{5.45}$$

The fault current flowing in the faulty loop, the induced voltage across the L_{a2}, and the inductance of the faulted coil are plotted together in the idling mode for the 1Ω case and illustrated in the figure 5.20.

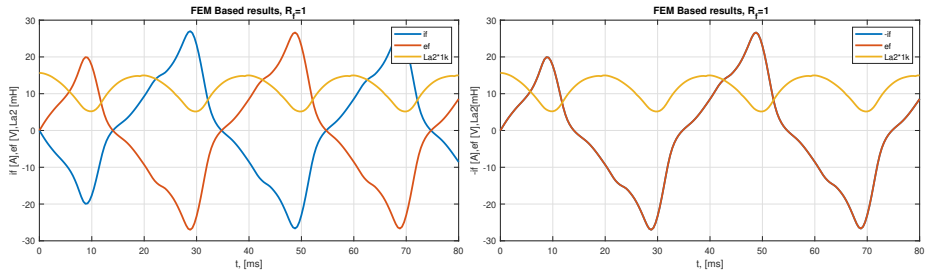

Figure 5.20: An illustration of the induced voltage e_f, fault current i_f and faulted inductance L_{a2}

It is obvious from this comparison that the fault current is synchronous and in phase with the induced voltage. As a result, the impedance of the faulted loop becomes resistive and the fault current follows the following equation as 5.46.

$$i_f = -\frac{e_f}{R_f} \tag{5.46}$$

However, the parameter exported from the FEM study does not show the same inductance variation. Based on the FEM results, the faulted coil inductance L_{a2} varies from 15mH to 5mH. Based on these parameters, the simulink model results in a low fault current because of the high impedance of the faulted loop.

Simulink's model can be corrected easily under low resistance when the machine is idling, but in other operating modes the presence of phase currents makes it more difficult.

In order to accurately model the transient behavior of the PMSM, a flux-based (*d-q*) or inductance-based PMSM model needs to be adopted which takes into account cross-coupling, magnetic saturation, and temperature effects[6, 5].

5.7 Summary

A detailed analysis of PMSM analytical model is presented in this chapter, both for healthy and faulted systems. Stator flux linkages, fault current, and torque equations are analyzed in MATLAB for both scenarios. The fault models together with current control is further analysed to see the effect of change in the demand current and how the fault current is changing the parameters like SFL, torque and the voltage provided by the controller to the control setup. Having found that the analytical model using constant inductances and curve fitted induced voltage could able to produce the same fault current as the analytical model utilizing position-dependent values of inductances and induced voltages could, the same model is extended to the analytical model using position-dependent inductances and induced voltages. Despite this, position dependent values are still unable to match the fault current generated by the FEM study in chapter 6 when the fault resistance become 1Ω and under FW mode.

5.8 Learning outcomes

- Solving ODE using different solvers in both Simulink and Matlab under different scenarios also helped to understand the singularity in the matrix system, and how to set the relative tolerances to avoid it.
- Understanding the current controller, vector control, and how effectively it can provide the reference current by looking at the induced voltage to find the rotor position and generate the voltage by the current controller under various operating modes.
- Developed an understanding of fault modeling through the use of FEM based fault parameters (both constants inductances and position-dependent parameter matrix of inductance and induced voltages).
- Aiming to export position-dependent values, it helped extend the understanding of rotor angle references and how to associate them with models. If these aren't set correctly, this further increases the difference in fault current.

References

[1] A. Djerdir J. A. Farooq, T. Raminosoa and A. Miraoui. "modelling and simulation of stator winding inter-turn faults in permanent magnet synchronous motors". *COMPEL: The International Journal for Computation and Mathematics in Electrical and Electronic Engineering*, 27(4):887–896, 2008.

[2] F. Meibody-Tabar A. Djerdir J. Farooq B. Vaseghi, N. Takorabet and A. Miraoui. "modeling and characterizing the inter-turn short circuit fault in pmsm". *Electric Machines Drives Conference (IEMDC), IEEE International,*, pages 551–556, 2011.

[3] R. Krishnan. *"Permanent Magnet Synchronous and Brushless DC Motor Drives"*. https://doi.org/10.1201/9781420014235, 2010.

[4] Dubar Christian. "recent advances in modeling and online detection of stator interturn faults in electrical motors". *PhD thesis. Division of Electric Power Engineering Department of Energy and Environment Chalmers University Of Technology*, 2016.

[5] F. Meibody-Tabar A. Djerdir J. Farooq B. Vaseghi, N. Takorabet and A. Miraoui. "modeling and characterizing the inter-turn short circuit fault in pmsm". *Electric Machines Drives Conference (IEMDC), 2011 IEEE International,*, pages 551–556, 2011.

[6] Mats Alaküla. *"On the Control of Saturated Synchronous Machines"*. 1993.

Chapter 6

Parameter identification using FEM model

In this chapter, the FEM model is presented for determining fault parameters under ITF. Firstly, setting up the model using geometrical details, and later performing the fault analysis using an external circuit. The parameters like inductances and back emf are identified and extracted under various fault and operating conditions. These parameters later used in fault diagnostic via proposed method in chapter 7.

6.1 Introduction

Fault diagnosis begin with modeling and determining parameters of the machine with a turn fault. Under ITF, fault parameters like inductances, back emf or induced voltage and stator flux linkages depends on the geometry and winding arrangement[1, 6]. A faulty coil's inductance and its mutual inductance with surrounding coils can be identified by analytical equations based on fault fraction[2, 6], magnetic circuits[1, 6], and reluctance grids[3, 6], as mentioned in literature. There is, however, difficulty in visualizing the distribution of magnetic flux. In a machine with a fault, the current and flux density distribution changes more or less when the fault severity increases. The distribution of magnetic flux impact the shape and size of the induced voltage (backemf) across the healthy and faulty coils. A realistic design of the machine usually produces a non-sinusoidal induced voltages. Considering the importance of induced voltages shape in validating an analytical model [4, 6], harmonics cannot be ignored and can be acquired from FEM models in both healthy and faulty conditions.

A simplified model is provided by chapter 5 through analytical modeling.Physical arrangement does not influence the derived analytical model, since the analytical model is more general and is not directly dependent on the structure or winding arrangement. It is only through the parameters of the machine that these aspects impact the model indirectly. Therefore a FEM based study is conducted to study machine behavior under fault conditions and identify the parameter like inductances and induced voltages under faulty conditions. As well, a detailed analysis of parameters under fault and in various operating conditions is conducted.

6.2 FEM model of healthy PMSM

The geometry of machine is based on a prototype machine available at the electrical machine laboratory at Chalmers university of technology[5, 6]; this machine has been selected due to the availability and due to access to coils points in machine (Table 5.2). From Figure 6.1, the modelled machine has three phases, three pole-pairs, a interior permanent magnet motor, nine teeth and concentrated windings (CW).

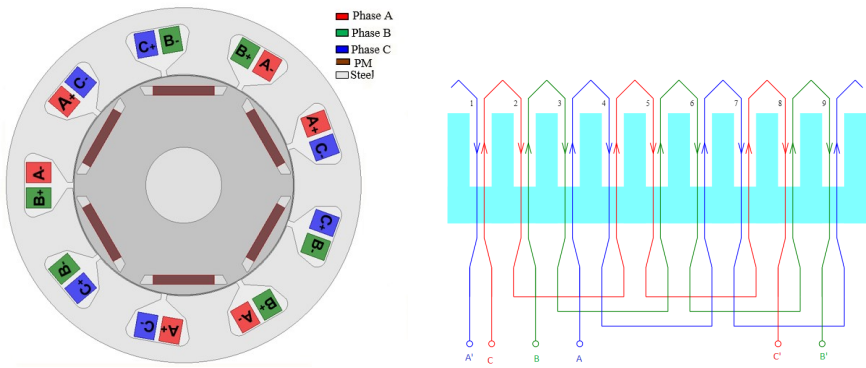

Figure 6.1: FEM model of the machine representing the complete machine and the individual winding arrangement of each coil

The coil arrangement also shown in the left hand side of the figure, where "-" index indicates that positive current is entering into the paper. Each phase has three series-connected coils as shown in the right hand side of Figure 6.1.The machine has nine slots wound with concentrated windings. Each tooth has a single coil wounded around it, which consists of 48 turns leading to a total of 144 turns per phase.

Model is built with the help of RMxprt using Ansys electronics desktop. Ansys electronics desktop is one of the Ansoft corporation softwares well known for finite element method modeling.In this work, Maxwell is mainly used to build, analyze and

extracting the fault parameters of the permanent magnet synchronous machine under inter turn fault. The Maxwell models can be linked to the Twin Builder for co-simulation for system based study.

6.2.1 RMxprt

Ansys RMxprt is the template based electrical machine design tool .With RMxprt, a basic motor design can be implemented along with performance evaluation, a reduction in the design space for the motor, and a development of the motor's Maxwell two-dimensional finite element model (Fig. 6.1).

In RMxprt its required to specify some motor parameters, such as the stator and rotor diameters, the slot, the iron core length, the insulation, winding's, and the permanent magnet size and material type. A few assumptions and the motor's specified rating were used to perform design calculations. As a final step, the Maxwell model is imported into Ansys Electronic Desktop for further processing and co-simulation. Below is a step-by-step procedure for creating an in-depth machine model starting from stator design.

First steps towards designing is to select the right template and input the source type, structure , stator type and rotor type.

Table 6.1: Machine specification

Name	Value and Unit
Source type	DC
Structure	Inner Rotor
Stator Type	Slot-AC
Rotor Type	PM-interior

6.2.2 Stator design details

Inputting the correct stator, rotor, and winding details is the next step to model the machine. The parameters used in the design of the stator core, slot, and windings are listed below in Table 6.2.

Stator core, slot and winding

By selecting a template from a number of stator slot templates, a stator core is created. Figure 6.2, shows what the core design looks like after inputting the stator parameters. The parameters which were input to the RMxprt model of the machine are categorized in Tables 6.2. Majority of the stator dimensions are taken from [5, 6]. The dimensions of some stator slots were assumed, including R_s, H_{s1} and H_{s0}, B_{s1} and B_{s2} were calculated from given slot area. A Y type 3 phase with drive type connection is the circuit type for the given model.

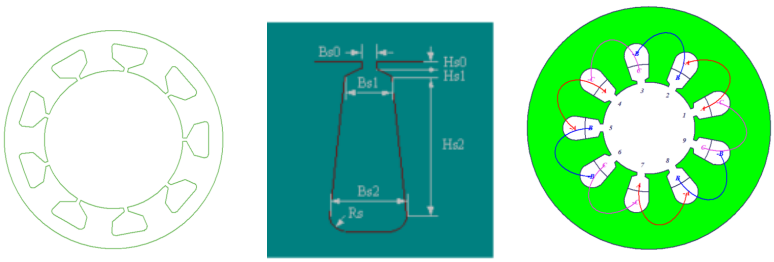

Figure 6.2: Design of stator core, slot and stator winding

Table 6.2: Stator core, slot and winding dimensions

Parameters	Value
Outer stator diameter	190 mm
Inner stator diameter	118.6 mm
Air-gap length	0.7 mm
Stack length	120 mm
Stacking factor	0.95
Steel type	$M310-50A, 50Hz$
Number of turns	48 per tooth
Wire diameter	1.4 mm

Parameters	Value
Number of stator slots	9
Yoke thickness	12.8 mm
Tooth width	22.6 mm
Shoe height, inner(Hs2)	9.6 mm
Shoe height, outer	3 mm
Slot opening width (Bso)	3.5 mm
Slot area	481 mm^2
Slot dimension (Rs)	3 mm

6.2.3 Rotor design details

Figure 6.3, illustrates the internal permanent magnets of the rotor. This rotor pole design template is available in RMxprt. According to [5, 6], magnet thickness and magnet width are obtained, while other parameters related to magnet duct dimensions are inputted after visual inspection. The following table provides magnet dimensions and rotor diameter information.

Table 6.4: Rotor core, magnet pole dimensions

Parameters	Value
Rotor diameter	118.6 mm
Shaft hole diameter	40.6 mm
Number of poles	6
Steel type	$M310-50A, 50Hz$
Magnet type	NdFe35

Parameters	Value
Magnet thickness	5 mm
Magnet width	33 mm
Magnet duct dimension O2	29mm
Magnet duct dimension B1	5mm
Magnet duct dimension Rib	14mm

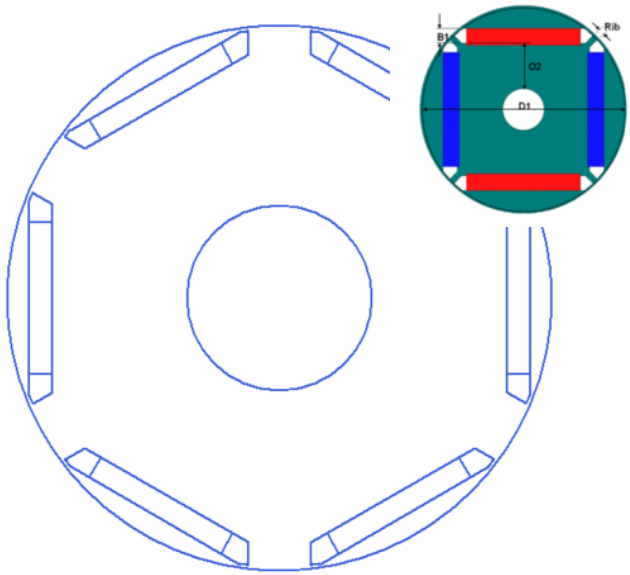

Figure 6.3: Design of rotor

6.2.4 Machine Specification

In order to simulate the RMxprt, some further machine specifications must be provided, which are shown in Table 6.5.

Table 6.5: Machine specification

Name	Value and Unit
Operating type	Motor
Load type	Constant Power
Rated output power	4kW
Rated voltage	106V
Rated Speed	3000rpm

The next step was to export the model to a 2D model. This was accomplished using Maxwell software, which generates 2D models from RMxprt files. As a result of this functionality, all necessary information for a 2D transient analysis is generated. The exported 2D model from the exported RMxprt model is shown in Figure 6.4.

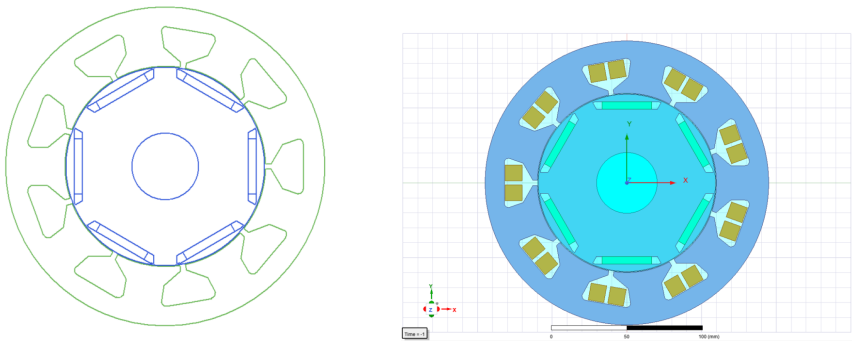

Figure 6.4: RMxprt and Maxwell 2D Model

6.2.5 No load study

After setting up the 2D model, no load studies have been conducted. During no-load conditions, the stator phase is excited with zero current and is spinning at a speed of 500 rpm. Below is a graph showing the obtained flux and current density for the motor obtained under this study. Between the bridges, there is a maximum flux density of 1.9 T and a strong equipotential line of flux of 0.0149Wb/m.

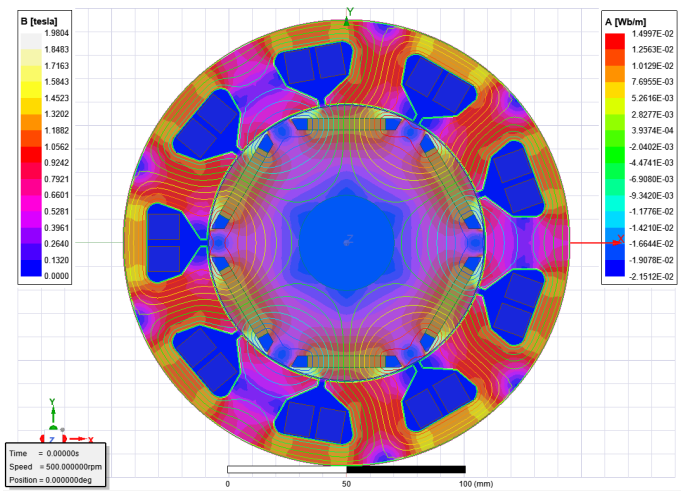

Figure 6.5: Flux density distribution at no load

6.2.6 Inductance of a healthy machine

To determine the self and mutual inductances, a magneto-statics solver is used. Magneto-statics solver provides inductance and coupling between coils in matrix form. Simulating the FEM model under magnetostatic solver would give self and mutual inductance of any phase and across phases. Under this simulation setting, a DC excitation of 1A is given to a phase and other phases are forced to have zero excitation and the magnets are moving incrementally from 0 to 360 degree. In this simulation the material chosen for the stator and rotor is linear iron, for the magnets it is Neodymium and the coil material is copper.

Through this, self and mutual inductance with respect to rotor position of phase *a* and with respect to other phases can be determined. As can be noticed from the Figure 6.6, the inductance varies with rotor position, which is to be expected for machines with interior permanent magnets. Self inductance of machine is the summation of flux in each tooth of a machine divided by the current flowing in that phase.

$$L_{aa} = \frac{\Psi_{aa}}{i_a} \tag{6.1}$$

While the mutual inductance between any two phases (lets consider *a* and *b* for instance) relates the flux from *phase a*, linking the coils of *phase b* and the current in *phase a* .

$$L_{ab} = \frac{\Psi_{ab}}{i_a} \tag{6.2}$$

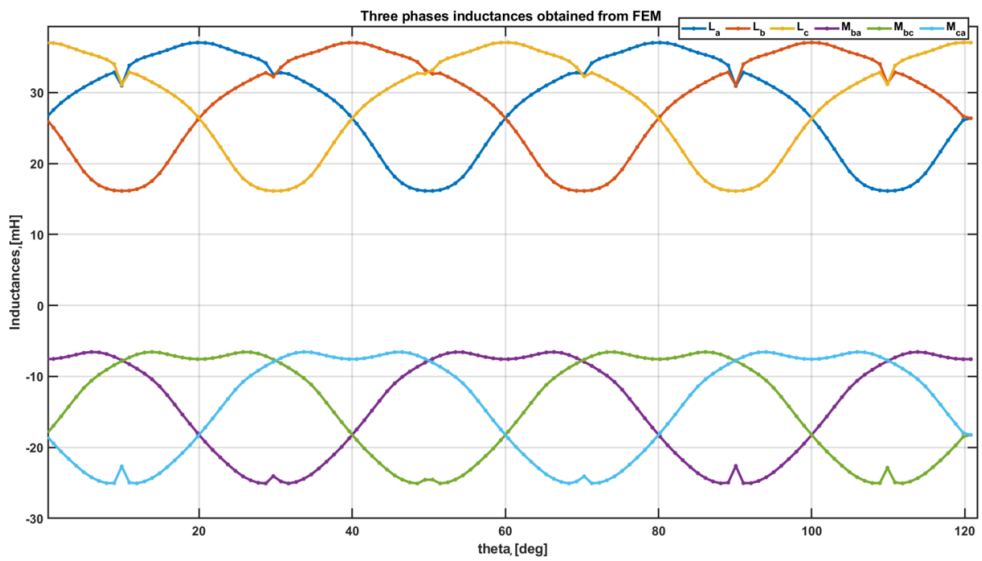

Figure 6.6: variation of self and mutual inductance w.r.t to rotor position

The average value of inductances obtained from FEM tabulated below;

Table 6.6: Average value of Inductance obtained from FEM

Parameters	Value,[mH]
$L_a = L_b = L_c$	28.4
$M_{ab} = M_{bc} = M_{ca}$	-14.02

Inductance equations

By [6, 6], the inductances of the stator windings are defined as functions of rotor electrical angles(θ_r). L_d and L_q are the self-inductances of the d and q-axes windings, respectively.

$$L_{dc} = \frac{1}{2}[(L_d + L_q)]; L_{ac} = \frac{1}{2}[(L_q - L_d)] \tag{6.3}$$

where:

- L_{dc} represents the self-inductance of the stator winding per phase. This is the average self-inductance of each stator winding.
- L_{ac} represents the fluctuation in stator inductance. With changing rotor angles, self-inductance and mutual inductance fluctuate according to this value.

With this information, the phase inductance can be evaluated:

$$L_a = L_{dc} + L_{ac}cos(2\theta_r) \tag{6.4}$$

$$L_b = L_{dc} + L_{ac}cos(2\theta_r - \frac{2\pi}{3}) \tag{6.5}$$

$$L_c = L_{dc} + L_{ac}cos(2\theta_r + \frac{2\pi}{3}) \tag{6.6}$$

$$M_{bc} = M_{cb} = -\frac{1}{2}L_{dc} + L_{ac}cos(2\theta_r) \tag{6.7}$$

$$M_{ab} = M_{ba} = -\frac{1}{2}L_{dc} + L_{ac}cos(2\theta_r - \frac{2\pi}{3}) \tag{6.8}$$

$$M_{ac} = M_{ca} = -\frac{1}{2}L_{dc} + L_{ac}cos(2\theta_r + \frac{2\pi}{3}) \tag{6.9}$$

Below is a comparison of average inductance obtained from analytical equation (equation 6.4 and 6.7) and from FEM based simulation.

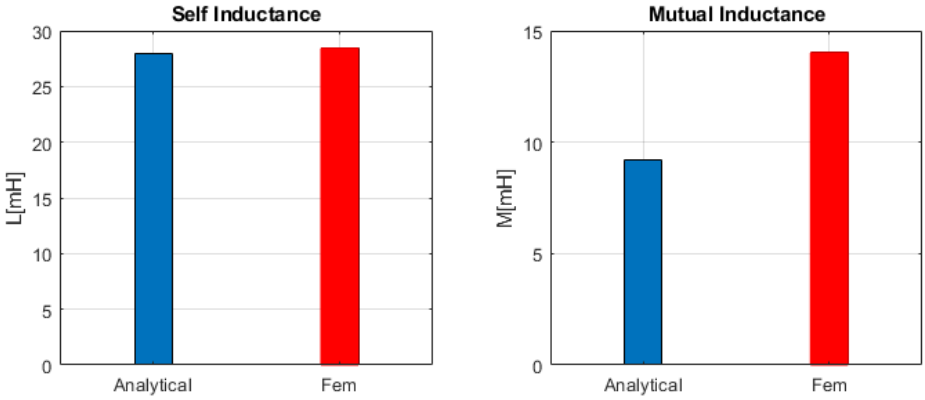

Figure 6.7: Comparison between self and mutual inductance obtained from the equations and the FEM model.

For the self inductance, the analytical method agrees well with FEM, but for the mutual inductance, the spread is wider. The bar graph shows mutual inductance as positive for ease of reading. A coil arrangement in the machine has a strong mutual coupling between different coil phases, which might explain the disagreement.

6.2.7 Back emf of healthy machine

The back-emf in PMSMs is induced by the movement of the rotor magnets relative to the stator coils; the amplitude of the back-emf is determined by this movement. As long as the flux amplitude from the permanent magnet is constant, the induced voltage amplitude is proportional to rotational speed. Induced voltage waveforms depend on the amount of flux within coils, which is in turn determined by the design of the machine.

With the help of the FEM model, we can understand the shape and harmonic distribution of the induced emf across the coils and across the whole phase.

In analytical model, the back emf represented in equation 5.40 is due to movement of permanent magnets around the coils. The phase currents are forced to zero in order to acquire the voltage induced in coils only due to rotation of permanent magnet, and the FEM model is simulated with a mechanical speed of 107rpm using the FEM transient solver. Using FEM software, the voltage induced in coils is calculated by taking the derivative of the total flux. Here, the phase back emf is the resultant sum of induced voltage across three series connected coils. The obtained back emf from the FEM study is shown in Fig. 6.8.

Model initialisation

To ensure the model at FEM is trustworthy, no load experiments were conducted in the laboratory on the machine and compared the extracted back emf with the result obtained from FEM. Based on the obtained value, the back emf waveform from the experiment and the Maxwell model shows good agreement for further study.

Table 6.7: Measured and FEM based obtained value of induced voltage

Parameters	Model	Experimental
E_a	18.37	17.2

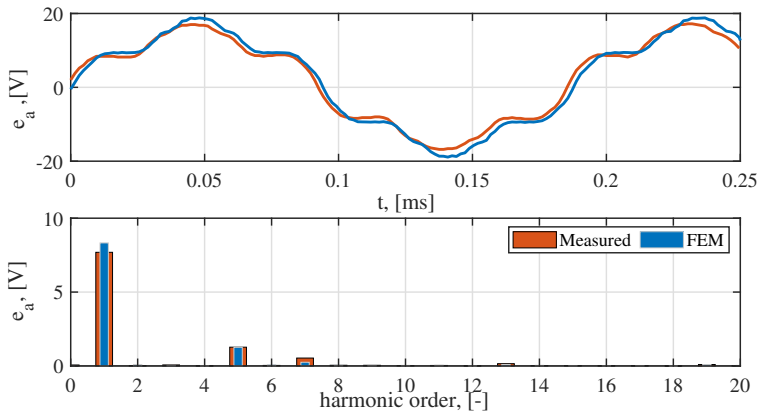

Figure 6.8: Comparison between back emf obtained from lab and from FEM model.

Figure 6.8, shows that the back emf is not a perfect sine wave and contains low-order harmonics. It is possible to observe from a Fourier analysis of the back emf that besides the fundamental component there are also low-order (5th and 7th) harmonics present. The harmonic components are independent of the machine's operational speed under no load.

6.3 FEM model of unhealthy machine

An external circuit is used to connect the similar fault set up as experimental setup in the model using Ansys twin builder[7, 6]. System simulation is conducted using Maxwell's 2D model and Twin Builder. Co-simulation refers to this process.

6.3.1 Fault creation using Co-Simulation(Maxwell/Twin Builder)

6.3.2 Model setup

An FEA-based PMSM model with the ITF in *phase a* is illustrated in Figure 6.9. Inductances and resistances at the end of a turn are represented by R_{ae} and L_{Ae}, respectively. For each coil end-turn inductance L_{A2e}, we choose 1mH and resistance R_{A2e} to be 100mΩ, respectively. Total and remaining end-turn inductance are L_{Be} is 3mH and L_{Ae} is 2mH, respectively. i_a, i_b and i_c are input currents to *phase a, b and c* , respectively.

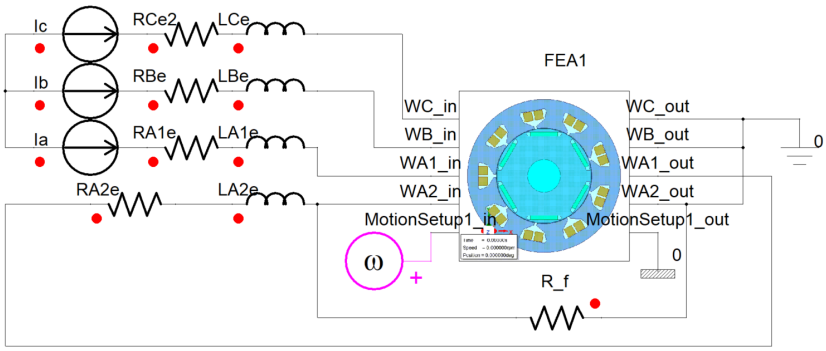

Figure 6.9: Coupling of Maxwell model with twin builder for ITF setup

In *phase a*, there are two coils connected in series and represented as, WA1 and WA2. R_f across coil WA2 represents the gradual deterioration of winding coil insulation. To replicate current control in FEM, the machine is fed by a three-phase current source. The ITF is set by varying the fault resistance R_f. The resistance of the fault resistor R_f in the simulation is changed from 5, 2.5 to 1Ω. With the speed source component (shown in the Figure 6.9), as a constant mechanical speed source was applied to the Maxwell machine model. The machine runs at 500 rpm with no load.

Model initialisation with ITF

An experimental measurement of fault current is carried out to verify the FEM model results under similar fault conditions. The fault current i_f is measured through *phase a's* coil loaded with a 5Ω resistor in parallel with the middle of the three series connected coils. The fault current from the FEM model is 6.1 A and measured i_f from test machine is 6.9 A as shown in Figure 6.10. Based on the comparison results, FEM Model and experimental results appear close, but when calculating the percentage change w.r.t their peak they differ by 13 %.

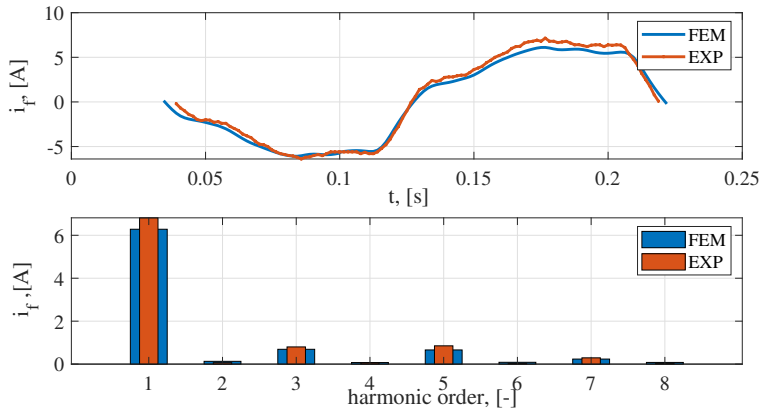

Figure 6.10: Comparison of fault current based on lab measurements and FEM models.

After validating the model, next step is to identify parameters under different conditions and fault severity levels.

6.3.3 Simulation approach and operating modes

Simulation approach:

The co-simulation with twin builder is set to runs in two ways.

I - The total simulation time is 160ms and after every 40ms the fault resistor R_f in the simulation is changed from 1k, 5, 2.5 to 1 Ω respectively.

II. - The simulation time is 80ms, and the fault resistorR_f is parametrically changed from 1 k, 5, 2.5 to 1 Ω respectively.

Operating Modes:- Three different case studies are made in order to understand and parameter identification under idling mode, motoring mode and field weakening (FW) mode. In all the cases degradation of insulation is approximated with a fault resistance (R_f) connected across the one coil of phase *a*.

Table 6.8: Operating Modes

Operating Modes	Current [A]	Speed [rpm]
Idling Mode	I_q =I_d = 0	500
Motoring Mode	I_q = 3, I_d = 0	500
FW Mode	I_q = 3, I_d = −5	500

Input current - Simulations are run under each operating mode by feeding the input current into the model as shown in Figure 6.11. In motoring mode, the peak current

is 4.2A, while in FW mode, it is 5A.

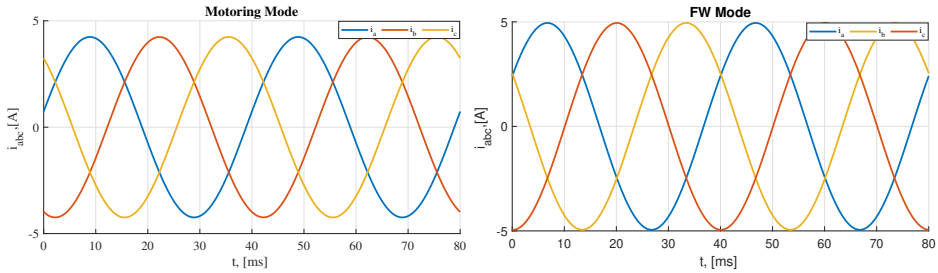

Figure 6.11: Input current under motoring and FW mode

6.4 Parameters Identification

A fault diagnostic simulation model relies on the identification of inductances [8, 6]-[9, 6], mutual inductances, fault inductances and coupling from the faulty coil to the healthy coil in the same phase or linking to other phases. Another important parameter is the induced voltage across the phases and the faulty coil. The FEM based results are showing the change in the induced voltage across other healthy phases as well. The reason behind this is a stator flux linkage between the faulty coil and its neighbouring coil, which affects the induced voltage of the same phase as well as the phase adjacent to it. The mutual effect is studied in under stator flux linkages and induced voltage study. The distribution of magnetic flux impact the shape and size of the induced voltage across the healthy and faulty coils.

Inductances - The waveforms of machine inductances in the healthy and faulty cases can be a good approximation of inductance matrix needed for analytical equation. Inductances under different fault severity cases are obtained using transient cosimulation in FEM. Parameters are obtained in all modes, but they are shown here only for idling. The idling modes is performed as described in simulation approach II. From Figure 6.12, obtained inductances oscillate due to the air gap variations by rotating machine. The average value of self (L) and mutual (M) inductances are 28 mH and -14 mH under healthy condition. When the fault resistance is placed across one coil of any one phase in this case is *phase a* the average values is varying with $\pm$ 1% .

The three phase self and mutual inductance is shown below under different fault resistances. The variation of faulted inductances like L_{a2}, M_f, M_{a2b}, M_{a2c} with different fault resistance has also shown under it and their average inductance values are tabulated in Table 6.9.

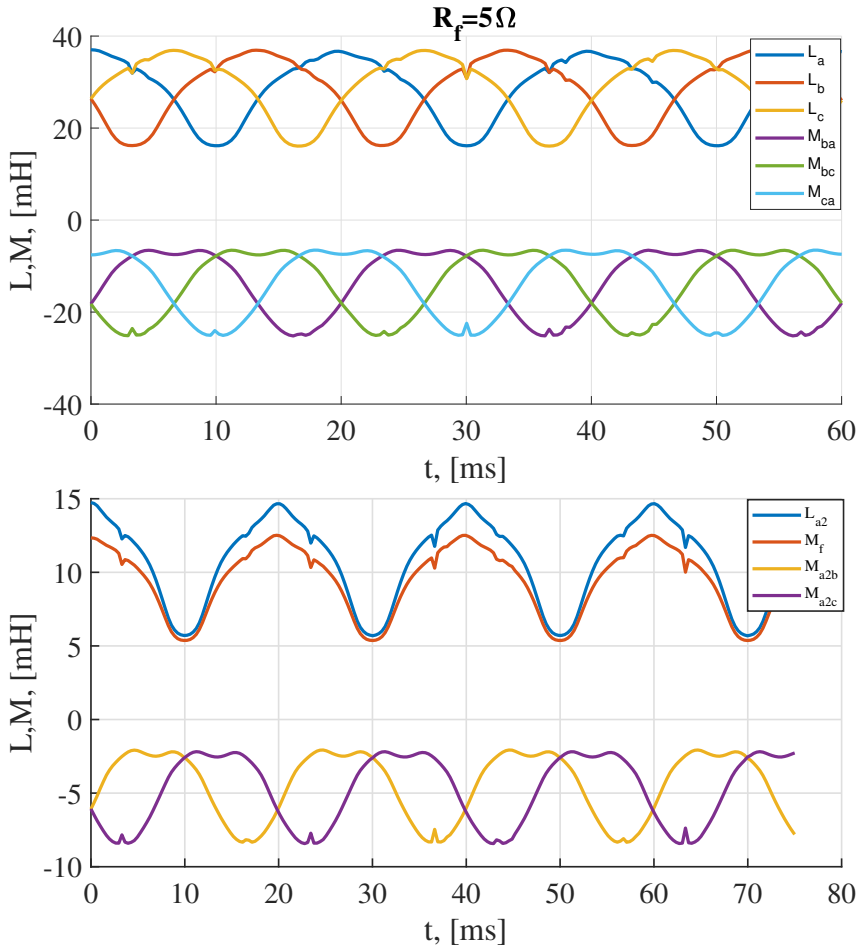

Figure 6.12: Three-phase self and mutual-inductance variation as well as faulted inductance variation at 5Ω

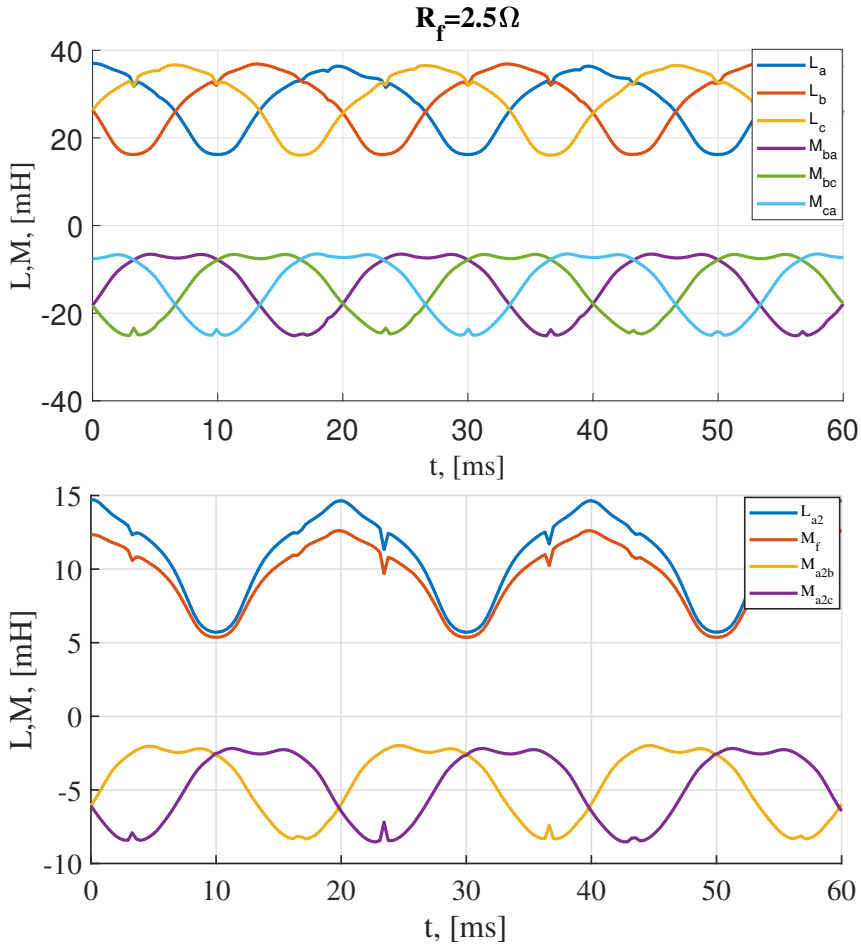

Figure 6.13: Three-phase self- and mutual-inductance variation as well as faulted inductance variation at 2.5Ω

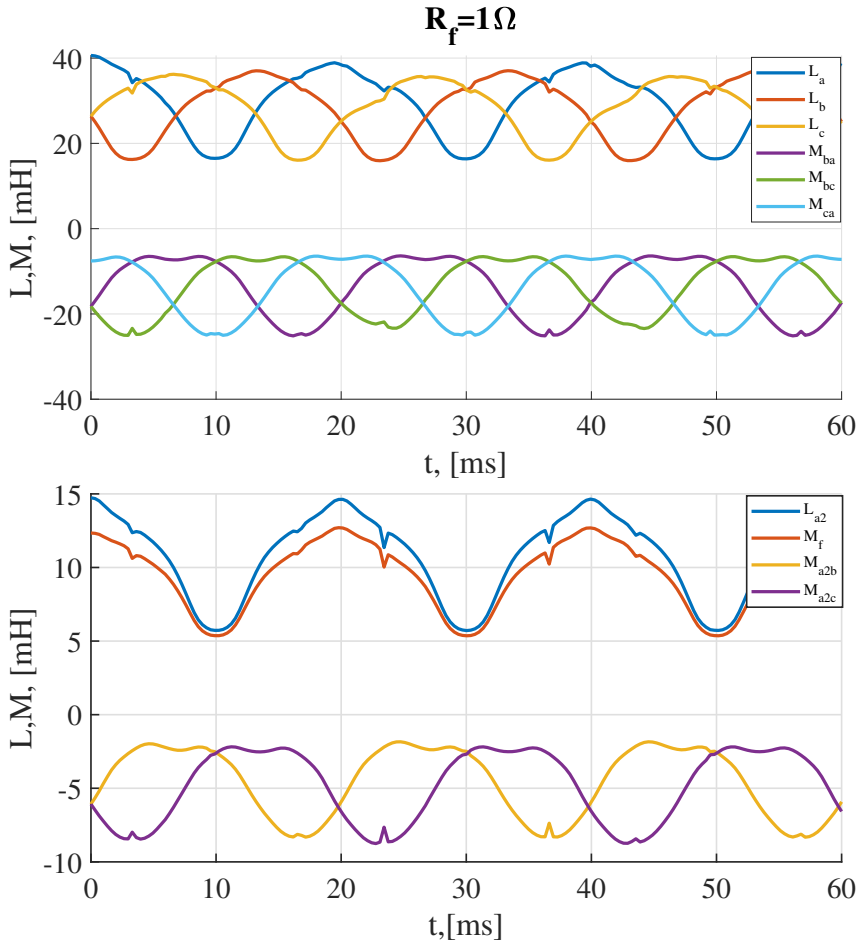

Figure 6.14: Three-phase self- and mutual-inductance variation as well as faulted inductance variation at 1Ω

Plotting the self- and mutual inductances of three phases over each other shows how they vary in response to fault resistance and rotor position.

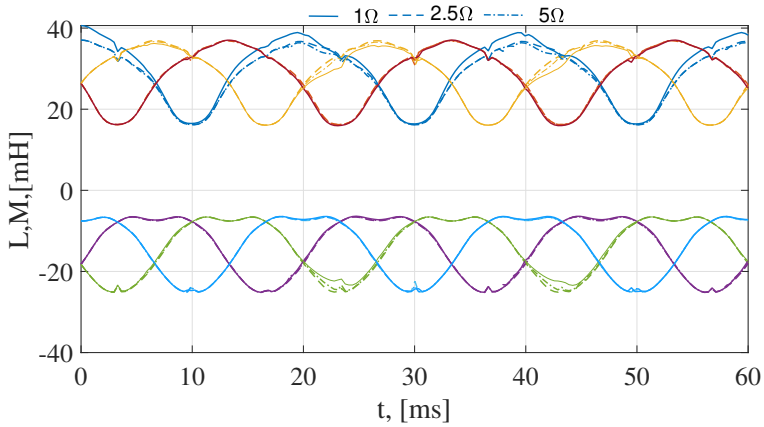

Figure 6.15: self inductance of phase *a* ,*b* and *c* is shown with blue red and yellow while the mutual inducatance between *ab*, *bc*, and *ca* are shown with purple, green and light blue respectively.

A simulation approach I is used again to show the effective changes with respect to the fault resistance. Figure 6.16, showing the variation of the faulted coil self inductance and mutual inductance with respect to both the fault resistance and the rotor position. An average value of self and mutual inductances of the faulted coil with it and with other phases is listed below. L_{a2} and M_f only changed 1% when R_f changed from 1k to 1Ω, however mutual inductance increased 7.5%. The difference in mutual coupling between the fault coil and *phase b* and *c* respectively, is due to machine geometry and direction of rotation. In this case the fault has occurred in coil A2 where the neighbouring coils are C2 and B3. The flux produced by the faulty coil reaches a coil belonging to *phase b* is less than the *phase c* due to the rotating direction and hence the coupling values are bigger than *phase b*.

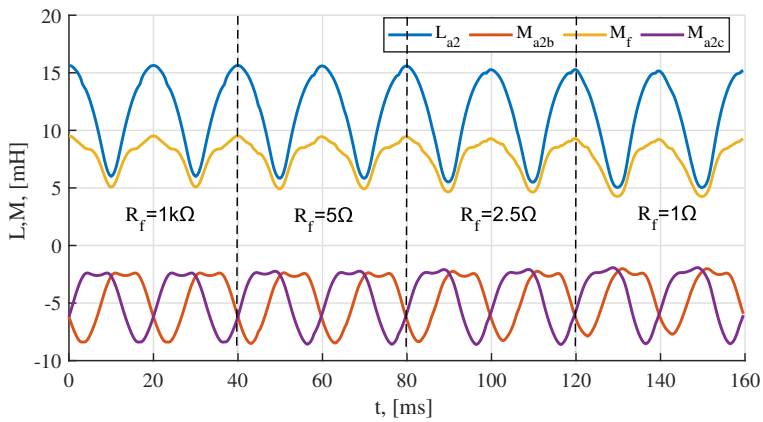

Figure 6.16: La2,Mf,Ma2b,Ma2c (faulted inductance) of a faulted winding under varying fault resistance

Table 6.9: FEM based obtained mean value of faulted coil inductance in [mH]

Fault Resistance	L_{a2}	M_f	M_{a2b}	M_{a2c}
R_f= 1k	10.69	9.51	−4.43	−4.79
R_f= 5	10.69	9.51	−4.43	−4.79
R_f= 2.5	10.63	9.56	−4.6	−4.76
R_f= 1	10.55	9.58	−4.11	−4.43

Following this, in chapter 5 and 7, while performing fault modeling and fault diagnostics, FEM based obtained inductances both as the average values and position dependent values are used.

Stator flux linkages

The stator flux linkage (SFL) under an inter-turn fault can be expressed mathematically as:

$$\psi_s = L_s i_s + \psi_{pm} + \psi_f \tag{6.10}$$

In the equation, ψ_s represents the stator flux linkage, L_s is the stator inductance matrix, i_s is the stator current vector, ψ_{pm} is the permanent magnet flux linkage, and ψ_f is the additional flux linkage caused by the fault.

SFL occurs due to PM flux linkage and fault current flowing across the faulty coil in this case. The behavior of the magnetic fields and stator flux linkages under different fault conditions is studied using the circuit shown in Figure 6.9. Through the use of different fault resistances R_f, an ITF is created which replicates the different stages of fault development. R_f is reduced from 1k to 1Ω.

The flux linkage across the faulty phase decreases with decrease in R_f as shown in Figure 6.17. Due to a decrease in SFL across coil A2, this is the case. There is a reduction in flux linkage of the faulty phase due to fault currents, which act in opposition to main SFL. In addition, since the total flux linkage is the vector sum across all three coils, with a reduction in flux linkage, the total flux linkage decreases. Similar observations are made under different operating modes as well.

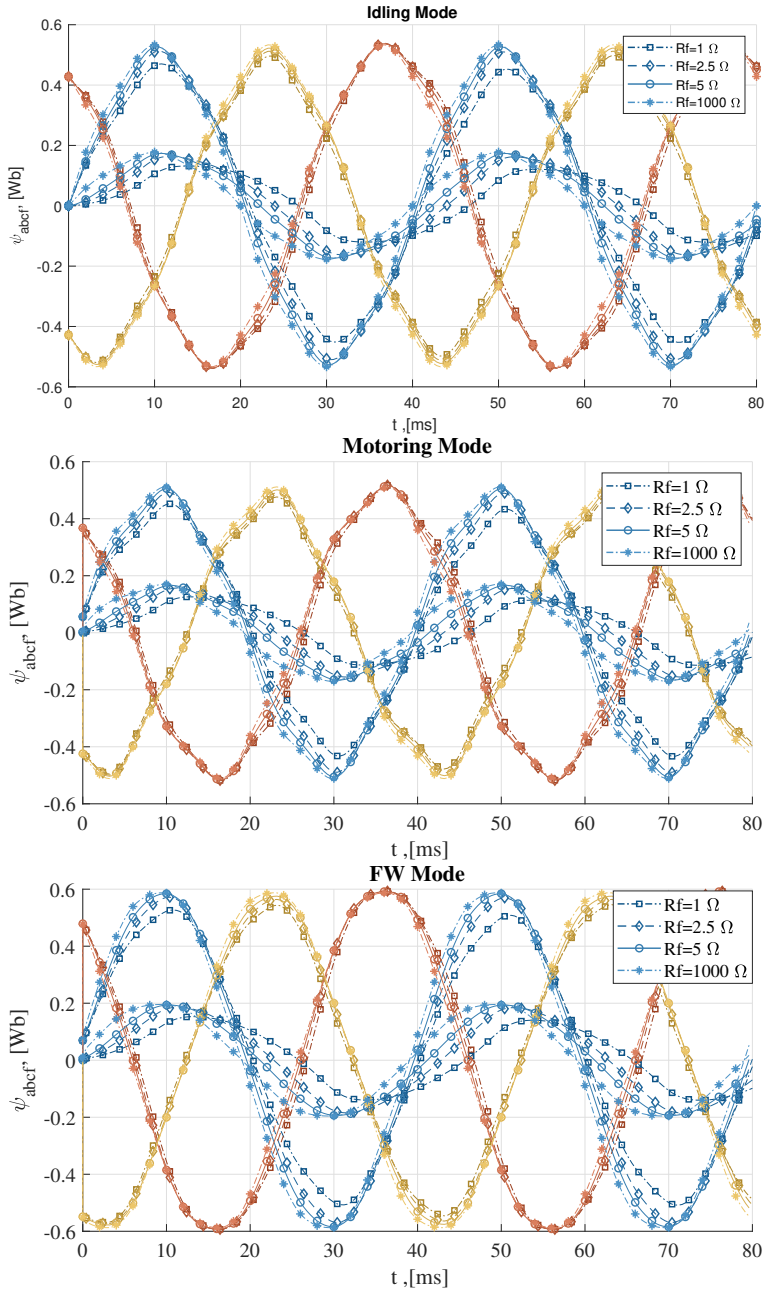

Figure 6.17: The SFL in phase a, b and c and across the coil A2 under idling, motoring and FW mode with varying fault resistance

Although it's understandable that the SFL decreased across the faulty phase, it's interesting to see that it also changed in the other phases.

The winding distribution affects flux linkages in *phase c* and *b*. In *phase b*, the SFL decreases with a decrease in R_f, but in *phase c*, it increases. The reason behind the change in SFL across phases *b* and *c* is an excess flux linkage between the faulted coil and nearby coils, as shown in Figure 6.18. The top of the figure explains the excess flux linkage in phases *c* and *c2* which are nearby. The same phenomenon can be observed in phase *b* when the machine runs in opposite direction.

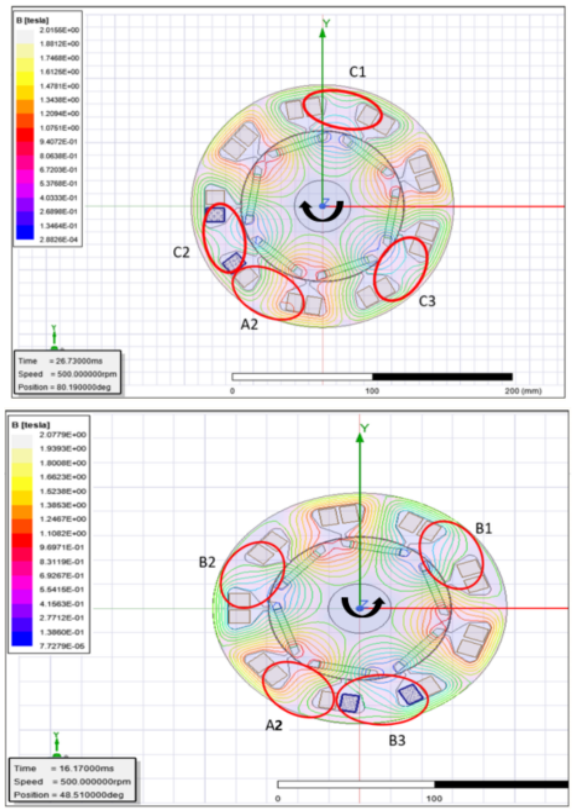

Figure 6.18: Flux line distribution when coil A2 is loaded with R_f. On the top, the machine is rotating clockwise and on the bottom, it is rotating anticlockwise.

Induced Voltage

In healthy conditions, the induced voltage across each phase is symmetrical. A three phase SFL becomes unsymmetrical when resistors are added to any coil of the phase, resulting in an unsymmetrical three phase induced voltage. As observed through SFL under fault conditions the SFL in *phase c* is maximum while it reduces in the faulty *phase a* with R_f and also in the other *phase b*. SFL's behavior and movement across the other phases are explained above.

In order to verify the SFL crossover phenomenon experimentally, the induced voltage is examined across each phase when one coil of *phase a* is loaded with R_f as 1 Ω. The machine is rotating at 500 rpm under field oriented control. The following Figure 6.19 shows the change in back emf obtained from FEM model and lab experiments when the machine rotates clockwise (500) rpm and anticlockwise (-500rpm).

A similar explanation can be given for the maximum voltage across *phase b* when the machine rotates anticlockwise. This machine's total induced back emf is a vector sum of the induced voltage across each coil. By loading R_f onto coil A2, an increased current flows across the coil due to low resistance. As a result of this high current, flux lines begin to move across the coil, and the flux lines start moving across the neighboring coil as well as shown in Figure 6.18. During clockwise rotation, the flux line across coil C2 increases, resulting in higher induced voltage across coil C2. Consequently, the induced voltage increases across the *phase c.* SFL crossover understanding is also supported by similar experimental observations as the FEM model. For this phenomenon to be included in the analytical model, the back emf and its frequency components needs to be updated under different operating conditions with different induced voltage amplitudes. Therefore, the back emf is obtained via FEM model in different operating modes.

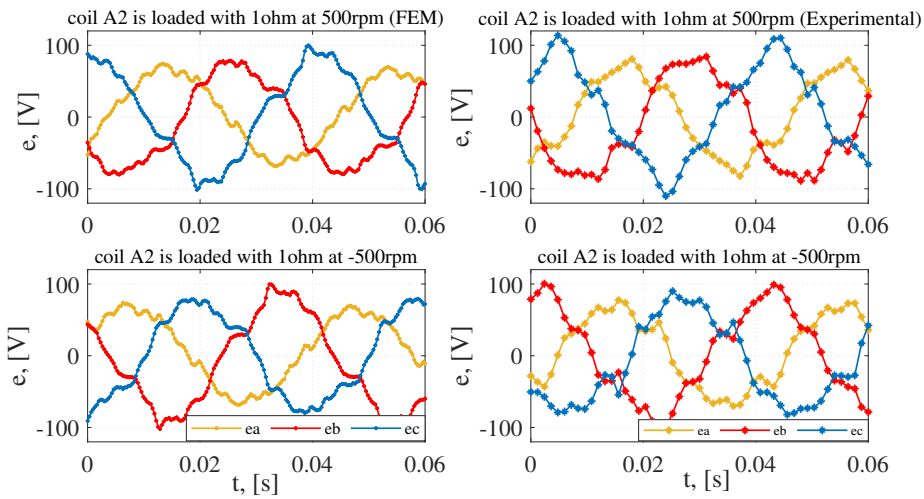

Figure 6.19: Three phase back emf obtained from FEM model and through the lab experiments

Idling mode

Under idling mode, the back emf across three phases only varies due to the flux change induced by the rotation of permanent magnets. *Phase a* is represented by blue color and the color get darker with lower R_f that means lower the R_f darker will be the

color shade. *Phases c* and *b* are represented by red and yellow, respectively. Under it, the harmonic distribution of induced voltages is also shown with same color codes.

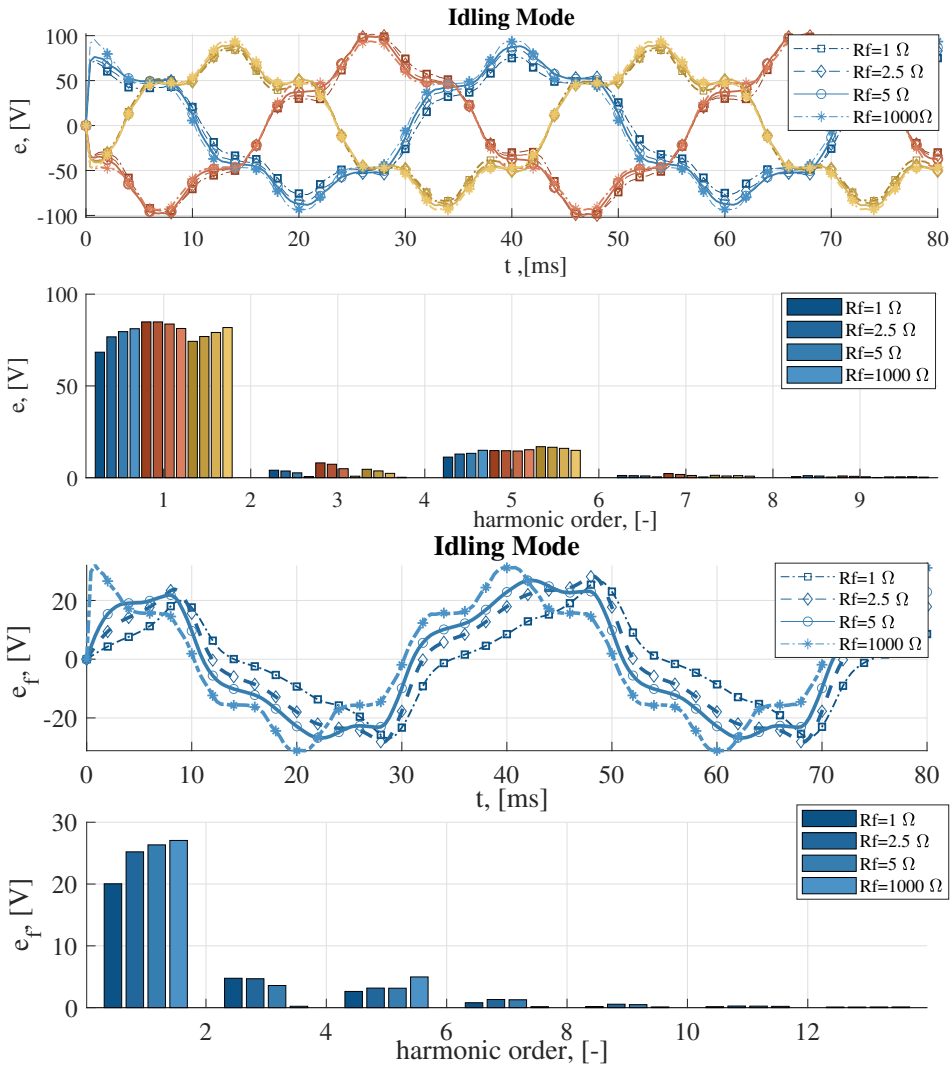

Figure 6.20: Three phase back emf and the induced voltage across the faulted coil when R_f is connected across the coil under Idling mode

Based on the results, the back emf of phase *a* and *b* decreases while in case of phase *c* it increases with decrease in fault resistance. Under healthy conditions, induced voltage reaches 93V across all phases. In phase *a* and *b*, it drops to 75V and 83V, respectively, while in phase *c* it increases to 101V when R_f is 1Ω. On the other hand, if we look at the harmonic distribution, then the fifth harmonic component decreases and third

harmonic component increases as R_f decreases.

On the bottom of Figure 6.20, is shown the induced voltage across the faulty coil, along with its harmonic distribution.Under healthy conditions, induced voltage across faulty coil is 31V and it drops to 26V when R_f is 1Ω. The third harmonic increases with decrease in fault resistance, while the fifth harmonic decreases with increase in fault resistance, which causes induced voltage or fault current to change shape.

Motoring mode

In motoring mode, the back emf is induced by both the magnetic flux changes caused by the permanent magnets and the phase currents. As a result the shape of the induced voltage is different as compared to idling mode. Under motoring mode, the induced voltage has higher fifth and seventh harmonics.

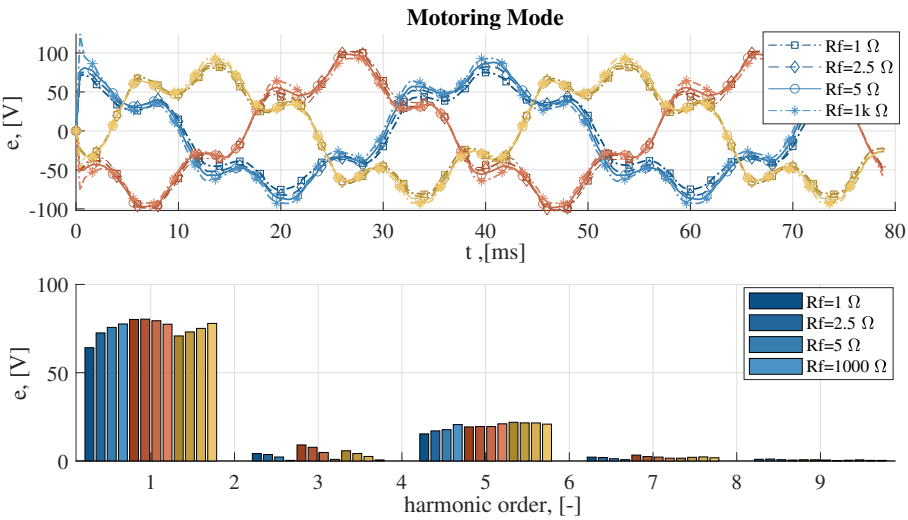

Figure 6.21: Three phase back emf when R_f connected across the coil A_2 under motoring mode

Under motoring mode, the induced voltage across faulty is shown below. Like, idling mode the third harmonic increases with decrease in fault resistance, while the fifth harmonic decreases with increase in fault resistance, which causes induced voltage or fault current to change shape as well.

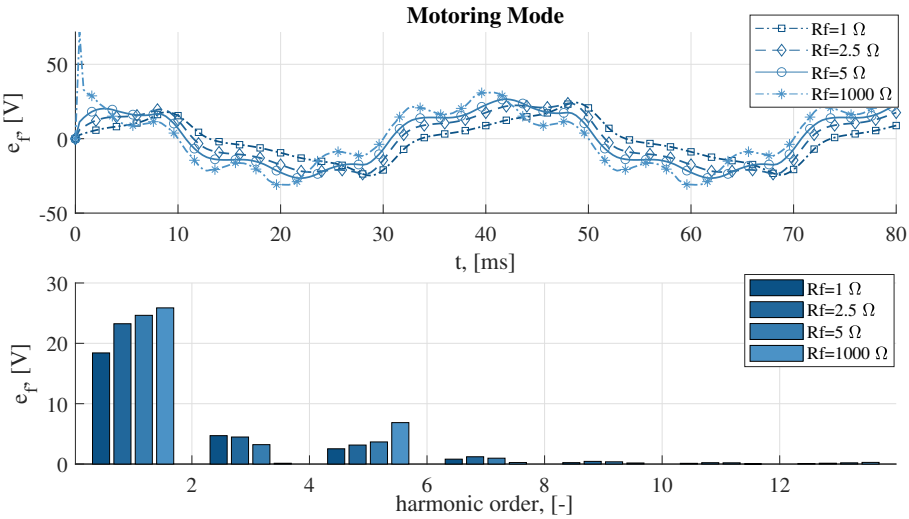

Figure 6.22: The induced voltage across the faulted coil under variable R_f

FW mode

Three phase induced voltage is shaped by negative current in the *d axis*. As shown in the plotted waveform below, the maximum induced voltage is across *phase c* approximately 112V when R_f is 1Ω in this mode. Compared with other modes, harmonics were suppressed, and the induced voltage waveform appears sinusoidal.

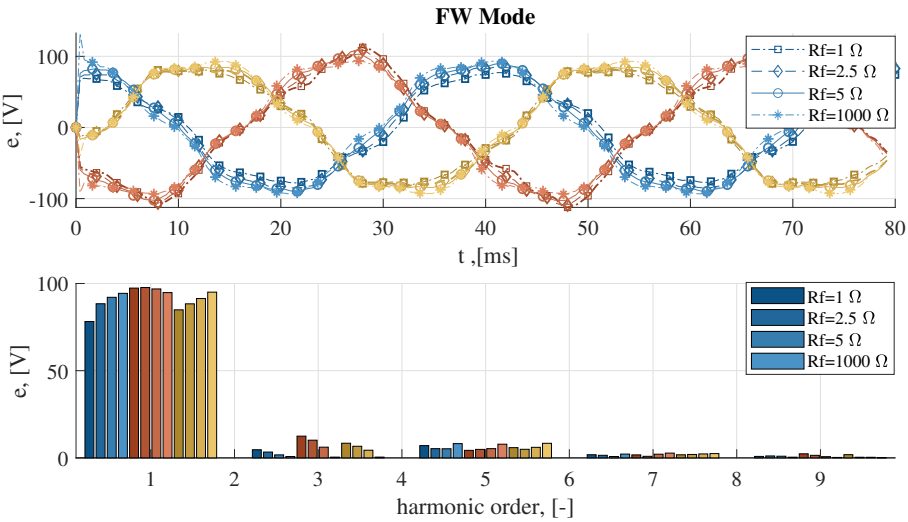

Figure 6.23: Three phase back emf when R_f connected across the coil under FW mode

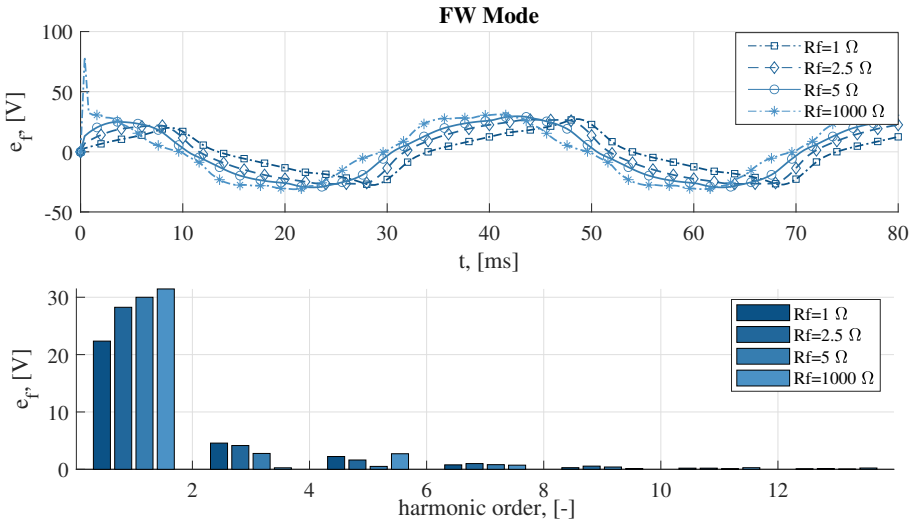

Figure 6.24: The induced voltage across the faulted coil under variable R_f

Fault current

With varying fault resistance, the figure below shows the fault current obtained for each operating mode. Fault current increases with decreasing R_f and reaches its maximum 26.7 A when the R_f is 1ohm in idling mode and 31A and 40 A when the machine is in motoring and FW mode respectively. Under different operating modes, the fault current flows with a difference in amplitude and shape due to the change in the shape of the induced voltage across the fault coil.

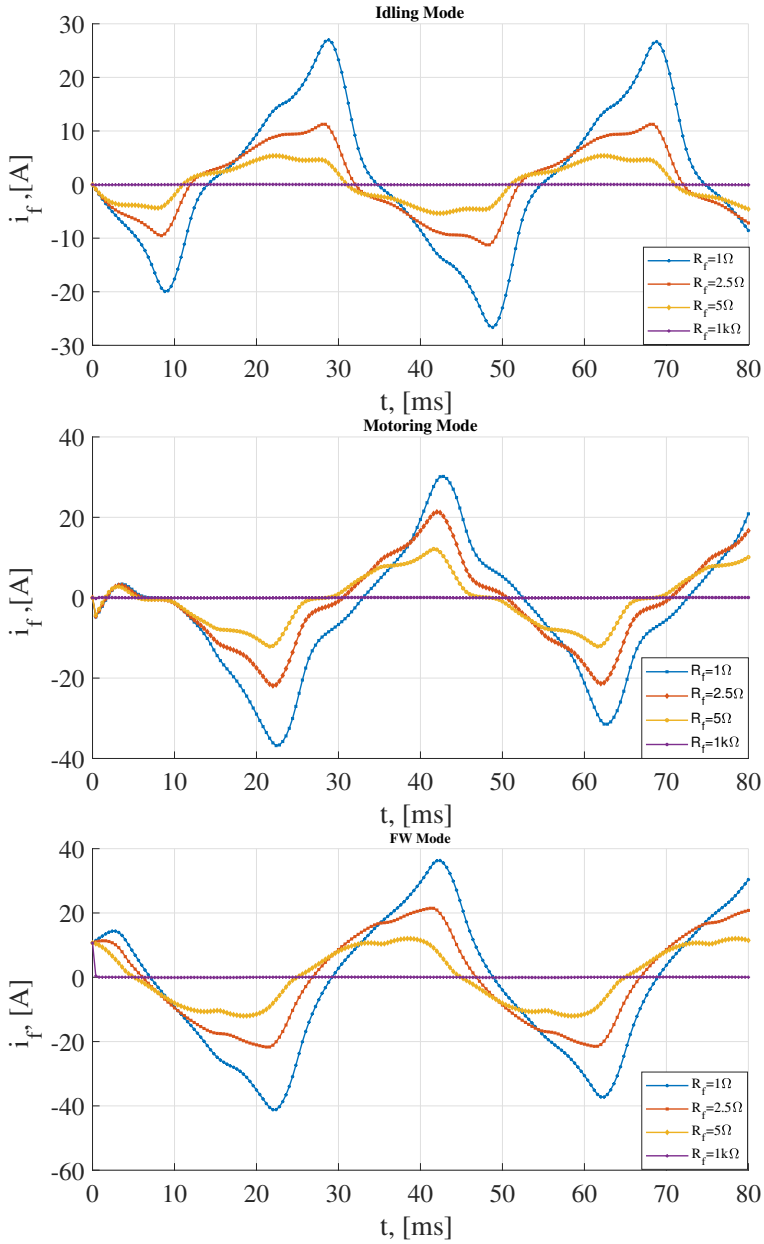

Figure 6.25: Fault current under idling, motoring and FW mode

Based on the results of this study, the fault current obtained is higher than the fault current obtained from a drive system or a model with a current controller in chapter 5. A comparison of the peak value of fault current obtained from different models under different operating modes is made in chapter 5.

Torque ripple

The torque ripple under various operating modes is investigated using simulation approach II and shown below in Figure 6.26. The ripple is caused mainly by $e_f i_f$ in the torque equation below:-

$$T_{el}\omega_e = e_a i_a + e_b i_b + e_c i_c - e_f i_f \tag{6.11}$$

Low resistance increase the fault current and the uneven distribution of the magnetic field can cause variations in the electromagnetic torque, leading to increased torque ripple. The ripple component introduced by the ITF has a larger amplitude compared the ripple due to cogging for the healthy machine. The average torque decreases with decrease in R_f as a result of an increase in torque ripple under different operating modes.

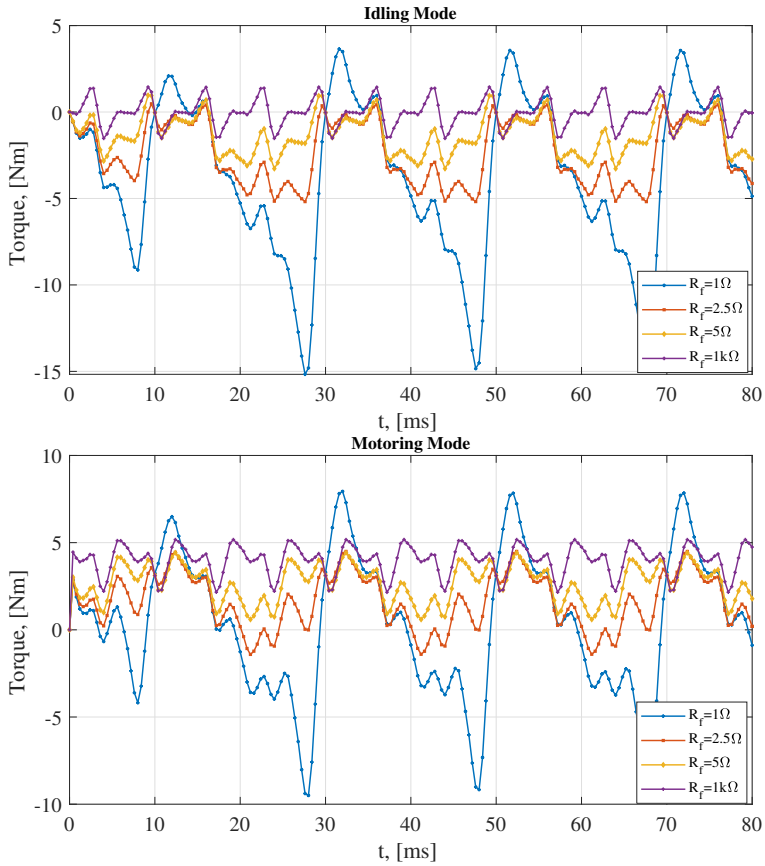

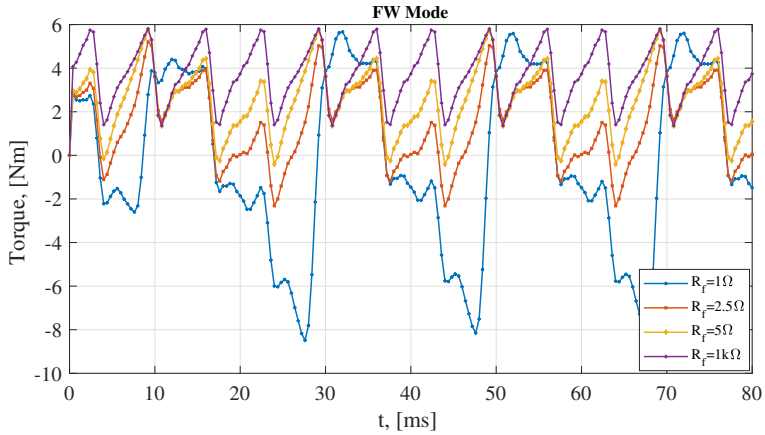

Figure 6.26: Electric torque variation with different fault resistance under the idling, motoring and FW mode

6.5 Summary

In this chapter, FEM models were presented for both a healthy PMSM and one with an interturn fault. The fault was introduced into the FEM model using twin builder. The circuit was then simulated with a circuit software in a co-simulation environment with more realistic connections between the faulted coil and the affected phase. The built FEM model is initialised by experimental results. Additionally, this FEM model runs in different operating modes. The stator flux linkage and its distribution to other phases are then visualized and analyzed in order to understand the mutual coupling between phases and coils under high fault severity. The effect of SFL on fault inductance and back emf is identified and explained. The analysis also includes fault currents and mechanical torques.

6.6 Learning outcomes

- Developing the FEM model in ANSYS and analyzing the fault parameters under varying fault severity and operating modes were learned.
- The stator flux linkage between the faulty coil and its neighbouring coil, affects the induced voltage of the same phase as well as the phase adjacent to it depending on the direction of rotation. The distribution of magnetic flux impact the shape and size of the induced voltage across the healthy and faulty coils.

References

[1] C. Jun-Hyuk G. Bon-Gwan and J. In-Soung. "a dynamic modeling and a fault detection scheme of a pmsm under an inter turn short". *in Vehicle Power and Propulsion Conference (VPPC), IEEE International,*, 2012.

[2] B. M. Ebrahimi and J. Faiz. "feature extraction for short-circuit fault detection in permanent-magnet synchronous motors using stator-current monitoring". *IEEE Trans. Power Electron.*, 25(10):2673–2682, Oct. 2010.

[3] H. Polinder T. D. Strous and J. A. Ferreira. "inductance calculations for pm machines with concentrated windings". *2011 IEEE International Electric Machines Drives Conference (IEMDC),Niagara Falls, ON„*, pages 447–452, 2011.

[4] M. Mardaneh A. Rahideh and T. Korakianitis. "analytical 2-d calculations of torque, inductance, and back-emf for brushless slotless machines with surface inset magnets". *in IEEE Transactions on Magnetics*, 49(8):4873–4884, Aug. 2013.

[5] Dubar Christian. "recent advances in modeling and online detection of stator interturn faults in electrical motors". *PhD thesis. Division of Electric Power Engineering Department of Energy and Environment Chalmers University Of Technology*, 2016.

[6] R. Krishnan. *"Permanent Magnet Synchronous and Brushless DC Motor Drives"*. https://doi.org/10.1201/9781420014235, 2010.

[7] URL `https://ansyshelp.ansys.com/account/securedreturnurl=/Views/Secured/Electronics/v211/en/home.htm%23../Subsystems/TwinBuilder/Content/GettingStarted.htm`.

[8] B. Vaseghi;N. Takorabet;F. Meibody-Tabar;A. Djerdir;J-A. Farooq;A. Miraoui. "modeling and characterizing the inter-turn short circuit fault in pmsm,". *IEEE International Electric Machines and Drives Conference (IEMDC)*, 2011.

[9] B. Nahid-Mobarakeh N. Takorabet F. Meibody-Tabar N. Leboeuf, T. Boileau and G. Clerc. "estimating permanent-magnet motor parameters under inter-turn fault conditions". *IEEE Transactions on Magnetics.*, 48(2):963–966, Feb. 2012.

Chapter 7

Inter turn fault diagnostics using SFDO

This chapter provides the diagnostics of inter-turn faults utilizing the proposed stator flux linkage DC offsets followed by a detailed analysis of the simulation results under a variety of severity levels, fault locations, and operating modes.

7.1 ITF diagnostics- using simulink model

The diagnostic model is shown in Figure 5.9. The model is having three main parts, I) the Field Oriented Control (FOC), II), the PMSM model with ITF and III) Stator Flux linkage DC Offset (SFDO) observer.

All other parts were already covered in chapter 5, so this chapter focuses solely on the SFDO observer. PMSM uses FEM-calculated parameters, such as induced voltages and inductances.

7.1.1 The SFDO observer

As described in chapter 4 of section 4.2, the SFDO proposed here is built on measurement of the stator flux linkage vector, transforming it to a reference frame rotating reverse with the rotor and in that reverse rotating reference frame filter out the quasi-DC component of the stator flux linkage. The way this is implemented here requires two LPFs:

LPF I is used as an integrator of the stator voltage vector. The reason not to use a pure integrator is to avoid drift due to bias errors. The selection of the cut off frequency of LPF I is a balance between having as low cut off frequency as possible (to mimic an integratator as good as possible) but having it high enough to settle bias errors as fast as possible. In practice the cut off frequency becomes a few hertz.

LPF II is used as the low pass filter needed to extract the DC component in the reverse rotating reference frame.

Figure 7.1, shows the complete block diagram of the steps required to obtain the DC offsets in the ASRF's SFL.

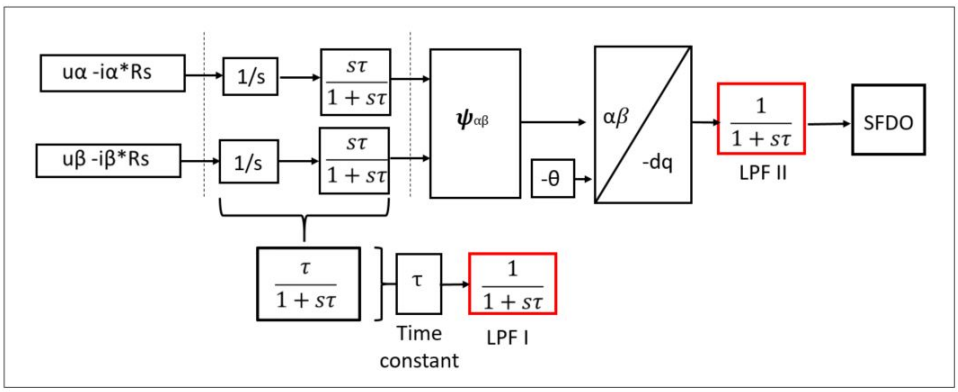

Figure 7.1: The block diagram of SFDO observer

An estimation of the SFL in stationary reference frame can be achieved by integrating the stator voltage. The stator voltage and the current both are in α-β reference frame. Voltage sent by the controller depends on back emf, reference current, and machine actual current. An additional current flows through the circuit during the ITF, and depending on the severity of the fault the total flux in the faulty phase is reduced and thus also the voltage needed by the current controllers to keep the phase current.

The dc offset may also be determined from the controller voltage directly [1, 7]-[2, 7], but this study takes a different approach by using SFL in the ASRF then signal processing and transformation to detect faults without any extra hardware onboard.

Voltage integrator drift is a problem that can be overcome by a high pass filter[3, 7]. Integrator and HPF can act like a time constant times low pass filter (LPF) (explained in chapter 4) and shown in Figure 7.1. The selection of right cut off frequency is important step in obtaining the SFL close to the real SFL. This is discussed further below.

Selection of cut off frequency of LPF I-

The LPF's I role is to integrate the stator voltage vector and estimate the SFL. The LPF is a first order filter with a low cutoff frequency, as it brings the LPF closer to the pure integrator if the cutoff frequency is low[3, 7]. The transfer function used for first order LPF is provided in equation 7.1

$$G(s) = \frac{\tau}{1 + s\tau} \tag{7.1}$$

where τ is the time constant. The magnitude and the phase of the LPF frequency-domain response are, respectively:

$$G = \frac{1}{\sqrt{\omega_s^2 + \omega_c^2}} \tag{7.2}$$

$$\phi = -arctan(\frac{\omega_s}{\omega_c}) \tag{7.3}$$

where ω_c is the filter cut off frequency and ω_s is the stator electrical frequency in rad/s.

Figure 7.2, shows the frequency response of the pure integrator and three LPFs with cutoff frequencies of 1, 5 and 10 Hz, using the transfer function provided in equation 7.1.

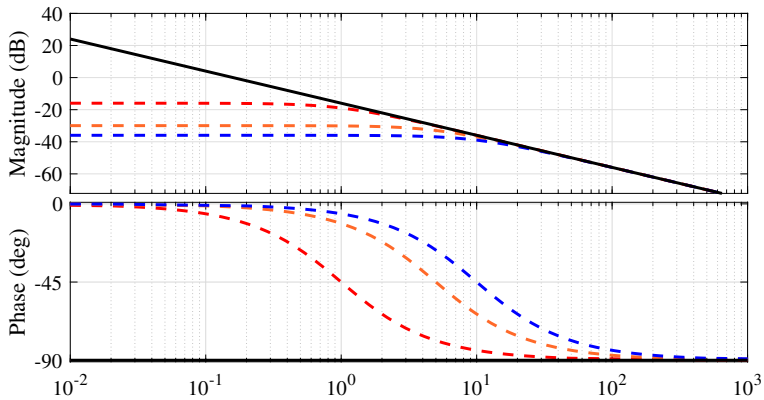

Figure 7.2: Real flux (in black), integrator output (dashed blue) , low-pass filter output (dashed red) with fc = 1Hz,low-pass filter output (dashed orange) with fc = 5Hz and low-pass filter output (dashed navy blue) with fc = 10Hz

Hence from the above frequency response, higher cutoff frequency like 10Hz ensures faster DC-offset rejection, however, it introduces higher deviations to the output signal due to increasing attenuation and phase lag. The most critical situation prevails when the stator frequency ω_s is lower than the cutoff frequency ω_c. On the other

hand, if ω_c is chosen to be very low like 1Hz, which corresponds to a large time-constant of the LPF, the drift problem persists for few initial cycles.

To understand it further, an analysis of integral of a sin wave is made with different cutoff frequency in time domain. Figure 7.3, shows the time domain response of both the pure integrator and the LPF (with ω_c = 2*pi*(1,5 and 10Hz). Contrary, to the pure integrator (1/s), the LPF is able to eliminate the DC-offset in the estimated flux.

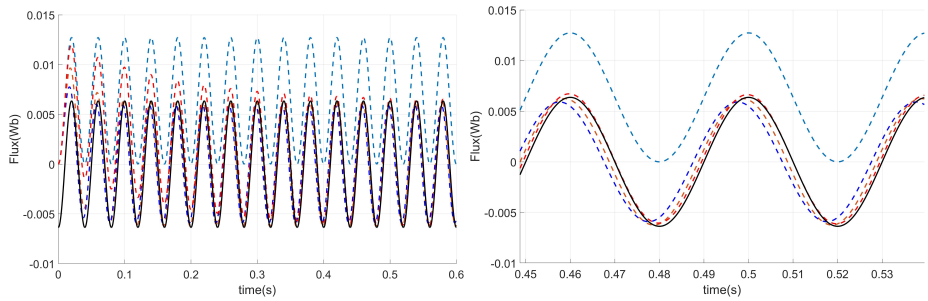

Figure 7.3: Real flux (in black), integrator(1/s) output (dashed blue) and low-pass filter output (dashed red) with fc = 1Hz,low-pass filter output (dashed orange) with fc = 5Hz and low-pass filter output (dashed navy blue) with fc = 10Hz in both figure the right one showing the zoomed version

In order to make sure that we guarantee a pure integrator-like overall frequency response, a cut off frequency of f_c = 1Hz is the ideal case as shown in the Figure 7.3. However, to improve the DC-offset rejection and the settling time in real drive condition, 10Hz is used during the experimental investigation and while performing simulation exercise.

Next step towards SFDO estimation is transformation of SFL in stationary reference frame (α-β) to ASRF using the power invariant Park transformation[4, 7]. The rotor angle is estimated and provided by the machine model.The rotor angle is called theta in the block diagram and is used to transform vectors using the power invariant Park transformation[4, 7].

Choice of cut off frequency of LPF II-

A role of LPF II is to remove dc offsets present in the ASRF's SFL. Since DC offsets need to be looked down, so a very small cutoff frequency is used to filter them out. The choice of the cutoff frequency is made by looking at the FFT of experimental results of ASRF's SFL in both healthy and unhealhty case and its provided below in Figure 7.4 for an instance.

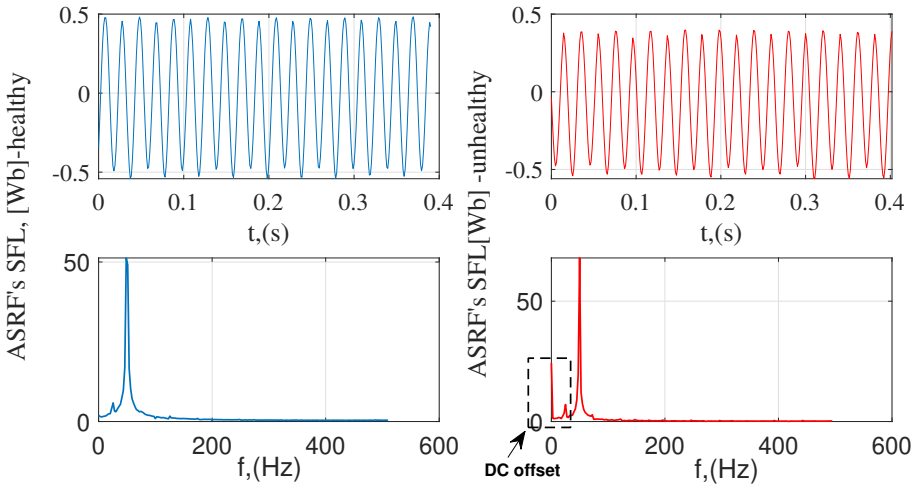

Figure 7.4: FFT illustration of both healthy and unhealthy ASRF's SFL

Based on the results, the cut off frequency can range from 0.1 to 1Hz. The smallest in the range is chosen to avoid magnitude and phase attenuation. Therefore 0.1Hz cut-off frequency was taken into consideration during both experimentation and simulation.

7.2 Simulation setup and results

Simulation setting-The simulation type is continuous, the simulation step time is 0.0012s, and the simulation solver is ode45. The simulation is carried out with DC-link voltage (Udc) of 300V of the PMSM drive system, and the sampling frequency is 833 Hz. The machine runs at 500 rpm. This study is based on curve fitted values of back emf and constant inductances obtained from FEM study under different fault resistances and operation modes.

Healthy mode operation - The PMSM model is initially run with high fault resistance to test the effectiveness of the SFDO observer under healthy conditions. However, the system runs very slowly due to a high fault resistance (R_f). The simulation results provided below in Figure 7.5. The first two figure from left is SFL in stationary and ASRF reference frame. The SFL in stationary reference frame is like a hexagon due to the nature of machine's induced voltage which is rich in 5th and 7th harmonics. The SFL in the ASRF is shaped like an oval and rotates twice as fast as the SFL in the stationary reference frame. Since there is an almost negligible offset in the ASRF due to the extremely small fault current, the SFDO obtained from the observer is at the origin.

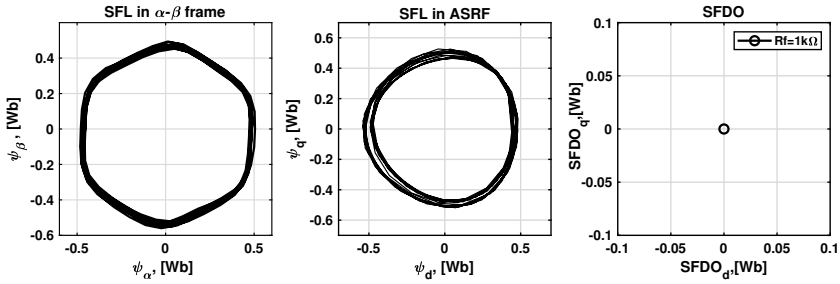

Figure 7.5: SFL and SFDO obtained from the model under healthy operation

Faulty mode operation - One coil out of three in *phase a* is considered for short circuit creation, represented by a coil with resistance R_{a2}, inductance L_{a2}, and back emf E_{a2}. A variable resistor represented by R_f is placed across to represent the short circuit resistance which is very high during normal operation of PMSM and converge to zero when a single winding short fault occurs and yields high circulating current.

7.2.1 Operating modes

Three different operating modes as like in chapter 5 and 6 , are made using a MATLAB script in order to understand and diagnose faults under idling mode, motoring mode and field weakening (FW) mode. In all the operating cases degradation of insulation is approximated with a fault resistance (R_f) connected across the middle coil of stator phase *a* than in *b* and finally in *c*. R_f is varied from 5, 2.5 and 1Ω.

7.2.2 Idling Mode

Idling mode is defined as the freewheeling of machine under speed control. The system simulation is made in simulink by spinning the machine at 500 rpm and setting the currents (i_d =i_q = 0A) to zero which are controlled by PI controller through an inverter.

The simulation results are obtained in the same format as healthy one and are provided in Figure 7.6. The simulation first runs under the case when the fault resistance (R_f) is varying across *phase a* , then *b* and lastly with *phase c* and named in figure as *x, y, and z* respectively.

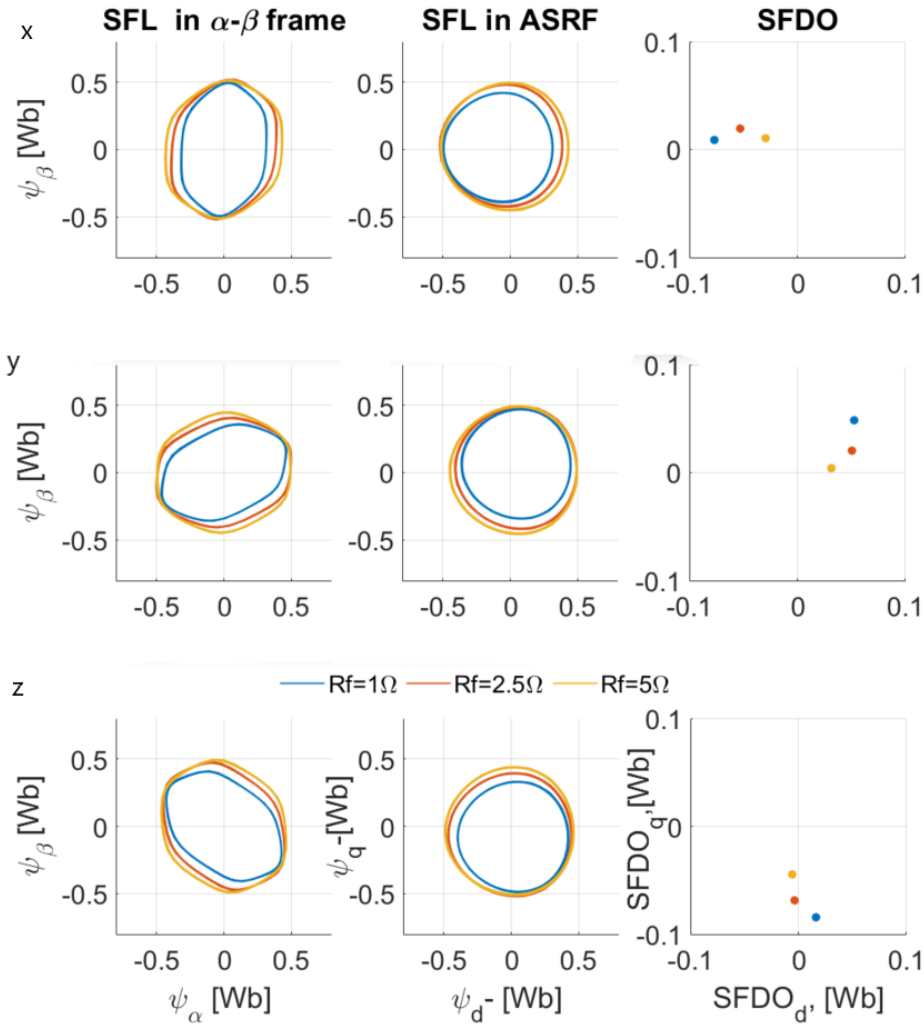

Figure 7.6: Simulation results under idling mode of operation with the R_f placed across in the x) phase *a* y) phase *b* z) phase *c*

In order to understand the obtained results in Figure 7.6x , lets consider the SFL in the idling mode across phase *a, b and c* as written in equation 7.4.

The generic equations of SFL for a three phase PMSM with an ITF can be described according to equation 5.45 (described in chapter 5); this is a linear model, but the simulation model under FOC is a non-linear model.

$$\begin{bmatrix}\psi_{af}\\ \psi_{bf}\\ \psi_{cf}\\ \psi_{f}\end{bmatrix} = \begin{bmatrix} L & M & M & -M_f \\ M & L & M & -M_{a2b} \\ M & M & L & -M_{a2c} \\ -M_f & -M_{a2b} & -M_{a2c} & L_{a2}\end{bmatrix} \begin{bmatrix} i_a \\ i_b \\ i_c \\ i_f \end{bmatrix} + \psi_{pm} \begin{bmatrix} sin(\omega t) \\ sin(\omega t - 2\pi/3) \\ sin(\omega t + 2\pi/3) \\ -\mu * sin(\omega t + \phi)\end{bmatrix} \tag{7.4}$$

where ψ_{af}, ψ_{bf}, ψ_{cf}, are the SFL with a turn fault across each phase, ψ_f is the SFL across the faulty winding, ψ_{pm} is the magnitude of magnetic flux linkage from the permanent magnet under healthy conditions and ϕ is the phase shift between the induced SFL in the short circuited turns and phase *a*. μ is defined as the ratio between the number of shorted turns to the total number of turns in the faulted phase. L_{a2} is the self inductance of shorted coil a_2. M_{a2b} and M_{a2c} is the mutual inductance between coil a_2 to phase *b and c* respectively. M_f is a mutual inductance between coil a_2 to a_1 and to a_3.

$$M_f = L_{a2} + M_{a1a2} + M_{a2a3}; \tag{7.5}$$

Since the phase currents are absent, the influence of the phase current on the SFL is nil.

$$\begin{bmatrix}\psi_{af}\\ \psi_{bf}\\ \psi_{cf}\\ \psi_{f}\end{bmatrix} = \begin{bmatrix} -M_f \\ -M_{a2b} \\ -M_{a2c} \\ L_{a2}\end{bmatrix} \begin{bmatrix} i_f \end{bmatrix} + \psi_{pm} \begin{bmatrix} sin(\omega t) \\ sin(\omega t - 2\pi/3) \\ sin(\omega t + 2\pi/3) \\ -\mu * sin(\omega t + \phi)\end{bmatrix} \tag{7.6}$$

Next step, is to obtain the SFL in the stationary rotating reference frame by using power invariant Clark transformation[4, 7].

$$\begin{bmatrix}\psi_{\alpha}\\ \psi_{\beta}\\ \psi_{0}\end{bmatrix} = \begin{bmatrix} -M_f \\ 0 \\ -(M_f + 2M_{a2c})\end{bmatrix} \begin{bmatrix} i_f \end{bmatrix} + \sqrt{\frac{3}{2}}\psi_{pm} \begin{bmatrix} sin(\omega t) \\ -cos(\omega t) \\ 0\end{bmatrix} \tag{7.7}$$

From the obtained equation 7.7, the reduction in the SFL due to ITF is significant in the alpha axis shown in the left column of Figure 7.7x, is due to inverse magnetic flux linkage from the faulty turn, which opposes the main flux and as a result the resultant SFL decreases.

Last step, is the transformation from SRF to ASRF by using power invariant Park

transformation. The resultant SFL in ASRF are given in equation 7.8.

$$\begin{bmatrix}\psi_{d-}\\ \psi_{q-}\\ \psi_0\end{bmatrix} = \sqrt{\frac{2}{3}}\Bigg[M_f \begin{bmatrix}1\\ 1\\ 0.5\end{bmatrix}\begin{bmatrix}i_f\end{bmatrix} + 2\psi_{pm}\begin{bmatrix}sin2(\omega t)sin2(\omega t - 2\pi/3)sin2(\omega t + 2\pi/3)\\ cos2(\omega t)cos2(\omega t - 2\pi/3)cos2(\omega t + 2\pi/3)\\ 0\end{bmatrix}\Bigg] \tag{7.8}$$

where ψ_{d-} and ψ_{q-} are the SFL in the ASRF. From equation 7.8, it should be stressed that the transformed SFL in the ASRF creates both AC(rotating) and DC(stationary) components which significantly appeared in both the *d and q* axes. The rotating flux in the ASRF is moving twice the electrical speed of the machine, which can be depicted in the middle column of Figure 7.7 and from equation 7.8.

The shift of SFDO from origin is a fault signal and it can be seen from the right column of Figure 7.7x i.e. the lower the R_f is the longer is the SFDO shift from origin. SFDO varies in direct proportions with (i_f) as from equation 7.8. Therefore, in inverse proportion with the fault resistance (R_f). As the R_f decreases the SFDO increases due to higher fault current in the faulty loop (i_f). In a similar fashion the fault in phase *b* (Figure 7.7y) and phase *c* (Figure 7.7z) can be understood with a phase difference of $\pm 120^\circ$ in the three phase and $\pm 30^\circ$ in the stationary reference frame.

Therefore, the SFDO can serve as a useful tool for determining the location as well as the severity of faults. Next, is to check the effectiveness of the SFDO observer in motoring and FW modes of operation.

7.2.3 Motoring Mode

Under motoring mode, the system simulation is made by running the machine at 500 rpm and setting the reference current (i_d =0 and i_q = 3A). During a turn fault in the motoring mode, there is more requirement of current from the controller in order to meet the reference current which is i_q is 3A in the provided case. The three phase SFL in the motoring mode is the summation of flux generated from the stator current and from the permanent magnet and is the same as written in equation 7.4. As a result, the explanation behind the Figure 7.7 is similar to the idling mode except for the tilt in SFL under SRF and ASRF due to lagging phase current in phase *a, b, and c*.

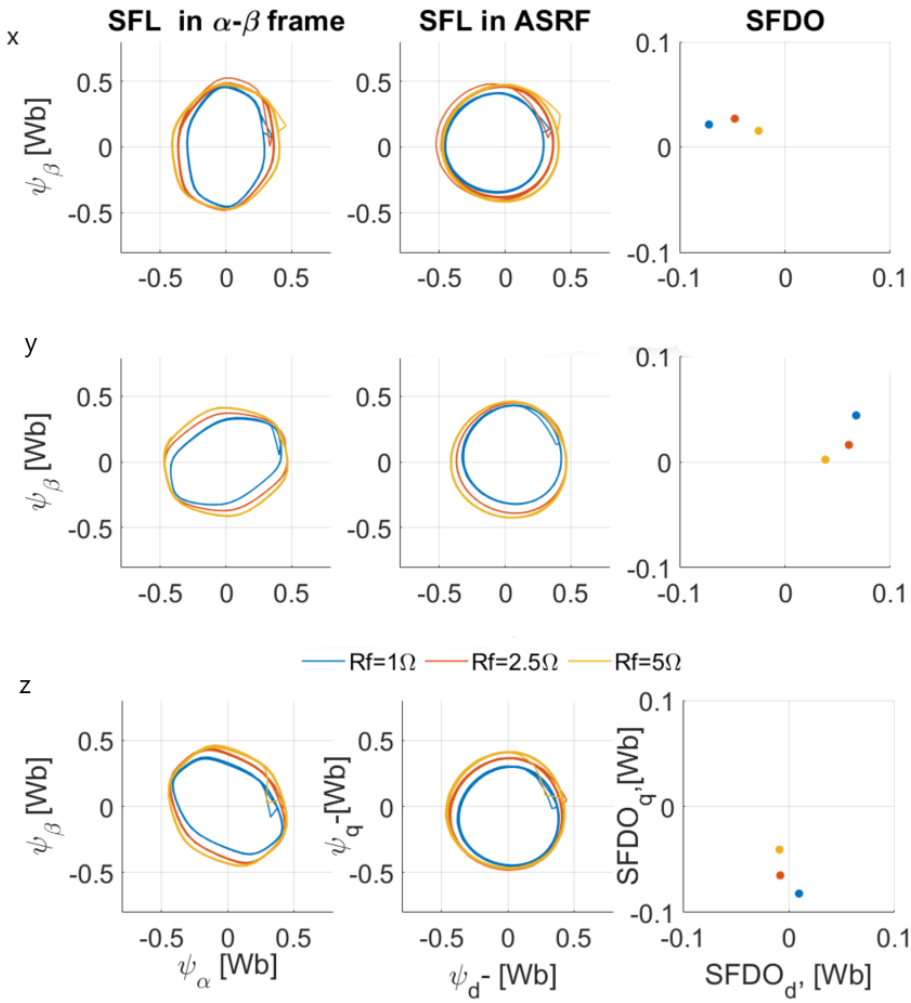

Figure 7.7: Simulation results under motoring mode of the turn fault in the x) phase *a* y) phase *b* z) phase *c*

7.2.4 Field weakening Mode

FW is used to increase the machine speed above its base speed, while maintaining a constant output power, which is the product of torque and motor speed. The reference speed is set to 500 rpm. The purpose of running the machine under FW is to see the rate of decrease in the SFL under the influence of both the ITF and negative current in *d* axes and its affect on the diagnostic parameter SFDO.

During field-weakening, the stator *d* and *q* axis currents are set to I_d = 3A and I_q = -5A and are manipulated to counter the magnetic flux generated by the permanent

magnets. The response under the ITF shown in Figure 7.8 are similar to the motoring and idling mode except there is an additional decrease in the SFL of SRF and ASRF significantly more in *d* axes due to the negative *d* axis current.

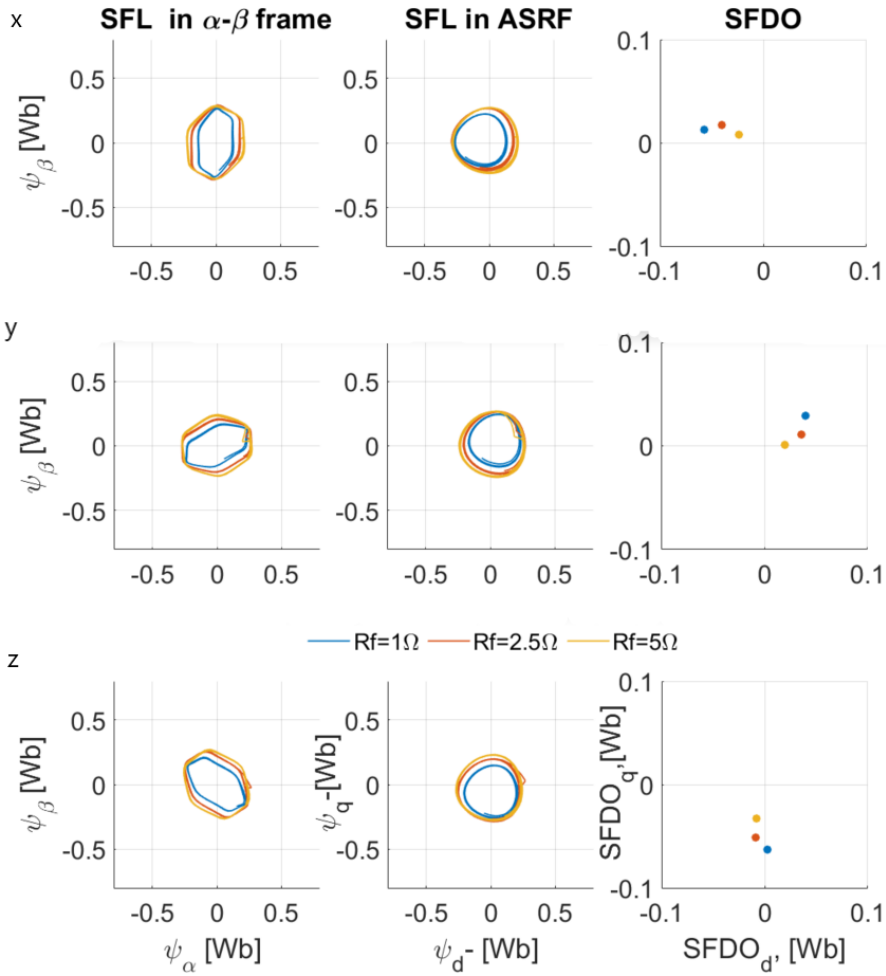

Figure 7.8: Simulation results under FW mode of the turn fault in the x) phase *a* y) phase *b* z) phase *c*

Therefore from above results, the proposed diagnostic method is able to predict the nature, location, and severity of the fault under different operating modes.

7.3 Summary

The application of the SFDO-based diagnostics of the ITF is described in this chapter. By using the Simulink model (chapter 5) and fault parameters from the FEM-based study (chapter 6), the SFDO's are obtained under different operating modes and fault resistance variations. In all three phases of the machine, the fault resistance is varied in the same manner. According to simulation results, SFDO-based diagnostics can be summarised with following advantages:

1. A SFDO's position and length away from the origin indicate the severity of the fault. The SFDO trajectory in different quadrants shows the location of the disturbance .

2. SFDO diagnostics can be used in idling, motoring, and FW modes of operation.

3. No additional hardware is required to implement the SFDO-based diagnostics of ITF.

7.4 Learning outcomes

- Investigating what LPFs are and how to select the correct cutoff frequency.
- The SFDO trajectory under ITF is influenced by the back emf and its harmonic components.

References

[1] A. Bagheri and M. J. H. Bollen. "space phasor model based monitoring of voltages in three phase systems". *18th International Conference on Harmonics and Quality of Power (ICHQP), Ljubljana, Slovenia, 2018*, pages 1–6, 2018.

[2] Nuno M. A. Freire; Jorge O. Estima; A. J. Marques Cardoso. "a voltage-based approach for open-circuit fault diagnosis in voltage-fed svm motor drives without extra hardware". *2012 XXth International Conference on Electrical Machines*, 2-5 Sept. 2012.

[3] G. M. Asher C. Silva and M. Sumner. Hybrid rotor position observer for wide speed-range sensorless pm motor drives including zero speed. *IEEE Transactions on Industrial Electronics*, 53(2):373–378, 2006.

[4] Colm J. et al O'Rourke. "a geometric interpretation of reference frames and transformations: dq0, clarke, and park". *IEEE Transactions on Energy Conversion 34, 4*, pages 2070 – 2083, December 2019.

Chapter 8

Experimental verification

This chapter presents the measurements carried out with the PMSM machine in the lab. First, the experimental setup is presented, then the results of the measurement are presented. It is carried out in a variety of operating modes and finally the model results are validated with the experimental results.

8.1 Experimental setup

An overview of the experimental setup is provided in the form of a block diagram, along with calibration procedures for aligning the resolver angle with the alpha axis of the PMSM. A schematic illustration of the electrical part of the experimental setup is shown below.

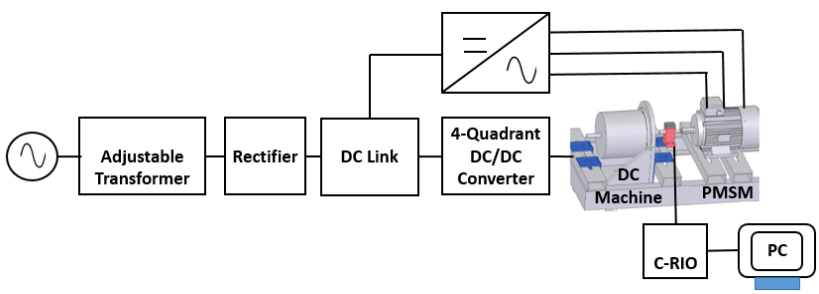

Figure 8.1: Schematic illustration of the electrical part of the experimental setup

From Figure 8.1, DC voltage is supplied by the grid through an adjustable trans-

former and three-phase rectifier bridge. The experimental PMSM is the same as the modelled machine and the details are provided in Table II of chapter 5. It is connected to a voltage controlled DC machine (thus running at almost constant speed when loaded with the PMSM) and controlled through FOC. The control system for the experimental setup is implemented by National instruments (NI) Labview (LV) and is executed in a Compact-RIO (C-RIO), which controls the power electronics, and sample the feedback signals. The controller settings, which decides in what way the C-RIO, should act is made on an interface on a PC.

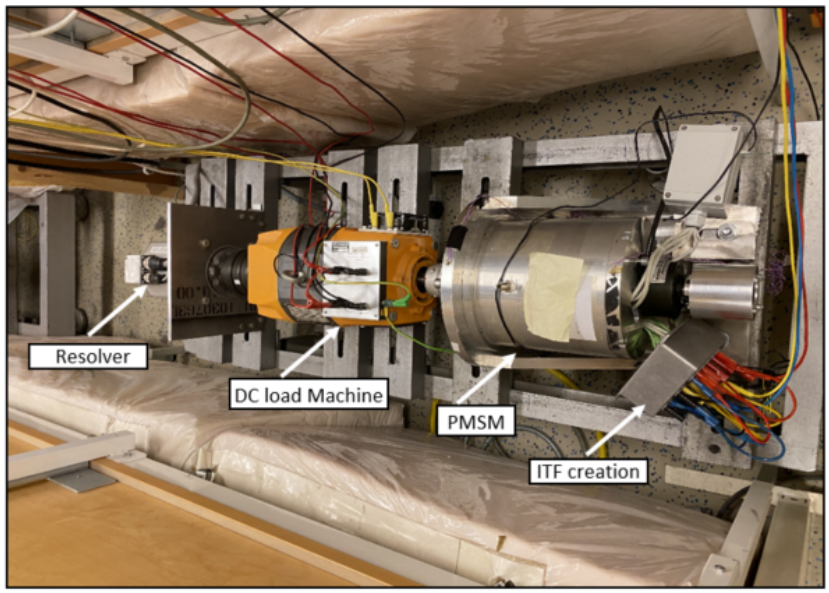

Figure 8.2: Details of lab setup for test machine

The test machine [1, 8], has an external arrangement for the creation of coil faults as also shown in the Figure 8.2. The setup is made to drive the common shaft with one of the machines and brake it with another as shown in Figure 8.2. In this setup, the PMSM is driven by the drive system and the DC machine is used for braking the machine by applying an external resistive load to its terminals. The resolver provides position signals to the C-RIO, which are needed when controlling the speed of a PMSM or the current. C-RIO is programmed using LabVIEW, a graphical programming language[2, 8]. LabVIEW provides a user-friendly development environment, like simulink to create complex control algorithms and user interfaces with ease. The integration of LabVIEW with C-RIO's hardware enables seamless communication and synchronization between the control system and the machine.

LabVIEW interface

The LabVIEW interface set up is actually made for a laboratory exercise in the power electronic course in IEA [3, 8]. In this work the same setup is used. From Figure 8.3, the display is divided into indicator, PI current control and graphical display in addition there are four tabs namely voltage control, current control, motor control, modulation and field weakening. Mostly current control tab-based panel used in this work for the current control, and the fault diagnosis setup.The graphical display is made for displaying the parameters like current and SFL both in stationary, synchronous and anti-synchronous reference frame. In addition, the graphical display of SFDO is built for real time display. The data are observed on this graphical display and later exported to CSV files for further post processing.

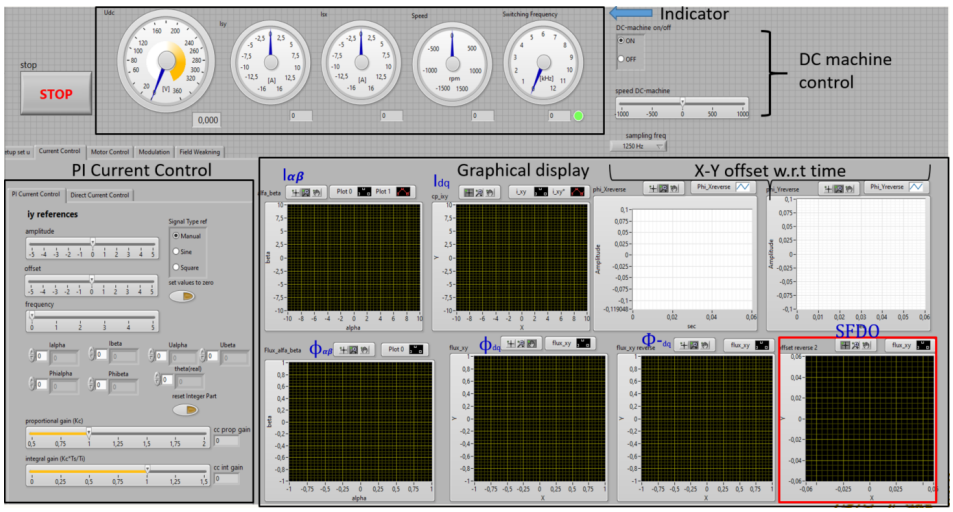

Figure 8.3: The labVIEW interface used for the running the experimental set up

The purpose of this figure is to illustrate how the observations were made and how the results were obtained.

Setting of controller parameters

To adjust the proportional and integral gains of the PI current controller, a slider gain is provided on the interface. By using the reference current generator in q axes (i_q), one can generate a constant, sine wave, or square wave with offset. The reference currents on the q axes are constants in this case. Based on the machine data (as provided in chapter 5), a setting on the slider proportional and integral gains are made.

8.1.1 Rotor angle offset calibration

The position of the rotor is measured by a resolver.On the lab test bench, it was mounted on the same shaft as the PMSM. The reference angle of the resolver must be aligned with the α-axis of PMSM machines. However, they are rarely aligned, and this problem can be solved by measuring the offsets.

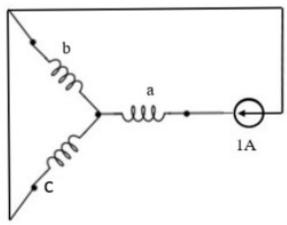

Figure 8.4: An illustration of position offset measurement by giving constant current to phase *a*

To measure it, 1A current is applied to *phase a* as shown in Figure 8.4. This will result in magnetisation only in the alpha axis since those *phases b and c* are symmetrically arranged and will have equal and opposite currents.

The linked flux of the *phase a* winding is aligned with the α-axis of the machine. As a result, a linked magnetic flux is generated, which causes the permanent magnet's *d-axis* to turn mechanically and align with the machine's α-axis. Rotor angle offsets will appear on the LV interface, which can be incorporated from the very beginning into the setup as provided above.

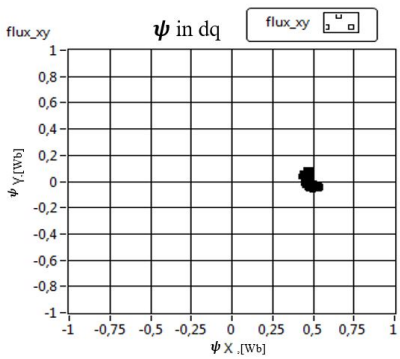

Figure 8.5: Experimental measurements of the SFL in *d-q* reference frame

After the rotor angle calibration the SFL in *dq* axes is checked and it is illustrated in Figure 8.5. The SFL in *d-q* reference frame is a point shape due to the correct alignment of the motor *d axis* with resolver zero degree position. The peak value of the SFL in *d-q* reference frame is 0.5Wb.

8.2 Experimental results

In this section, the measured SFL characteristics of the experimental machine in the α-β, *d-q* , ASRF and SFDO are presented under various operational conditions: different severity faults, generator operation, motoring operation and FW operation.

SFL measurement under no load case - Accurate rotor positions measurements are required for the the *dq* transformations in the control system to provide the reliable SFL transformations. Following the rotor angle offset calibration, initially the machine is run in the idling mode when no current is applied and the speed is 500rpm. The machine is not connected with any additional resistance across any coil of the winding. This is done to ensure the normal three phase operation of the experimental machine. Figure 8.6 , illustrates the experimental stator flux linkages in stationary reference frame, the ASRF and the SFDO from the left of the page.

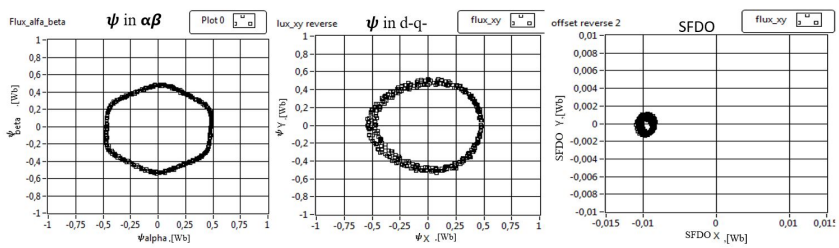

Figure 8.6: Experimental measurements of the SFL in α-β reference frame, *d-q* reference frame, ASRF and SFDO under healthy condition

From the measured experimental result-

- **SFL in α-β reference frame**- The SFL in α-β reference frame is hexagonal shape due to the shape of the induced voltage of PMSM machine. The peak value of the SFL in α-β reference frame is 0.5Wb.
- **SFL in anti synchronous(d-q-) reference frame (ASRF)**-The SFL in negative *d-q* or anti synchronous reference frame is an oval shape and its rotating with twice of the electrical frequency of the machine.

- **SFDO-** The measured SFDO under healthy conditions is not centered at the origin, contrary to what simulations would predict. The position of the SFDO is at $(-0.01,0)$ came out to be robust after changing setups and checking everything, so it may be caused by an uncompensated voltage drop in the power switches, dead-time, discretization, and quantization errors.

SFL measurement with load case -

Following the testing of the experimental setup and the three phase operation, measurements are performed under different operating modes of the machine as described in section 6.33 of chapter 6 with varying fault severity levels.

The machine runs at 500 rpm in all the different operating modes. An ITF is created by placing a resistance across one coil of the winding both when stator windings are Δ connected and star (Y) connected. As a result, ITFs are created in different phases one by one by connecting fault resistors (R_f) and their variations in order of 5, 2.5 and 1 Ω.

1. **Motoring mode**

Motoring mode is the most common mode of operation for electric vehicles. The fault monitoring is illustrated in this case with a step by step illustration of the SFL under different fault resistances. ITF is made across *phase a* with varying R_f. The SFL in stationary reference frame, ASRF and the SFDO are illustrated in the Figure 8.7.

The SFL decreases in α axes when R_f decreases across phase *a*, whereas the offset increases in the ASRF as R_f decreases as shown in Figure 8.7. In the SFL of the ASRF, this offset is evident. In order to see the offset in ASRF it is good to see the origin and in the first case it is equidistant in both directions. However, when R_f decreases, the symmetry from the origin changes. An offset created by the unbalance of the three phase system has been filtered out and presented as SFDO, which has changed the origin. With different fault severity, SFDO increases towards the left as anticipated from the simulation results.

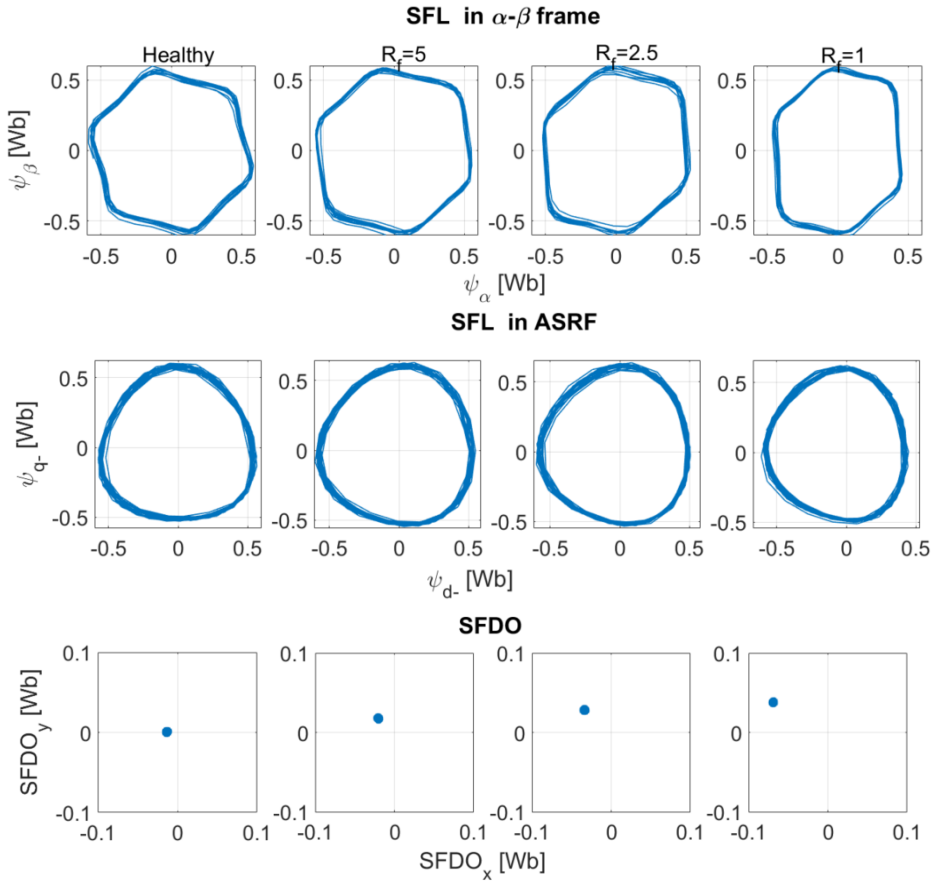

Figure 8.7: The SFL in statoinry reference frame, ASRF and SFDO with decreasing R_f

Results for different ITF severities and locations for the PMSM operating at motoring operation are presented in Figure 8.7. A total of 19 results are shown in figure, from which nine correspond to ITF cases when the the stator windings are star connected and nine when they are connected in delta and one under healthy condition. All the tests marked with circles were made at constant speed of 500 rpm, with the machine operating under no load condition and with the *q axes* current fixed at the value of 3 A and *d axes* current fixed at the value of 0 A. Looking at the displacements corresponding to the faulty cases, it is visible on the figure how the value increases with the fault severity, and it can also be observed that the direction of the displacement of the points is related with the faulty phase.

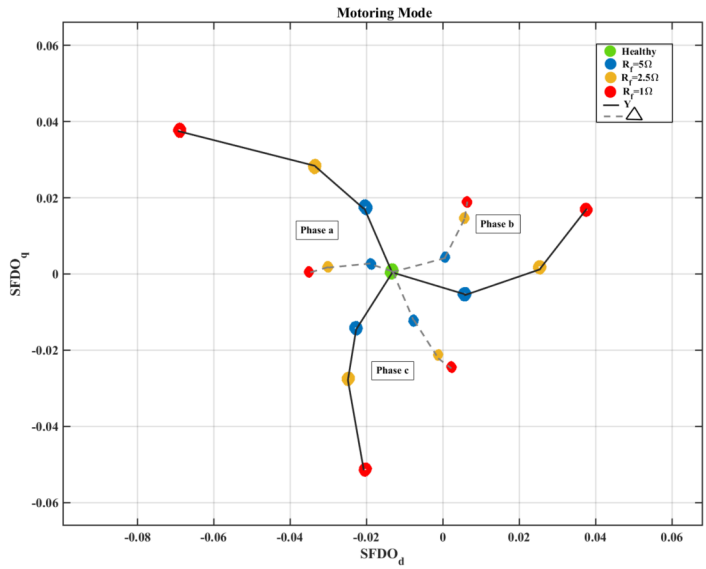

Figure 8.8: Experimental results of the SFDO under motoring mode when stator winding connected in Y and Δ fashion

The vector length from the point close to origin $(-0.015,0)$ to different SFDO points are measured and its angle defined as

$$\theta_{dq} = atan2(SFDO_q, SFDO_d) \tag{8.1}$$

The measured displacement for the Y connected stator winding is tabulated below. Looking at the number column wise it is visible the vector length and its angular position is inversely proportional to the fault severity.

Table 8.1: Comparison of vector length derived from different phases under motoring mode when machine Y connected

Vector length	Phase a	Phase b	Phase c
0-5 Ω	$0.0196\angle 120.7^\circ$	$0.0168\angle$-21.2°	$0.0197\angle -131.3^\circ$
0-2.5Ω	$0.034\angle 130.9^\circ$	$0.035\angle 1.67^\circ$	$0.032\angle$-117.9°
0-1Ω	$0.0689\angle 147.3^\circ$	$0.049\angle 19^\circ$	$0.0527\angle$-100.9°

The location of the fault can be obtained by the angle of the displacement. Ideally, the fault displacement is expected to appear at 0°,120° and 240° for *phases a, b and c,* respectively however in this machine it is for *phases b, a and c.* The maximum computed angular error was obtained for one ITF on phase B, where the faulty point is located at -21°. Therefore, a limit of $\pm 30^\circ$ was defined for the diagnosis.

Table 8.2: Location of faulty phase

Angle range	Faulty phase
0±30°	b
120±30°	a
240±30°	c

2. Idling mode

Similar observations are made when the machine operating mode switched between motoring to the idling mode by adjusting the reference current setting. In this case, the reference current at the *d and q* axes is zero. Results for different ITF severities and locations for the PMSM operating at idling operation are illustrated in Figure 8.9.

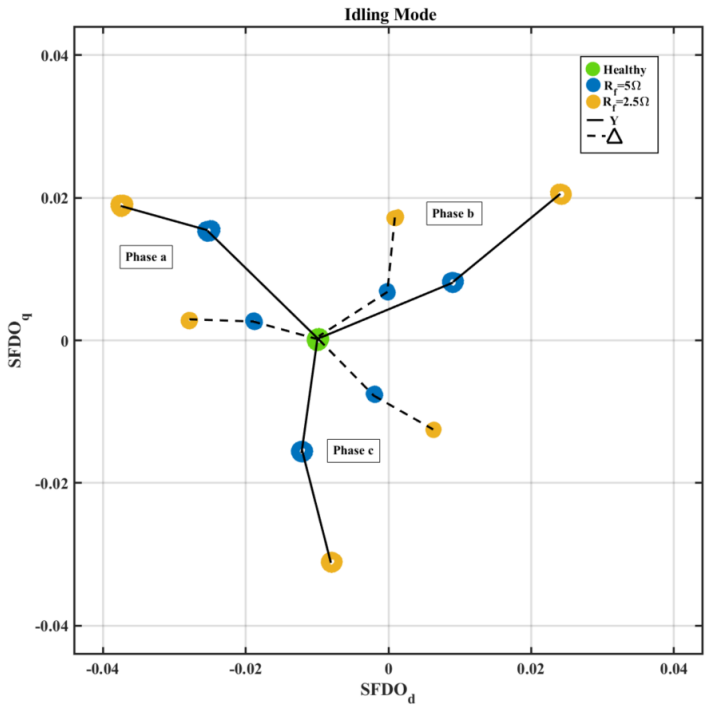

Figure 8.9: SFDO monitoring under idling mode when stator winding connected in Y and Δ fashion

A total of 13 results are shown in figure, from which six correspond to ITF cases when the the stator windings are star connected shown with a solid line and six when they are connected in delta fashion (dash line) and one under healthy condition. In idling mode fault resistors R_f and their variations in order of 5 and 2.5 Ω. SFDO measurement with fault resistance R_f as 1Ω is measured for *phase a* but not while the

R_f connected across *phase b and c*. So they are not plotted here just for the sake of symmetrical distribution.

The vector length between the point close to origin $(-0.015,0)$ and the next consecutive point is computed and tabulated below with a maximum absolute error of 0.006 for all three phases.

Table 8.3: Comparison of vector length derived from different phases under idling mode when machine star connected

Vector length	Phase a	Phase b	Phase c
0-5 Ω	$0.0219\angle 134.5^\circ$	$0.0216\angle 23^\circ$	$0.0154\angle$-97.6°
0-2.5Ω	$0.034\angle 145.4^\circ$	$0.039\angle 31^\circ$	$0.031\angle$-86°

3.FW mode

During field-weakening, the reference d and q axis currents are set to I_d = 3A and I_q =-5A. The FW operation is only conducted when the machine is star connected. However, this operation is run under two different speed as shown below. Interestingly, this mode is showing the variation of the SFDO w.r.t speed as provide in the Figure 8.10.

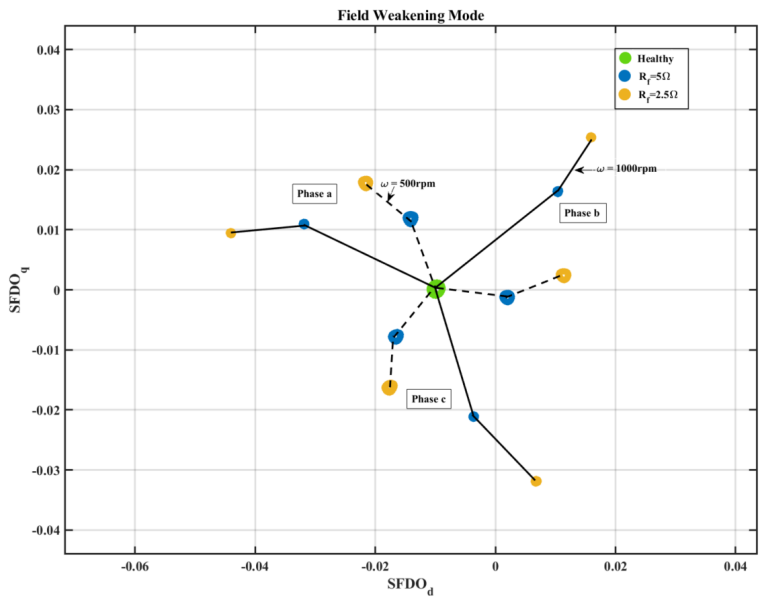

Figure 8.10: Experimental measurements of the SFDO under FW mode

The vector length between the origin and the next consecutive point is computed and

tabulated below for all three phases and under different speed.

Table 8.4: Comparison of vector length derived from different phases under motoring mode when machine Y connected

Vector length	Phase a	Phase b	Phase c
ω=500rpm			
0-5 Ω	$0.0115\angle 110^\circ$	$0.0121\angle -10.9^\circ$	$0.011\angle -126.5^\circ$
0-2.5Ω	$0.021\angle 124^\circ$	$0.0214\angle 3.74^\circ$	$0.019\angle -113.78^\circ$
ω=1000rpm			
0-5 Ω	$0.024\angle 155^\circ$	$0.025\angle 37^\circ$	$0.023\angle -73.8^\circ$
0-2.5Ω	$0.035\angle 166^\circ$	$0.035\angle 42^\circ$	$0.033\angle -84.5^\circ$

The wider angle and change in vector length under two different speed is due to higher fault current and also due to the lack of tuning of the cutoff frequency (fc) of the LPF I provided to obtain the SFL estimate in the stationary reference frame. The phase of the SFL estimate changes gradually as the speed and thus the input frequency increases. The electrical frequency increases when the speed increases from 500 to 1000 rpm and this electrical frequency is closer to the cut off frequency of the SFL estimating low pass filter. This frequency was mistakenly set to about 10Hz at the time of the measurements were made and should have been closer to 1 Hz.

8.2.1 Model Validation

After measuring the results under different operating modes, fault severity and locations, this section aims to validate the simulink model results presented in chapter 5 and 7 for SFDO based diagnostics.

Simulation setting of the simulink model is kept same like the experimental setup, the fault parameters as mentioned in earlier chapter is obtained from the FEM study. However, while inputting the fault parameters with limited knowledge of how fault parameters affect the trajectory, this study made back and forth and here tries to compare all the steps taken to make the model as close as possible to the lab results. So the steps in building the diagnostics have been done in three steps based on the fault parameters entered in analytical equation (AE) using different assumptions. These assumptions are denoted by AE together with the step number as AE1, AE2 and AE3.

- AE1- In the first step, waveforms of fault behavior is obtained from chapter 5 where parameters like induced voltage is illustrated in Figure 5.6. The harmonics distribution of the induced voltage waveform is obtained by the initial experimental no load test at 107rpm. In this case the induced voltage across

the faulty coil is scaled by the factor μ. The average inductances are obtained from FEM analysis.

- AE2- In the second step, the fault severity dependent induced voltage waveform (based on a finite element model) is used and illustrated in Figure 5.13. The induced voltage is composed of all harmonic component but not having the phase of the harmonics. Inductances are again average values listed in Table 6.9.
- AE3- In the last step, the position dependent induced voltage and inductance waveform (exported from finite element model) is used illustrated in Figure 6.13 - Figure 6.24.

SFL Monitoring - The SFL illustration obtained from is arranged similarly to the measured SFL illustrated in Figure 8.11. A fault is created in *phase a's* coil, and then the SFDO's are compared with the measured experimental results under different ITF scenarios. Operating mode is idling and the obtained SFL characteristics from the fault parameters mentioned by AE1, AE2 , AE3 and experimental result is presented in the Figure 8.11. A short explanation of SFDO's monitoring is provided based on fault waveforms derived from parameter setting AE1, AE2 and AE3 .

SFDO Monitoring based on parameter setting AE1

The SFL in different reference frame obtained from the fault parameters based on AE1 is provided at the top of the Figure 8.11. The change in SFDO is significant enough to detect faulted operation when R_f changed from 1k, 5 , 2.5 to 1 Ω. However, the vector length of the SFDO's obtained are shorter than AE2 and AE3.

SFDO Monitoring based on parameter setting AE2

In contrast to results based on AE1, ITF reductions in SFL are significant along the alpha axis (due to ITF across *phase a*) shown in Figure 8.11. The reason is that the exported induced voltage from the FEM corresponds to the electrical frequency used in the experiments. However the position of the obtained SFDO are not exact like the experimental ones.

SFDO Monitoring based on parameter setting AE3

In order to make the model results closer to the experimental ones, the position dependent values of the induced voltage and inductances are exported into the simulink model using 1-D look up table and the SFL characteristics are obtained again. As a result of position-dependent inductance and induced voltage values, some of the SFDO points are very close to the experimentally measured values of the SFDO. This is especially the case when R_f is 5 Ω.

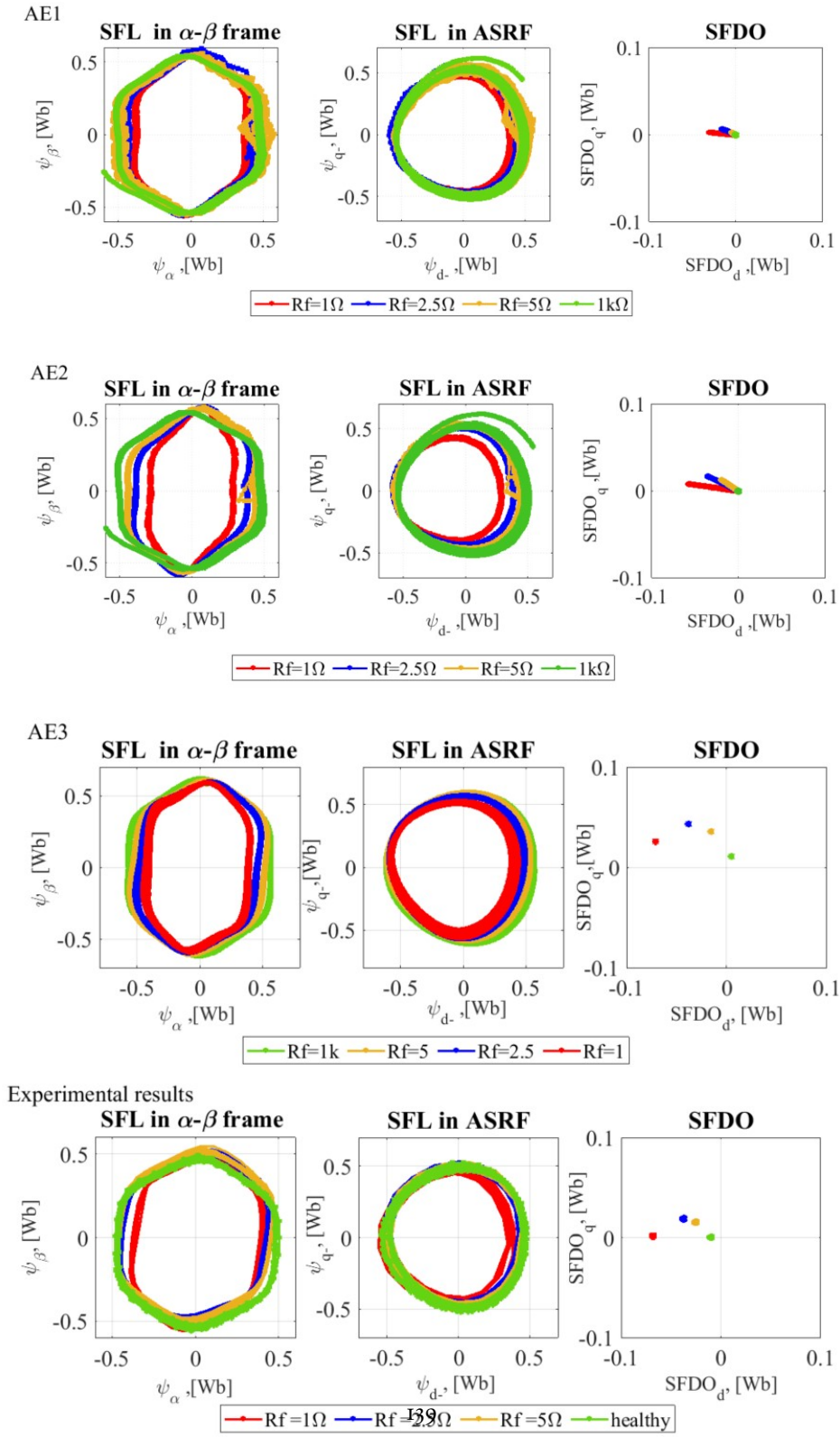

Figure 8.11: The SFL and SFDO obtained from AE1, AE2, AE3 and experimental results

Experimental validation

For the idling operating case, simulation results for all cases and the experiment are plotted together based on the parameters input AE1, AE2, and AE3.

Variation of R_f from 1k to 1Ω is from the right hand side (R_f = 1kΩ) to the left hand side (R_f = 1Ω). In healthy conditions, the SFDO is at origin. While the SFDO from the lab experiments is not centered at the origin.

In case 1 (AE1), the SFDO trajectory is not as close to the experimental trajectory as in case 2 (AE2) and 3 (AE3) . Nevertheless, they are following the trend.

The SFDO's trajectory obtained from case 2 (AE2) is closer (deviation of 3.6%) to the experimental value due to accounting the fault severity dependent voltage waveform. A deviation is calculated by taking the percentage change between the leftmost point when R_f = 1Ω.

The SFDO's trajectory obtained from case 3 (AE3) is above the trajectory obtained by the experimental results. A trajectory's points are close when R_f = 5Ω, and it can also depict healthy offsets.

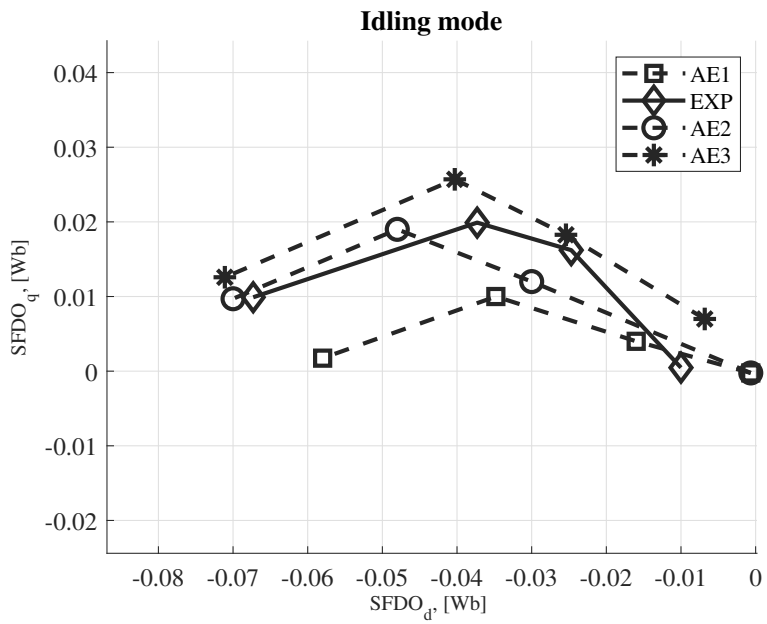

Figure 8.12: A comparison of SFDO's measurement from the experiment and from the simulation model using three cases under idling mode

Operating modes validation

Similar ITF creation is made in the model using AE2 and AE3 under different operating modes and compared with experimental results as shown in Figure 8.13 and 8.14. A deviation is calculated under different operating modes as calculated above using AE2 and it came out to be 3.6% in case of idling, 6.1% in case of motoring mode and 34% in case of FW mode. In case of FW mode the deviation is 34% is calculated by taking the percentage change between the point when R_f = 2.5Ω. This deviation is improved by using the position dependent values of induced voltage especially under motoring and FW mode.

Table 8.5: Percentage deviation using AE2 and AE3

Operating Mode	AE2	AE3
Idling mode	3.6%	6.2
Motoring mode	6.1%	9.1
FW mode	34%	9.5

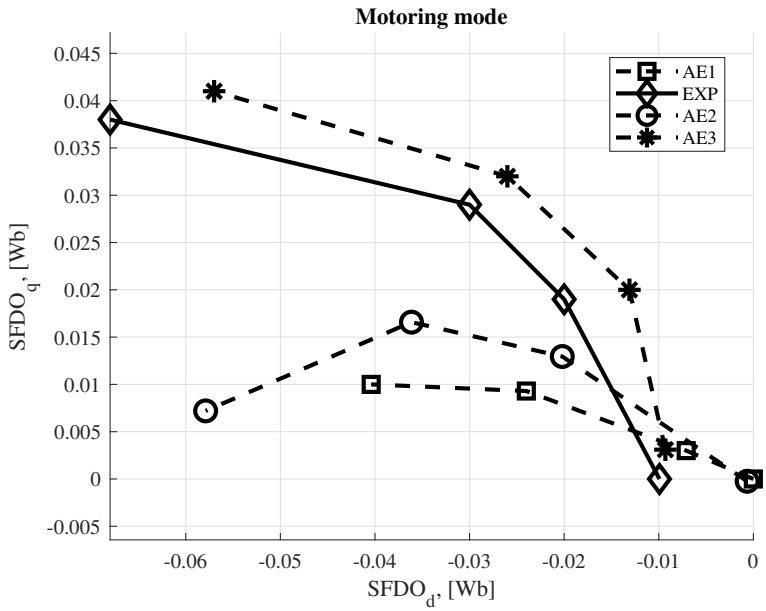

Figure 8.13: A comparison of SFDO's measurement from the experiment and from the simulation model using two cases under motoring mode

The model results follow the same fault trajectory and trend as experimental results in the same quadrant, but the SFDO position deviation is quite high in both the motoring and FW modes when using AE2, while it is more consistent when using AE3. With AE2, the induced voltages are fitted using FFT, resulting in phase-degraded

curves, while with AE3, the induced voltages are position-dependent, similar to the induced voltages from FEM.

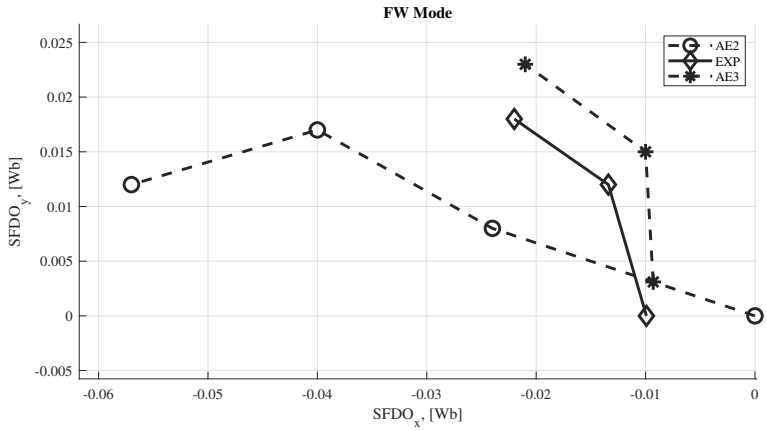

Figure 8.14: A comparison of SFDO's measurement from the experiment and from the simulation model using two cases under FW mode

8.3 Summary

This chapter presents an experimental setup and the experimental results of SFDO-based ITF diagnostics. Model accuracy is good for the idling and motoring mode but under FW mode the model results deviate by 34% and is calculated by taking the percentage change between the point when R_f = 2.5Ω. To increase the efficacy of the model position dependent values of induced voltages and inductances are used. By using it, the deviation is improved by 25% .

Various operating modes, fault severity levels, and locations were used in the experiments. The fault existence and location are diagnosed in accordance with position shift of the SFDO under the influence of ITF. Likewise, experiments were also conducted when the stator winding was connected in a delta configuration. Based on the results, SFDO-based diagnostics are valid for both delta and star-connected machines.

Tuning of cutoff frequency is needed under high speed operation of the PMSM machine.

ITF's diagnostics are summarized in the following figure.

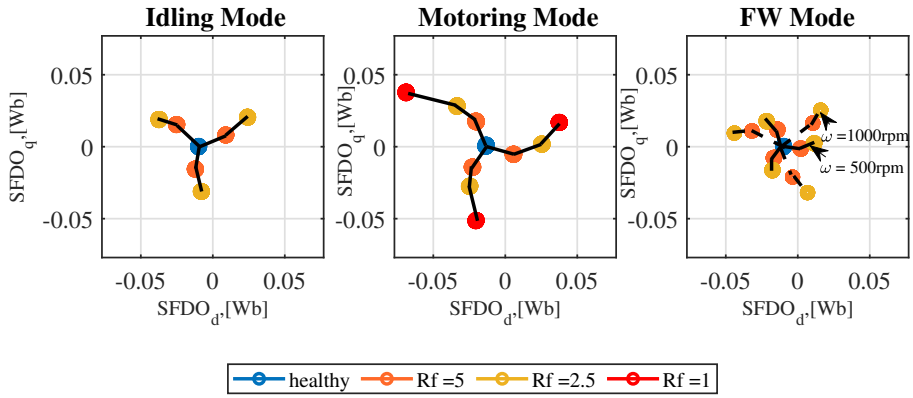

Figure 8.15: Experimental results of the SFDO under idling, motoring and FW mode when the machine is Y connected

According to these results, the applicability of the diagnostic of the ITF using SFDO has been experimentally verified and has the following advantages based on the results of the fault indicator under different operating modes:

(i) It is robust to the operating condition of the motor and can reveal the fault severity under different conditions.

(ii) It can diagnose the stator fault existence, location, and severity.

(iii) It is sensitive and is effective in detecting the fault at an incipient stage.

(iv) It is cost effective and it can integrated into modern EV drives.

8.4 Learning outcomes

(i) Making new sub-VIs with experimental setup helped build knowledge of LV interfaces.

(ii) Testing the model with experiments provided insight into the validity of fault parameters.

(iii) Learning rotor angle calibration was both new and challenging, but once done, it is done.

References

[1] Dubar Christian. "recent advances in modeling and online detection of stator interturn faults in electrical motors". *PhD thesis. Division of Electric Power Engineering Department of Energy and Environment Chalmers University Of Technology*, 2016.

[2] URL https://www.ni.com/en/shop/labview.html?srsltid=AfmBOopb1qSnE-cqSGmN0Ik5J6eZbLm92jWnmg9thQjY9DhNNeJVQvXD.

[3] URL https://www.iea.lth.se/kel/2020/Power%20Electronics%202019.pdf.

Chapter 9

Conclusions

The purpose of this chapter is to summarize the main conclusions of this Licentiate thesis and to outline the next step for the detection and identification of ITF.

9.1 Conclusion

This thesis presents following :

- A specimen is proposed to study how the TEAM stresses in electric traction machines cause insulation degradation and, ultimately, cause ITF. Using the proposed specimen, an interior stress distribution of a simplified coil is visualized, in order to better understand the physics-of-failure of a more complex system than twisted pair enameled wires.
- Based on a literature review of condition monitoring of ITF, a characterization for onboard condition monitoring techniques are proposed. In this characterization, self-analysis methods are distinguished from traction methods based on the functionality they provide. This characterization aims at providing a broad perspective on stator fault monitoring techniques to automotive engineers and researchers, focusing on permanent magnet synchronous machines.
- A methodology is proposed for diagnosing inter turn faults invasively through stator flux linkages in order to fill the existing gap in monitoring inter turn faults. In the proposed method, stator fault detection is based on the dc offset of the Stator Flux Linkage (SFL) in the antisynchronous reference frame (ASRF).

The DC offset of the SFL is calculated by estimating the SFL in the stator reference frame, transforming it to an ASRF and low pass filtering it.

- The proposed methodology is modeled and simulated to make it intuitive. Analytical equations are presented for PMSM machine under both healthy and faulty case. The effect of ITF on back emf, inductance, stator flux linkages, current and torque is discussed. Afterwards, FEM-based modeling is employed to identify parameter values under ITF, which are considered complex and hard to determine through analytical equations alone. FEM results indicated that the back-EMF across each phase input required updating to reflect the impact of stator flux linkage distortion caused by the machine's geometry and due to the fault resistance. Three different case studies are made in order to understand and detect faults under the idling mode, motoring mode and field weakening (FW) mode. The results illustrate the robustness of the diagnostic parameter under different operating conditions.

- Fault detection is carried out when using three sets of parameters in AE based ITF model implemented in Simulink.

  All the three cases are experimentally validated. A close agreement (deviation of 3.6%) was observed between the experimental results and the trajectory obtained from the fault dependent parameter that specifies induced voltage waveforms. Yet, the SFDO trajectory derived from healthy machine parameters also follows the trend.

  A FEM-based identification of parameters under fault conditions and in different operating modes would increase model accuracy and reliability, while initial healthy machine parameters would assist in analyzing faults quickly.

- Lastly, the proposed diagnostic algorithm was implemented in the experimental setup and tested for real-time ITF detection. According to experimental and simulation results, the applicability of the diagnostic of the ITF using SFDO are diagnosed in accordance with position shift of the SFDO under the influence of ITF produced by the SFDO observer. The diagnostic parameter namely SFDO is robust against the operating conditions and type of stator connection (star or delta). Additionally, it is able to diagnose both stator fault existence, its location and related phase. With the proposed method, a stator fault monitoring system is realised.

9.2 Future Work

The following suggestions are included in this thesis for potential future work:

- Measurement of fault current using an experimental setup when the fault resistance is 1 Ω.
- Use the proposed diagnostic technique to investigate the impact of different machine geometry on SFDO under fault conditions.
- Test the proposed fault indicator extensively under varying speed and load conditions. In addition, check SFDO's effectiveness under high frequency switching operation of the electric drive system.
- Integrate the model of the faulted machine to a thermal model, in order to be able to estimate the heat produced by the fault. Using this information, the faulted model can be updated to acquire information for better estimation of the remaining time before neighboring turns fail to insulate.

Appendix A

Appendix A - RMxprt Model Data

GENERAL DATA

Operation Type: Motor
Source Type: DC
Rated Output Power (kW): 4
Frequency (Hz): 37.5
Rated Voltage (V): 106
Load Type: Const Power
Rated Speed (rpm): 750
Operating Temperature (C): 75

STATOR DATA

Stator Core Type: SLOTAC
Stator Position: Outer
Number of Poles: 6
Outer Diameter of Stator (mm): 190
Inner Diameter of Stator (mm): 118.6
Length of Stator Core (mm): 120
Stacking Factor of Stator Core: 0.95
Steel Type of Stator: M1924G

Number of Stator Slots: 9
Type of Stator Slot: 3
Stator Slot

hs0 (mm): 3
hs1 (mm): 8
hs2 (mm): 10
bs0 (mm): 3
bs1 (mm): 27.11
bs2 (mm): 3.3894
rs (mm): 5
Top Tooth Width (mm): 22.6
Bottom Tooth Width (mm): 22.6

STATOR WINDING DATA

Number of Phases: 3
Winding Connection: Y3
Number of Parallel Branches: 1
Number of Layers: 2
Winding Type: Editor
Coil Pitch: 1
Winding Factor: 0.8666
Number of Conductors per Slot: 96
Number of Wires per Conductor: 1
Wire Diameter (mm): 1.369
Wire Wrap Thickness (mm): 0
Wedge Thickness (mm): 8
Slot Liner Thickness (mm): 0.3
Layer Insulation (mm): 0.3
Slot Area (mm^2): 598.14
Net Slot Area (mm^2): 424.989
Slot Fill Factor (%): 42.33
Limited Slot Fill Factor (%): 75
Coil Half-Turn Length (mm): 152.141
End Length Adjustment (mm): 0
End-Coil Clearance (mm): 0
Conductor Type of Stator: copper75 C
Conductor Resistivity at 75C (ohm.mm^2/m): 0.0262

CIRCUIT DATA

Control Type: DC
Lead Angle of Trigger (deg): 0

Trigger Pulse Width (deg): 120
Transistor Drop (V): 0
Diode Drop (V):0

ROTOR DATA

Rotor Core Type: PMINTERIOR
Rotor Position: Inner
Number of Poles: 6
Outer Diameter of Rotor (mm): 117.2
Inner Diameter of Rotor (mm): 40.6

Length of Rotor Core (mm): 120
Stacking Factor of Rotor Core: 0.95
Steel Type of Rotor: M1924G

Rotor Pole Type: 2
Rotor Pole Dimensions
D1 (mm): 115.2
O1 (mm): 3
O2 (mm): 27.8
B1 (mm): 5
Rib (mm): 12
HRib (mm): 3
Magnet Thickness (mm): 5
Magnet Width per Pole (mm): 33
Magnet Type: NdFe35
Maximum Magnet Width per Pole (mm): 41.68

SHAFT DATA

Magnetic Shaft: Yes
Friction Loss (W): 0
Windage Loss/Power (W): 0
Reference Speed (rpm): 3600

PERMANENT MAGNET DATA

Residual Flux Density (Tesla): 1.23

Coercive Force (kA/m): 890
Maximum Energy Density (kJ/m^3): 273.6
Relative Recoil Permeability: 1.099
Demagnetized Flux Density (Tesla): 0
Recoil Residual Flux Density (Tesla): 1.23
Recoil Coercive Force (kA/m): 890

USER DEFINED DATA

SolidCore 0
SleeveThick 0
PartialSol 0
Fractions 1

MATERIAL CONSUMPTION

Stator Wire Density (kg/m^3): 8900
Stator Core Steel Density (kg/m^3): 7650
Rotor Magnet Density (kg/m^3): 7400
Rotor Core Steel Density (kg/m^3): 7650
Stator Copper Weight (kg): 1.72
Stator Core Steel Weight (kg): 10.39
Rotor Core Steel Weight (kg): 7.11
Rotor Magnet Weight (kg): 0.87912
Stator Net Weight (kg): 12.1193
Rotor Net Weight (kg): 7.96
Stator Core Steel Consumption (kg): 23.05
Rotor Core Steel Consumption (kg): 9.4

UNSATURATED PARAMETERS

Stator Resistance R_1 (ohm): 0.78
Stator Resistance at 20C (ohm): 0.642
Stator Leakage Inductance L_1 (H): 0.0219
Slot Leakage Inductance L_{s1} (H): 0.0048
End Leakage Inductance L_{e1} (H): 0.0002204
Spread Harmonic Inductance L_{d1} (H):0.0145
Muture Slot Leakage Inductance Lsm (H): -0.00242
Uniform Air-gap Magnetizing Inductance Lm (H): 0.04067
D-axis Armature Reactive Inductance Lad (H): 0.013758

Q-axis Armature Reactive Inductance Laq (H): 0.0371
D-axis Armature synchronous Inductance Ld (H): 0.035
Q-axis Armature synchronous Inductance Lq (H): 0.059183

NO-LOAD MAGNETIC DATA

Stator Tooth Flux Density (Tesla): 0.9597
Stator Yoke Flux Density (Tesla): 1.42
Rotor Top-Tooth Flux Density (Tesla): 0.80
Rotor Yoke Flux Density (Tesla): 0.612533
Magnet Flux Density (Tesla): 1.02435
Air-Gap Flux Density (Tesla): 0.566
Stator Tooth Ampere Turns (A.T): 4.038
Stator Yoke Ampere Turns (A.T): 35.59
Rotor Top-Tooth Ampere Turns (A.T): 0.635
Rotor Yoke Ampere Turns (A.T): 2.72
Magnet Ampere Turns (A.T): -372
Air-Gap Ampere Turns (A.T): 329
Total Ampere Turn Drop (A.T): 6.99174e-12
Leakage-Flux Factor: 1.23031
Saturation Factor: 1.13068
Correction Factor for Magnetic
Circuit Length of Stator Yoke: 0.364771
Correction Factor for Magnetic
Circuit Length of Rotor Yoke: 1

FULL-LOAD ELECTRIC DATA

Average Input Current (A): 8.78201
Root-Mean-Square Armature Current (A): 9.63575
Armature Thermal Load (A^2/mm^3): 147.138
Specific Electric Loading (A/mm): 22.4769
Armature Current Density (A/mm^2): 6.54619
Frictional and Windage Loss (W): 0
Iron-Core Loss (W): 21.3852
Armature Copper Loss (W): 217.422
Transistor Loss (W): 0
Diode Loss (W): 0
Total Loss (W): 238.807
Output Power (W): 692.085

Input Power (W): 930.893
Efficiency (%): 74.3464
Torque Angle (elec. degree): 91.8
Rated Speed (rpm): 750
Rated Torque (N.m): 8.8119
Fundamental RMS Phase Back-EMF (V): 64.3604
THD of Phase Back-EMF (%): 17.5765

TRANSIENT FEA INPUT DATA

For Stator Winding:
Number of Turns: 144
Parallel Branches: 1
Terminal Resistance (ohm): 0.780569
End Leakage Inductance (H): 0.000220479
2D Equivalent Value:
Equivalent Model Depth (mm): 120
Equivalent Stator Stacking Factor: 0.95
Equivalent Rotor Stacking Factor: 0.95

A.1 Phase measurement obtained from the FEM results

Table A.1: Comparison of fault current[A] derived from different models under different operating modes

Operating Mode - Idling						
Fault resistance	FEM model		SM-CP		SM-PDP	
R_f, [Ω]	I_f, [A]	phase lag,[deg]	I_f, [A]	phase lag,[deg]	I_f, [A]	phase lag,[deg]
1	27	36	15	99	15	99
2.5	11.2	18	9.2	45	15	99
5	5.4	9	5.3	27	15	99
Operating Mode - Motoring						
1	25.81	79	13.67	34	15	99
2.5	10.4	57.6	9.22	14.4	15	99
5	4.34	39.6	5.9	28	15	99
Operating Mode - FW						
1	36.3	75	7.5	28	15	99
2.5	21.5	43.2	5.7	28	15	99
5	12	25	3.7	3.7	15	99

Table A.2: Comparison of flux linkage across faulty coil derived from FEM model under different operating modes

Operating Mode - Idling		
Fault resistance	FEM model	
R_f, [Ω]	ψ_f,[wb]	phase lag,[deg]
1	0.126	64.8
2.5	0.156	35.1
5	0.167	18
$1k$	0.17	0
Operating Mode - Motoring		
1	0.142	70.2
2.5	0.24	47.7
5	0.29	30.6
$1k$	0.32	0
Operating Mode - FW		
1	0.15	59.4
2.5	0.1858	33.3
5	0.194	18.9
$1k$	0.196	0

Table A.3: Comparison of voltage induced across faulty coil[V] derived from the FEM model under different operating modes

Operating Mode - Idling		
Fault resistance	FEM model	
R_f, [Ω]	e_f, [V]	phase lag,[deg]
1	26.8	41.4
2.5	28	16.2
5	26.7	7.2
$1k$	31.12	0
Operating Mode - Motoring		
1	23.82	32.4
2.5	23.72	14.4
5	26.1	7.2
$1k$	30.83	0
Operating Mode - FW		
1	26	36
2.5	25.88	15.3
5	29	4.5
$1k$	30.64	0

A.2 Steps of coupling Maxwell to Twin Builder

Maxwell model must be modified in order to be used in co-simulation with twin builder.

On the Maxwell project tree (be it 2D or 3D), right mouse click on Model tab, then click design setting . On the design setting pop-up window, go to the advanced product coupling tab and enable Transient-Transient link with twin builder. This will let Maxwell know that everything linked to rotor position and winding information are to be taken from twin builder.

Next, click on the excitation tab and find the winding definition. Click the right mouse button on phase A, B, and C windings (one at a time), then select properties and change the winding type to external. Make sure that the initial current is 0. In twin builder, add transient cosimulation as shown with these following arrows.

Twin Builder $\rightarrow SubCircuit \rightarrow MaxwellComponent \rightarrow TransientCosimulation.$

In the Transient-Transient coupling window that appears, browse to open the Maxwell project saved before. Maxwell is opened and loads the project. In the Transient-Transient coupling window, the project information are loaded. Select the project you modified in Maxwell and in the Option tab, select Pin Description and click OK. Place the component and make the connections.